Dissertation

Studies for a Top Quark Mass Measurement and Development of a Jet Energy Calibration with the ATLAS Detector

von

Andreas Jantsch

eingereicht an der

Fakultät für Physik
Technische Universität München

erstellt am

Max-Planck-Institut für Physik
(Werner-Heisenberg-Institut)

München
Dezember 2011

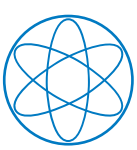

Physik-Department

TECHNISCHE UNIVERSITÄT MÜNCHEN

Max-Planck-Institut für Physik
(Werner-Heisenberg-Institut)

Studies for a Top Quark Mass Measurement and Development of a Jet Energy Calibration with the ATLAS Detector

Andreas Jantsch

Vollständiger Abdruck der von der Fakultät für Physik
der Technischen Universität München zur Erlangung des akademischen Grades eines

Doktors der Naturwissenschaften (Dr. rer. nat.)

genehmigten Dissertation.

Vorsitzender: Univ.-Prof. Dr. A. J. Buras
Prüfer der Dissertation:
1. Hon.-Prof. Dr. S. Bethke
2. Univ.-Prof. Dr. St. Paul

Die Dissertation wurde am 21. Dezember 2011 bei der Technischen Universität München eingereicht und durch die Fakultät für Physik am 11. Juni 2012 angenommen.

Abstract

In this thesis, the development of a new jet energy calibration method as well as studies for a top quark mass measurement with the ATLAS detector are presented. The new calibration method considers jet shape variables in order to improve the linearity and resolution of the jet energy response. Promising results are shown for jet events from Monte Carlo simulation as well as from first $\sqrt{s} = 900\,\text{GeV}$ proton-proton collision data of the Large Hadron Collider. In addition, Monte Carlo studies for a top quark mass measurement in the lepton plus jets decay channel of top quark pair events are performed. Several top quark reconstruction methods are investigated in pseudo-experiments which are equivalent to an integrated luminosity of $\mathscr{L} = 200\,\text{pb}^{-1}$ at $\sqrt{s} = 10\,\text{TeV}$. Assuming a generated top quark mass of $m_t^{gen} = 172.5\,\text{GeV}$, the most promising result is achieved with the Max-p_T reconstruction method which returns a top quark mass of $m_{t,\text{el-channel}}^{\text{Max-p}_\text{T}} = 170.4 \pm 2.2|_{stat.} \pm 8.8|_{syst.}\,\text{GeV}$ in the electron plus jets decay channel including a bias correction of $+\,5.2\,\text{GeV}$ for the central top quark mass value.

Contents

Introduction 1

1. The Top Quark in the Standard Model of Particle Physics 5
1.1. The Standard Model of Particle Physics . . . 5
1.1.1. Particles and Interactions . . . 5
1.1.2. Unified Electroweak Theory and Higgs Mechanism . . . 6
1.1.3. Quantum Chromodynamics . . . 7
1.1.4. Precision Tests and Limitations . . . 9
1.2. Top Quark Physics . . . 11
1.2.1. Top Quark Production . . . 12
1.2.2. Top Quark Decay . . . 14
1.2.3. Top Quark Mass . . . 15

2. The ATLAS Experiment at the Large Hadron Collider 17
2.1. The Large Hadron Collider . . . 17
2.2. The ATLAS Detector . . . 19
2.2.1. The Inner Detector System . . . 20
2.2.2. The Calorimeter System . . . 22
2.2.3. The Muon Spectrometer . . . 28
2.2.4. Trigger and Data Acquisition . . . 30

3. Reconstruction and Energy Calibration of Calorimeter Jets 33
3.1. Jet Reconstruction Algorithms . . . 34
3.1.1. Fixed Cone Size Algorithms . . . 35
3.1.2. Sequential Recombination Algorithms . . . 35
3.2. Truth Particle Jets . . . 37
3.3. Calorimeter Jets . . . 37
3.3.1. Projective Signal Towers . . . 38
3.3.2. Topological Cell Clusters . . . 38
3.4. Energy Calibration of Calorimeter Jets . . . 39
3.4.1. Hadronic Calibration of the Calorimeter Objects . . . 40
3.4.2. Monte Carlo based Jet Level Corrections . . . 44
3.4.3. Data Driven in-situ Jet Calibration . . . 46
3.5. Calorimeter Jet Sequences in ATLAS . . . 47

4. Jet Energy Calibration using Jet Shape Information **49**
4.1. Jet Energy Response . . . 50
4.2. Jet Energy Response of LCTopoJets . . . 51
4.3. Jet Shape Variables and Jet Energy Response Sensitivity . . . 53
4.3.1. Jet Width . . . 53
4.3.2. Eccentricity . . . 53
4.3.3. Isolation distance . . . 54
4.3.4. Depth in the calorimeter . . . 55
4.3.5. Transverse energy fraction of low energetic clusters . . . 56
4.4. Jet Energy Calibration Weight Factors . . . 57
4.5. Validation and Performance in Monte Carlo Events . . . 59
4.5.1. Validation . . . 60
4.5.2. Performance . . . 61
4.6. Validation and Performance in First Data Events . . . 65
4.6.1. Validation of Jet Properties . . . 66
4.6.2. Validation of the Jet Energy Calibration . . . 68
4.6.3. Conclusion . . . 70
4.7. Summary and Outlook . . . 70

5. Top Quark Mass Measurement in the Lepton plus Jets Channel **73**
5.1. Signal and Background Processes – Monte Carlo Samples . . . 74
5.1.1. Signal Processes . . . 74
5.1.2. Background Processes . . . 75
5.2. Event Reconstruction – Reconstruction of the Top Quark Decay Products . . . 78
5.2.1. Electrons . . . 78
5.2.2. Muons . . . 79
5.2.3. Jets . . . 79
5.2.4. Neutrino Reconstruction from Missing Transverse Energy . . . 79
5.3. Event Selection – Study of Background from other Physics Processes . . . 80
5.3.1. Online Trigger Selection . . . 80
5.3.2. Offline Event Selection . . . 81
5.3.3. Results . . . 83
5.4. Top Quark Reconstruction – Study of Combinatorial Background . . . 85
5.4.1. Top Quark Reconstruction Methods . . . 86
5.4.2. Parton Level Studies . . . 87
5.4.3. Jet Level Studies including Parton-to-Jet Matching . . . 88
5.4.4. Jet Level Studies without Parton-to-Jet Matching . . . 89
5.4.5. Conclusion . . . 91
5.5. Top Quark Mass Measurement with the Combined Fit Method . . . 91
5.5.1. Invariant Mass Distribution . . . 91
5.5.2. Combined Fit of Signal and Background . . . 93

5.5.3. Systematic Uncertainties 97
5.5.4. Numerical Results of the Muon Channel 101
5.6. Final Results and Discussion 102

6. Summary and Conclusion **107**

A. Appendix **111**
A.1. Technical Information on Monte Carlo Samples 111
A.2. Additional Figures on Jet Shape Variables 112

List of Figures **117**

List of Tables **119**

Bibliography **121**

Acknowledgement **127**

Introduction

> "Nature has always looked like a horrible mess, but as we go along we see patterns and put theories together, a certain clarify comes and things get simpler."
>
> Richard P. Feynman [1]

Research and science are some of the driving forces in human history. The ability to observe, to describe and to understand nature is not only the basis of all technical development, above all it is of fundamental importance for our present philosophical world view. It is therefore of high relevance to research the nature of all matter in the universe from the largest scales of galaxy clusters to the smallest constituents of matter, the elementary particles.

Particle physics is the branch of science which studies these elementary particles and their fundamental interactions. The goal is to formulate a consistent and unified theory of matter, from sub-atomic up to astronomic scales. The current theory, the Standard Model of Particle Physics, is one of the most successful models in today's science. Nevertheless, it leaves several questions still unanswered. For this reason, physicists from all over the world are working together, building model extensions and analysing experimental data, in order to verify the predictions of the Standard Model and to answer its open questions.

One of the current experiments of particle physics is the Large Hadron Collider (LHC) at the site of the European Organization for Nuclear Research (CERN) near Geneva. It is the world's largest and highest-energetic particle accelerator and addresses Standard Model physics as well as the potential discovery of new physics. The products of the high energetic hadron collisions at the LHC are measured by huge and very sensitive particle detectors. The biggest of them is the ATLAS detector, a multi-purpose detector which allows for the reconstruction of leptonic and hadronic final states in a dynamic range from some few MeV to several TeV.

Calorimeter jets are the experimental signatures of hadronic particle showers in the ATLAS calorimeter system. Their reconstruction and energy determination is a crucial point for many data analyses since the error on the jet energy measurement has a significant impact on the systematic uncertainty. The complete reconstruction and energy calibration chain of the ATLAS experiment is described in this thesis. It is further shown that a dedicated energy calibration for jets is needed in order to account for lost particles. These are stopped in the non-instrumented up-stream material and thus do not leave any signal in the calorimeter system.

The first project of this thesis is the development of a new jet energy calibration method. This development begins with a Monte Carlo study of jet shape variables which describe the shape of a jet in the calorimeter but also the energy distribution inside a jet. The goal is to find a variable which is correlated with the missing jet energy due to lost particles. Considering the most promising variable, a complete set of calibration coefficients is derived from Monte Carlo multi-jet samples in order to be applied jet-by-jet during the reconstruction process. Finally, a set of quality tests is performed on various Monte Carlo samples as well as on first $\sqrt{s} = 900\,\text{GeV}$ ATLAS data.

The second project of this thesis is a Monte Carlo study of the prospects for top quark mass measurement with the ATLAS detector. The top quark is the heaviest known elementary particle and the precise determination of its properties is an important step towards the verification of the Standard Model and the testing of its possible extensions. Due to the large production cross-section at the LHC, top quark measurements are one of the feasible analyses on early ATLAS data. In addition, the statistical uncertainty is expected to be negligibly small in the long run.

In this thesis, a top quark mass measurement in the lepton plus jets decay channel is presented. The analysis is performed on a Monte Carlo dataset which is equivalent to an integrated luminosity of $\mathscr{L} = 200\,\text{pb}^{-1}$ of ATLAS data at a centre-of-mass energy of $\sqrt{s} = 10\,\text{TeV}$. While the high energetic lepton is an important object to trigger on, the top quark is reconstructed from the calorimeter jets of the hadronic decay branch. The energy of the jets is calibrated with the newly developed calibration method and is thus one of its first verifications in a physics analysis.

In order to give an estimate on the background contribution from wrong jet combinations in selected signal events, various top quark reconstruction methods are compared. Using the two most promising methods, a top quark mass measurement from the invariant mass distribution of the three selected jets is exercised for one typical pseudo-experiment. The top quark mass value is then determined from the result of a combined fit, performed on the signal plus background 3-jet invariant mass distribution. In addition, a complete study of the major systematic uncertainties is performed by varying the most important parameters of the event generation and signal reconstruction. Finally, the measured mass value is corrected for the biases effecting the analysis in order to extract the top quark pole mass.

The thesis is structured into the following chapters:

Chapter 1: The Top Quark in the Standard Model of Particle Physics

The Standard Model of Particle Physics and the role of the top quark are introduced. Recent methods for measuring the top quark mass are described and latest results provided.

Chapter 2: The ATLAS Experiment at the Large Hadron Collider

The technical design of the Large Hadron Collider, the ATLAS experiment and all ATLAS sub-detectors are described, including information about the expected performance.

Chapter 3: Reconstruction and Energy Calibration of Calorimeter Jets

The principles of particle jets are explained and an complete overview of the reconstruction chain of calorimeter jets in ATLAS is given.

Chapter 4: Jet Energy Calibration using Jet Shape Information

Various jet shape variables are studied with the focus on their usability for a new jet energy calibration. The calculation of the new jet energy calibration constants is described and the results are tested on various Monte Carlo samples and on first ATLAS data.

Chapter 5: Top Mass Quark Measurement in the Lepton plus Jets Channel

A Monte Carlo based top quark mass measurement in the lepton plus jets channel is presented. Various top quark reconstruction methods are compared and an estimation of the major systematic uncertainties is given.

Chapter 6: Summary and Conclusion

A summary of the results is provided including an outlook for the continuation of the presented studies.

1. The Top Quark in the Standard Model of Particle Physics

As an introduction into the relevant theoretical background, a brief overview of the Standard Model of Particle Physics [2, 3, 4] is provided. In this context, high energetic proton-proton scattering is discussed as well as the role of the top quark, its properties and recent results of top quark mass measurements [5, 6].

1.1. The Standard Model of Particle Physics

The **Standard Model of Particle Physics** (SM) is the theory of the fundamental particles and their interactions. It is a relativistic and re-normalisable Quantum Field Theory (QFT) and combines the unified theory of Electroweak Interactions and Quantum Chromodynamics (QCD). The SM carries the group structure of the gauge group $\mathrm{SU(3)_C} \otimes \mathrm{SU(2)_L} \otimes \mathrm{U(1)_Y}$, where C stands for colour, L stands for left and Y stands for the electroweak hypercharge. At energies below $\sim 200\,\mathrm{GeV}$, the local gauge symmetry of the SM is spontaneously broken to $\mathrm{SU(3)_C} \otimes \mathrm{U(1)_Q}$ with Q referring to the electric charge [4].

1.1.1. Particles and Interactions

All known elementary particles are classified into **fermions** having half-integer spin or **bosons** having integer spin. The fundamental fermions can be subdivided into leptons and quarks and constitute all of the observed visible matter in the universe. For each fermion a corresponding anti-fermion exists with the same mass, but opposite electric charge Q, colour i and third component of the weak isospin $\mathrm{I_3}$. Here, colour is the charge of the strong interaction which is an additional degree of freedom with three possible values, usually referred to as red (r), green (g) and blue (b). All elementary fermions are ordered in three generations with ascending masses as summarised in Table 1.1.

The three fundamental forces between the fermions are the **electromagnetic**, **weak** and **strong** interactions. They are mediated by vector gauge bosons, where the strength of the coupling depends on a coupling constant and is proportional to the corresponding charge (see Table 1.2).

The gauge boson of the **electromagnetic** interaction is the photon γ. It remains massless after symmetry breaking (cf. Section 1.1.2) and couples to all fermions with a non-zero electric charge and infinite range.

Fermions	Generation			Electric	Colour	Weak Isospin (I, I_3)	
	1	2	3	Charge $[e_0]$		left-handed	right-handed
Leptons	ν_e	ν_μ	ν_τ	0	–	(1/2, +1/2)	–
	e^-	μ^-	τ^-	-1		(1/2, −1/2)	(0, 0)
Quarks	u_i	c_i	t_i	$+2/3$	$i =$ r,g,b	(1/2, +1/2)	(0, 0)
	d_i	s_i	b_i	$-1/3$		(1/2, −1/2)	(0, 0)

Table 1.1.: The three generations of fundamental fermions.

The **weak** interaction is mediated through the three gauge bosons $W^\pm$ and Z^0. They couple to left-handed fermions and right-handed anti-fermions only and receive a mass in the order of $\sim 100\,\mathrm{GeV}$ after symmetry breaking. All bosons of the weak interaction carry as well weak charge and thus interact among each other. In addition, the W-bosons carry an electric charge and thus interact also electromagnetically.

The eight massless gluons g^μ of the **strong** interaction couple only to quarks while the colourless leptons are not effected. Since the gluons have colour as well, they interact among each other. This allows for gluon fusion, among others an important mechanism of top quark pair production.

Interaction	Group	Vector Boson	Mass [GeV]	Couples to	Relative Strength	Range
electromagnetic	$\mathrm{U(1)_Q}$	photon γ	0	electric charge	10^{-2}	∞
weak	$\mathrm{SU(2)_L}$	$\mathrm{W^\pm}$, $\mathrm{Z^0}$	$\sim 10^2$	weak charge	10^{-13}	10^{-18}m
strong	$\mathrm{SU(3)_C}$	8 gluons g^μ	0	colour charge	1	10^{-15}m

Table 1.2.: The fundamental interactions in the Standard Model of Particle Physics.

1.1.2. Unified Electroweak Theory and Higgs Mechanism

The unified theory of electromagnetism and weak interaction is described in the model of S. L. Glashow [7], S. Weinberg [8] and A. Salam [9] by the gauge group $\mathrm{SU(2)_L} \otimes \mathrm{U(1)_Y}$, where fermions are represented by left-handed doublets and right-handed singlets of the weak isospin. Since gauge invariance requires the absence of explicit mass terms in the Lagrangian, all particles are initially assumed to be massless.

As a mechanism of mass generation conserving the gauge invariance, P. Higgs [10] introduced in 1964 a complex scalar doublet field $\Phi = (\phi_1, \phi_2)$, which leads to an additional term $\mathcal{L}_\Phi$ in the SM Lagrangian with a rotationally symmetric potential $V(\Phi)$:

$$\mathcal{L}_\Phi = \left(\partial_\mu \Phi^\dagger\right)\left(\partial^\mu \Phi\right) - V\left(\Phi\right) \tag{1.1}$$

$$V(\Phi) = -\mu^2 \Phi^\dagger \Phi + \lambda^2 (\Phi^\dagger \Phi)^2 \tag{1.2}$$

Assuming $\mu^2 > 0$, the Higgs potential $V(\Phi)$ has a minimum at a non-zero value of $\Phi^\dagger\Phi$ ensuring spontaneous symmetry breaking from $\mathrm{SU(2)_L} \otimes \mathrm{U(1)_Y}$ to $\mathrm{U(1)_Q}$. The vacuum configuration is chosen to be $\langle\Phi\rangle = \left(0, v/\sqrt{2}\right)$ and the physical degrees of freedom are obtained expanding the theory around the minimum $\langle\Phi\rangle$. One consequence is the generation of Dirac mass terms for all fermions as well as for the weak vector bosons $W^\pm$ and Z^0. Only the photon remains massless. An important prediction of the theory is the existence of one massive spin-zero particle H, the so-called Higgs boson with mass $\mathrm{m_H}$. The discovery of the Higgs boson is one of the key goals of the Large Hadron Collider experiments.

As a consequence of the structure of the 3×3 Dirac mass matrices after diagonalising, the quark eigenstates with respect to the weak interaction are not any longer equal to their mass eigenstates. Thus flavour-changing processes including a violation of the $\mathcal{CP}$-symmetry are allowed.

$$V_{\mathrm{CKM}} = \begin{pmatrix} V_{ud} & V_{us} & V_{ub} \\ V_{cd} & V_{cs} & V_{cb} \\ V_{td} & V_{ts} & V_{tb} \end{pmatrix} \tag{1.3}$$

The strengths of these flavour-changing weak couplings are proportional to $|V_{qq'}|^2$, the elements of the complex and unitary CKM quark-mixing matrix V_{CKM}, introduced by N. Cabibbo, M. Kobayashi and T. Maskawa [11, 12].

1.1.3. Quantum Chromodynamics

Quantum Chromodynamics (QCD) [13, 14, 15, 16], represented by the gauge group $SU(3)_C$, is the gauge field theory of strong interactions between coloured quarks and gluons. Its effective coupling constant $\alpha_S(Q^2)$ depends on the energy scale of the process Q. While the coupling is very strong at low energies (i.e. large distances), it gets weaker at higher energies (i.e. short distances). As a consequence, quarks and gluons can be considered as free particles in processes with large momentum transfer (**Asymptotic Freedom**). This allows for quantitative predictions by using perturbative theories, which have been successfully tested in deep inelastic scattering experiments, mainly at SLAC and DESY.

In contrast to this, quarks and gluons tend to form colour-neutral bound states at low energies. From a certain distance on, it is energetically preferred to create a quark-antiquark pair than to continue to extend the colour flux. This so-called **Confinement** is the reason that no free quarks or gluons have been observed yet. Bound states of quarks and gluons are called hadrons and can be classified into baryons and mesons. Baryons are composed of three quarks with different colour ($q_i q_j q_k$) whereas mesons are composed of a quark-antiquark pair ($q_i \bar{q_{\bar{i}}}$). Here, the indices i, j, k represent the colour and $\bar{i}$ the anti-colour, respectively.

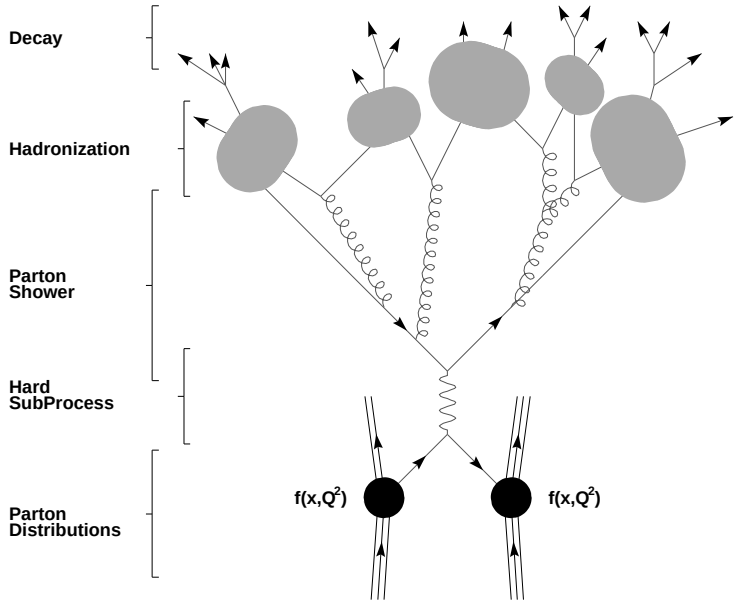

Figure 1.1.: Phenomenological model of a hard proton-proton interaction at the Large Hadron Collider [17].

The high energetic proton-proton collisions at the Large Hadron Collider can be generally described by a hard scattering process between two hadrons into a final state X as shown in Fig. 1.1. It results into an interaction between the partons where only a fraction x_i of the proton momentum is transferred. A factorisation ansatz allows to separate the short distance interaction of the partons i and j with its partonic cross section $\hat{\sigma}^{ij\to X}$ from the long distance interaction, calculated using the non-perturbative parton density function $f_i\left(x_i, Q^2\right)$ of the protons.

The total production cross section of a final state X with its invariant mass m_X in pp-collisions at a centre-of-mass energy $\sqrt{s}$ can be calculated from [16]:

$$\sigma_{p\bar{p}\to X} = \sum_{i,j=q,\bar{q},g} \int dx_i dx_j f_i\left(x_i, Q^2\right) f_j\left(x_j, Q^2\right) \times \hat{\sigma}^{ij\to X}\left(\rho, m_X, x_i, x_j, \alpha_S\left(Q^2\right), Q^2\right) \quad (1.4)$$

with $\rho = 4m_X/\hat{s}$, where $\hat{s} = x_i x_j s$ is the effective centre-of-mass energy of the hard sub-process. The summation loops over all possible partonic sub-processes: **gluon–gluon fusion** (gg), **quark–antiquark annihilation** ($q\bar{q}$) and **quark–gluon scattering** (gq and $g\bar{q}$).

Today, most of the partonic processes are available in leading order perturbation theory, only a few have been already calculated in next-to-leading order. Higher order corrections as well as perturbative hadronic fragmentation effects are taken into account by so-called **Parton Shower** (PS) models. Those describe the behaviour of quarks and gluons at a given momentum scale in the leading $\log Q^2$ approximation, using the DGLAP QCD evolution equations [18, 19, 20]. Thus, gluon radiation from the coloured initial and final state partons is allowed and can initiate itself quark-antiquark pair production cascades as shown in Figure 1.1.

Due to the colour confinement, the resulting coloured partons are transformed into colourless hadrons including also quarks and antiquarks spontaneously created from the vacuum. Since a perturbative treatment of this **Hadronisation** process is not yet possible, non-perturbative phenomenological descriptions, e.g. the Lund string model [21], are used instead.

The resulting hadrons or their decay products can be finally grouped together into bunches of particles. Only these so-called **Particle Jets** can be directly observed by interacting with particle detectors used in high energy physics.

1.1.4. Precision Tests and Limitations

The Standard Model of Particle Physics is one of the most successful models in the history of science. It has been validated in high-precision measurements over the last 60 years and predicted the existence of the W- and Z-bosons, the gluon, the charm and top quark before these particles have been experimentally observed [2].

Results from global electroweak fits show a very good agreement with currently accessible experimental data and give exclusion limits to parameters, like the mass of the SM Higgs boson (see Figure 1.2 left), that have not been measured yet. Another impressive agreement has been shown in fits of the CKM matrix parameters using data from flavour violating processes like B-meson decays (see Figure 1.2 right).

In spite of the success of the Standard Model, it is unlikely to be the final theory. It has at least 19 arbitrary parameters (e.g. values of masses, coupling constants, mixing angles) which are chosen to fit the experimental data. Furthermore it leaves several questions unanswered:

- A re-normalisable, relativistic quantum field theory of **Gravity** does not exist. Instead, gravity is described by the theory of general relativity. Finding a unified consistent model of all four fundamental interactions which describes subatomic as well as astronomic scales, is one of the future challenges in particle physics.

- The observed **Cosmological Matter-Antimatter Asymmetry** cannot be explained by $\mathcal{CP}$-violation in flavour changing weak interactions only.

- Cosmological measurements of galaxy cluster rotation and cosmic microwave background indicate that only 4 % of the energy present in the universe are explained by the Standard Model. About 24 % consist of so-called non-baryonic **Dark Matter** which interacts only weakly with the SM fields. The missing 72 % are postulated to be **Dark Energy**, a kind of constant background energy. It is more than hundred orders of magnitude larger than the vacuum energy explained by virtual particles and the energy-time uncertainty principal.

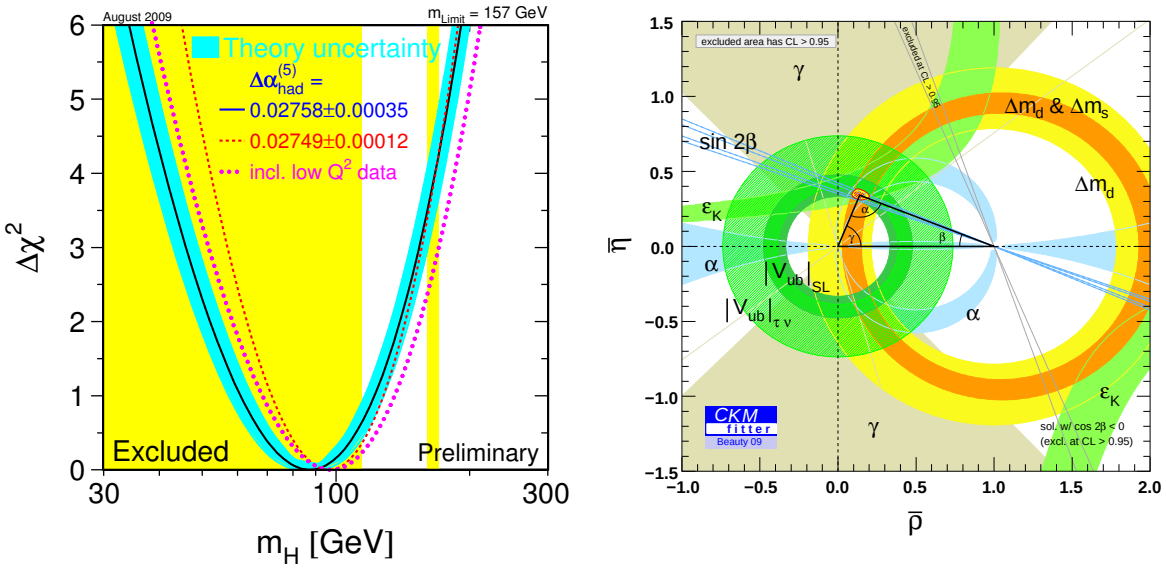

Figure 1.2.: Left: Experimental limits on the Higgs boson mass. $\Delta\chi^2 = \chi^2 - \chi^2_{min}$ of the combined fit to electroweak precision measurements as a function of the Higgs boson mass m_H. The blue/shaded band indicates the theoretical uncertainties due to unknown higher order corrections. The vertical yellow/shaded bands represent the regions excluded at 95 % CL by direct Higgs boson searches in experiments at LEP and Tevatron. [22] Right: Constraints in the $(\bar{\rho}, \bar{\eta})$-plane including the most recent inputs in the Standard Global CKM Fit. The $|V_{ub}|$ constraint has been split in the two contributions: $|V_{ub}|$ from inclusive and exclusive semileptonic decays (plain dark green) and $|V_{ub}|$ from $B \to \tau + \nu$ (hashed green). The red hashed region of the global combination corresponds to 68 % CL. [23]

- The Standard Model knows only left handed, massless neutrinos. Nevertheless, the observed **Neutrino Oscillation** implies non-zero neutrino masses. A possible explanation requires right-handed neutrinos which have not been observed.

- An extreme fine tuning is required in order to cancel the large loop corrections to the Higgs boson mass (**Hierarchy Problem**).

- Theoretically, the Standard Model Lagrangian allows for $\mathcal{CP}$-violation in strong interaction processes as well. However, no violation has been observed which requires an extreme fine tuning of the strong $\mathcal{CP}$-phase very close to zero (**Strong $\mathcal{CP}$-Problem**).

Several extensions of the SM [24], like **Supersymmetry** [25, 26], models including **Extra Dimensions** [27, 28, 29] and **String Theory** address these problems and predict **New Physics** at the TeV scale. Nevertheless, no direct experimental evidences for theories beyond the SM are found yet, which was one of the reasons to built the LHC (cf. Chapter 2). The only constraints on New Physics are given by global fits, e.g. setting of lower limits to the mass of hypothetical charged Higgs bosons of the **Minimal Supersymmetric Standard Model** (MSSM).

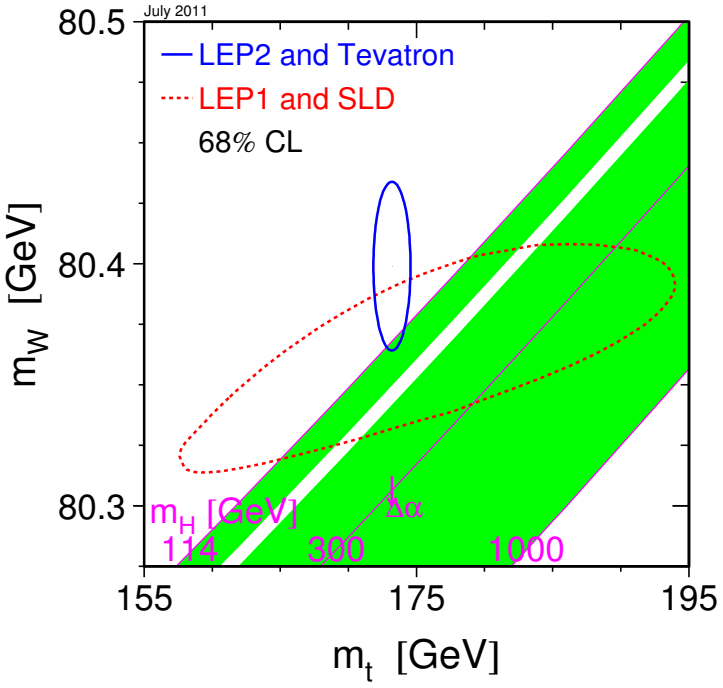

Figure 1.3.: Comparison of the indirect constraints on m_W and m_t based on LEP-I/SLD data (dashed contour) and the direct measurements from the LEP-II/Tevatron experiments (solid contour). In both cases the 68 % CL contours are plotted. [30]

1.2. Top Quark Physics

The top quark is the weak-isospin doublet partner of the bottom quark (see Table 1.1) and with a mass of $m_t = 173.2 \pm 0.9\,\text{GeV}$ [30] the heaviest observed elementary particle. It has been predicted in 1977 and discovered in 1995 by the Tevatron collaborations CDF [31] and D0 [32]. The width of the top quark has been calculated to be $\Gamma_t \sim 1.36\,\text{GeV}$ [2] with a corresponding life time of $\tau_t \sim 0.5 \cdot 10^{-24}\,\text{s}$. Thus it is the only quark which is expected to decay before hadronisation.

Due to its large mass, the top quark gives significant contributions to higher order loop corrections of electroweak processes and is therefore a crucial parameter for precision tests of the Standard Model. Furthermore, the correlation between top quark and W-boson masses allows to constrain the mass of the Higgs boson (see Figure 1.3). In addition, a precise measurement of the top quark mass is a powerful probe of new physics models beyond the SM, e.g. Supersymmetry.

In the following, top quark production mechanisms, decay channels and latest results of top quark mass measurements are discussed. A complete review of all top quark properties can be found in [5, 6].

1.2.1. Top Quark Production

At hadron colliders, two different top quark production mechanisms occur: top-antitop quark pair production via strong interaction processes and single top quark production via electroweak interaction [33].

Strong Top Quark Pair Production

Following Section 1.1.3, top quark pair production in high energetic proton-proton collisions can be described by perturbative theories from the partonic hard scattering sub-process. The total production cross section $\sigma_{p\bar{p}\to t\bar{t}}$ of $t\bar{t}$-pairs can be calculated using Equation 1.4 and depends on the top quark mass m_t, the centre-of-mass energy $\sqrt{s}$ and the partonic cross section $\hat{\sigma}^{ij\to t\bar{t}}$.

At leading order, only quark–antiquark annihilation ($q\bar{q}$) and gluon–gluon fusion (gg), illustrated in Figure 1.4, give a significant contribution. In contrast to the $p\bar{p}$-collisions at Tevatron (85 % $q\bar{q}$ vs. 15 % gg), gluon–gluon fusion is the dominating process at the Large Hadron Collider (10 % $q\bar{q}$ vs. 90 % gg).

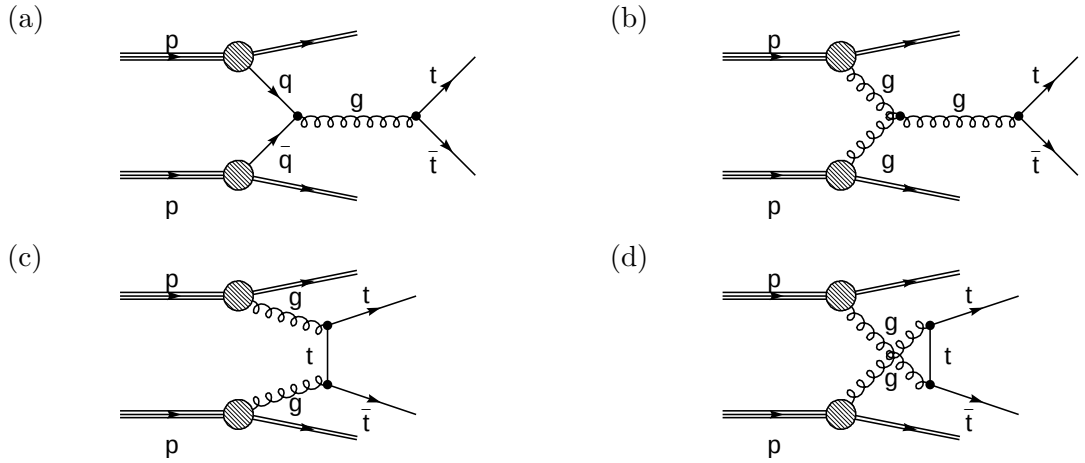

Figure 1.4.: Feynman diagrams for top quark pair production via the strong interaction. Processes at lowest order through quark-antiquark annihilation (a) and gluon–gluon fusion (b)–(d).

The total top quark pair production cross section in strong interaction processes is calculated at next-to-leading order in QCD, including gluon re-summation corrections [5, 16, 34]. A comparison to other processes over a wide range of centre-of-mass energies is shown in Figure 1.7, while numerical values are given in Table 1.3. With more than 80 million expected $t\bar{t}$-events per year, assuming $\sqrt{s} = 14\,\text{TeV}$, $\mathscr{L} = 10^{34}\,\text{cm}^{-2}\text{s}^{-1}$ and a machine efficiency of 1/3 (cf. Chapter 2), the Large Hadron Collider can be seriously called a top quark factory.

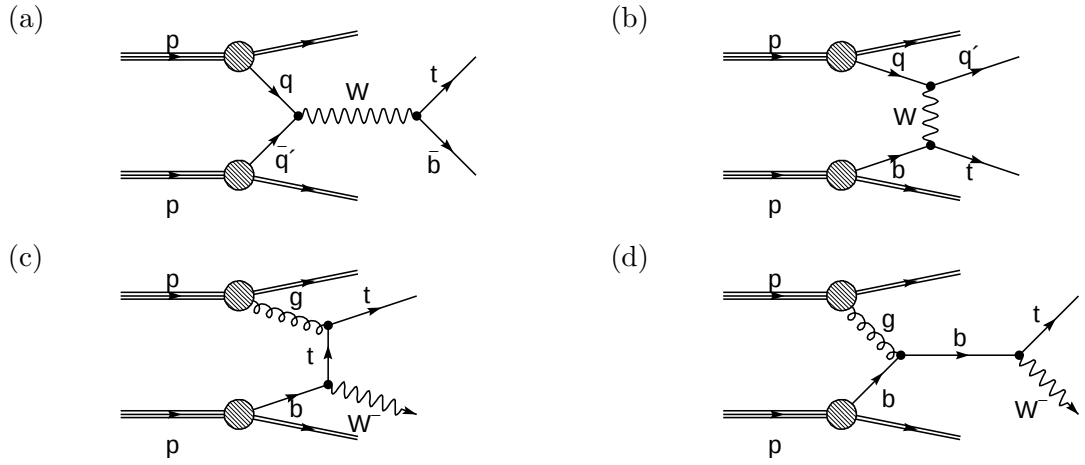

Figure 1.5.: Feynman diagrams for electroweak single top quark production at leading order: s-channel (a), t-channel (b) and Wt-production (c,d).

Electroweak Single Top Quark Production

In contrast to top quark pairs, the production of single top quarks results from electroweak interaction. At leading order, the Wtb-vertex occurs in three different processes, shown in Figure 1.5:

a) quark-antiquark annihilation (s-channel),

b) single top t-channel

c,d) and associated Wt-production.

The total cross section of single top quark events is about 60 % lower than for top quark pair events. Numerical values for each sub-process are given in Table 1.3. Single top quark production has been recently observed by the Tevatron experiments [35, 36], which allows now for the first time a direct measurement of the CKM matrix element $|V_{tb}|$ [37].

$\sqrt{s}$ [TeV]	$\sigma_{t\bar{t}}$ [pb]	$\sigma_{\text{s-channel}}$ [pb]	$\sigma_{\text{t-channel}}$ [pb]	$\sigma_{\text{Wt-channel}}$ [pb]
7	160.79	3.94	58.72	13.10
10	402.53	6.63	124.51	32.66
14	886.28	10.65	246.60	66.00

Table 1.3.: Calculated cross sections for top quark pair and single top production at the LHC for $m_t = 172.5\,\text{GeV}$ and various centre-of-mass energies. The calculation has been performed at next-to-leading order including gluon re-summation corrections [38].

1.2.2. Top Quark Decay

As mentioned above, the top quark is the only quark which decays before hadronisation, thus no top quark flavoured bound states have been observed yet. The top quark decays predominantly via electroweak interaction into a W-boson and a b-quark in almost 100 % of the cases. The decay channels t → Ws and t → Wd are strongly suppressed at tree level which is also expressed by the predicted hierarchy of the CKM matrix elements with a top quark involved V_{tx}.

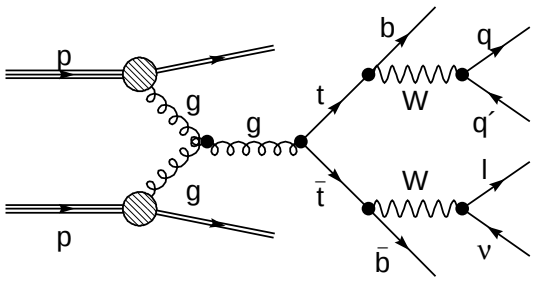

Figure 1.6.: Leading order Feynman diagram of the lepton plus jets channel in $t\bar{t}$-events.

Depending on the final states of the W-boson decay, top quark pair events can be classified into three different decay channels:

a) **di-lepton**, where both W-bosons decay into a leptonic final state,

b) **lepton plus jets**, where one W-boson decays leptonically and the other hadronically,

c) **all hadronic**, with both W-bosons decaying hadronically into a multi jet final state.

Because of the three possible colours of quarks, it is more likely for a W-boson to decay into a hadronic final state than into a leptonic one. The integrated branching ratio for each $t\bar{t}$-decay class is summarised in Table 1.4 and shows that the lepton plus jets channel and the all hadronic channel are almost at the same value while the di-lepton channel is further suppressed.

Channel	Decay	Branching Ratio	
		Born Level	measurement
di-lepton	$t\bar{t} \to bW^+\,\bar{b}W^- \to bl\bar{\nu}\,\bar{b}\bar{l}\nu$	1/9	10.3 %
lepton plus jets	$t\bar{t} \to bW^+\,\bar{b}W^- \to bl\bar{\nu}\,\bar{b}q\bar{q}'$	4/9	43.5 %
all hadronic	$t\bar{t} \to bW^+\,\bar{b}W^- \to bq\bar{q}'\,\bar{b}q\bar{q}'$	4/9	46.2 %

Table 1.4.: Integrated branching ratio of the top quark pair decay channels at Born level and the best measurement values [2].

1.2.3. Top Quark Mass

The top quark mass is a crucial, but free parameter in the Standard Model of Particle Physics and was measured in top quark pair events by the Tevatron experiments D0 and CDF [30]. Top quark mass measurements have been performed in each $t\bar{t}$-decay channel using various techniques. The three major methods established in the last years are:

a) a **Combined Fit** (CF) of signal and background, in order to determine the top quark's pole mass directly from the peak of the 3-jet invariant mass distribution,

b) the **Template Method** (TM), using Monte Carlo template distributions of variables strongly correlated to the top quark mass, generated for different mass points,

c) the **Matrix Element Method** (ME), where an event-by-event probability is calculated using the leading order $t\bar{t}$-production matrix element as a function of the reconstructed variable and the top quark mass.

The latest combined average (cf. Figure 1.7) from both Tevatron runs has a value of:

$$m_t = 173.2 \pm 0.6\,(\text{stat.}) \pm 0.8\,(\text{syst.})\,\text{GeV} \tag{1.5}$$

The average is still dominated by measurements of the lepton plus jets channel, but with an improved statistical uncertainty. In these measurements, systematic uncertainties like the jet energy scale uncertainty are dominating already over the statistical error. Thus, new analysis techniques have been recently developed for a top quark mass measurement in the lepton plus jets channel with a different dependence on the jet energy:

a) the **Decay Length Method**, measuring the transverse decay length of the b-quark jet,

b) and a template method using the **Lepton Transverse Momentum**.

Another way to indirectly extract the top quark mass is a comparison of the $t\bar{t}$ cross section measurement with its theoretical prediction from the Standard Model. The latest result obtained by the D0 collaboration is $m_t = 169.1^{+5.9}_{-5.2}\,\text{GeV}$ [39].

A top quark mass measurement will be one of the first Standard Model measurements to be performed at the Large Hadron Collider. Due to the high top quark pair production rate, the statistical error will be negligible shortly after the beginning of data-taking. The dominating systematic uncertainties occur as in the Tevatron case from the jet energy scale and final state radiation. The expected precision of a top quark mass measurement with the ATLAS detector is about $\Delta m_t \sim 1\,\text{GeV}$ [40].

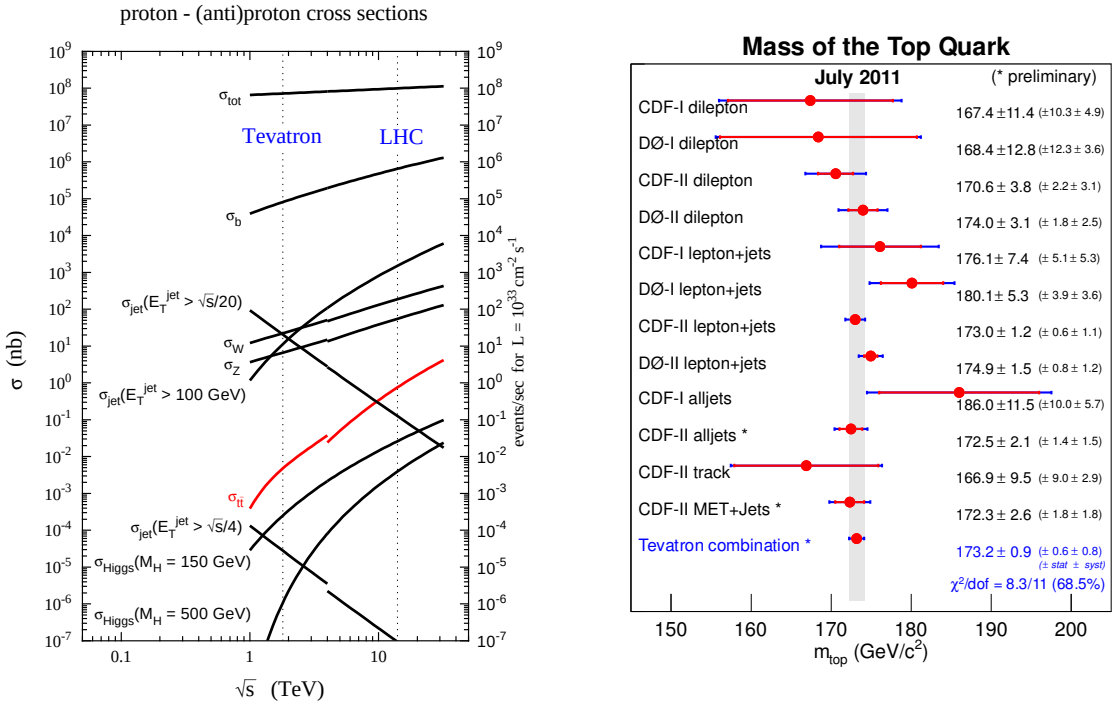

Figure 1.7.: Left: QCD prediction of the $t\bar{t}$ cross section (red) in comparison to other processes. The step at $\sqrt{s} = 4\,\text{TeV}$ is due to the change from $p\bar{p}$-scattering (Tevatron) to pp-scattering (LHC). [41] Right: Summary of the input measurements and resulting world average of the top quark mass measurements. [30]

2. The ATLAS Experiment at the Large Hadron Collider

In this chapter, the technical design of the Large Hadron Collider and the ATLAS detector are briefly described. In addition, the expected performance based on detector simulation and test-beam measurements is presented for each sub-detector of the ATLAS experiment.

2.1. The Large Hadron Collider

The **Large Hadron Collider** (**LHC**) [42] is a particle ring accelerator located in the 26.7 km long tunnel of the former Large Electron-Positron Collider (LEP) at CERN near Geneva (CH). It is built for accelerating and colliding protons or heavy ions in two oppositely circulating beams with an energy up to 7 TeV per proton. This unprecedented acceleration power is achieved with eight superconducting radio frequency (RF) cavity modules at 400 MHz. In order to deflect and focus the two beams, 1232 superconducting dipole magnets with a field strength of up to 8.3 T plus 8361 higher order multi-pole magnets are built in. For reaching and keeping the superconductivity range of the cold masses, the cooling system provides fluid helium at a temperature of 1.9 K.

At four interaction points, the 2808 particle bunches per beam are brought to collision with a bunch crossing time of 25 ns (40 MHz). With on average $1.1 \cdot 10^{11}$ protons per bunch a design luminosity of $\mathscr{L} = 10^{34}\,\mathrm{cm}^{-2}\mathrm{s}^{-1}$ can be achieved. Assuming a duty fraction of 1/3, an integrated luminosity of $100\,fb^{-1}$ collision data can be taken per year. At design luminosity, approximately 23 proton-proton collisions are expected per bunch crossing including 1-2 hard interactions with high transverse momentum. Due to the substructure of the protons, only a fraction of 1-2 TeV from the centre-of-mass energy of $\sqrt{s} = 14$ TeV will be present in the hard parton-parton processes. An analysis of those interesting physics events allows one to research a wide range of high energy particle physics, for example:

a) searches for the Higgs boson,

b) further tests of the standard model as top quark physics,

c) or searches for indications of physics beyond the SM, e.g. super-symmetric particles.

Nevertheless, it will be crucial for any physics analysis to study the remaining minimum bias events in order to understand this important physics background as well as noise contributions.

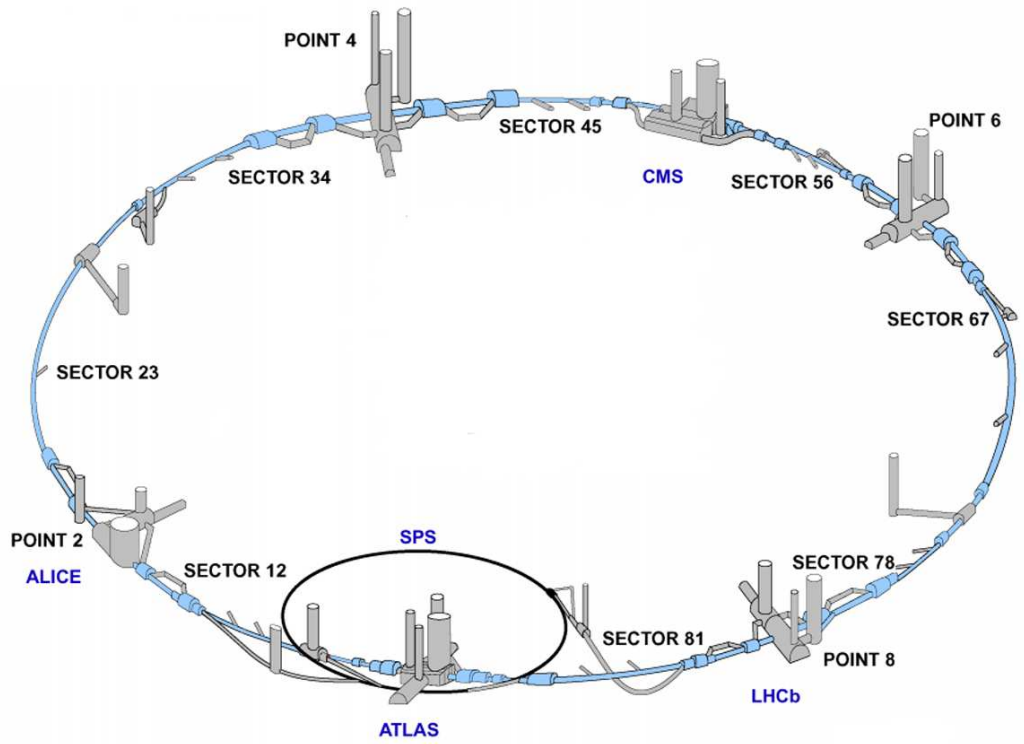

Figure 2.1.: Schematic view of the Large Hadron Collider at CERN. The pre-accelerator SPS is indicated as well as the four major experiments ATLAS, CMS, LHCb and Alice.

The major experiments at the LHC to study high energetic proton-proton collisions are built at the four interaction points as shown in Figure 2.1. The ATLAS detector at Point 1 is the biggest of them and devoted to a wide range of LHC physics. At the opposite site at Point 5, another multi-purpose experiment, CMS [43], is located. Both experiments, ATLAS and CMS, are typical symmetric multi-layer detectors including tracking system, calorimeters and muon detectors and provide independent measurements of the same physics quantities.

At Point 8, the more specific experiment LHCb [44] was built in order to study mainly B-meson physics including the phenomenon of $\mathcal{CP}$-violation. In contrast to ATLAS and CMS, the LHCb detector has a non-hermetic design and is optimised for B-meson tagging. Finally, there is the ALICE [45] experiment at Point 2 with the focus on heavy ion collisions. It has been optimised to deal with very high particle densities and researches for example the quark-gluon plasma.

After 10 years of data-taking, presumably in 2020, an upgrade of the Large Hadron Collider is planned in order to achieve a ten times higher luminosity up to $\mathscr{L} = 10^{35}\,\mathrm{cm}^{-2}\mathrm{s}^{-1}$. This and the limited lifetime of several detector components will also require an upgrade of all LHC experiments.

2.2. The ATLAS Detector

ATLAS (**A** **T**oroidal **L**HC **A**pparatu**S**) [46, 40] is a multi-purpose detector with a typical multi-layer design. It has a cylindrical shape of 44 m length, a diameter of 25 m and weighs about 7000 tonnes. The design of the ATLAS detector is shown in the schematic view in Figure 2.2 and can be subdivided into the following three major components:

a) an **Inner Detector System** to reconstruct the trajectories of charged particles,

b) a **Calorimeter System** to measure the energies carried by the particles

c) and a **Muon Spectrometer** to determine the momentum of muons.

A characteristic feature of the ATLAS detector is its large superconducting air-core toroid system. It generates a large magnetic field for the muon spectrometer, minimising the amount of intermediate material and thus multiple scattering. In order to handle the high luminosity provided by the LHC, each detector component has been optimised to radiation hardness and an efficient 3-level trigger system has been developed.

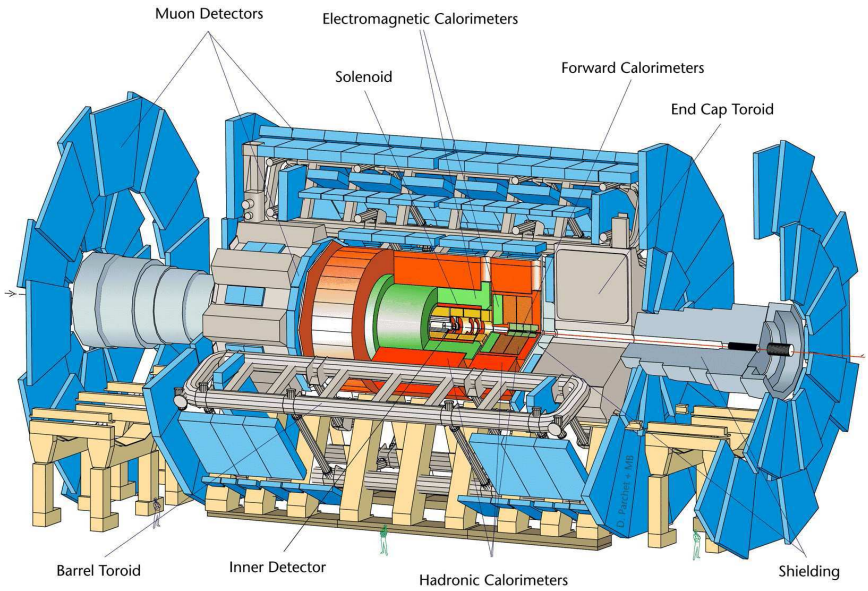

Figure 2.2.: Schematic view of the ATLAS detector.

The ATLAS experiment is devoted to the whole wide range of LHC physics and has even a research programme for heavy ion collisions. The detector development and operation as well as the data analysis is performed within the ATLAS collaboration, an international organisation of more than 3000 people from 173 institutes in 37 countries.

The coordinate system of ATLAS is a right-handed system with the origin at the nominal interaction point. From there, the x-axis is pointing to the centre of the LHC ring, the y-axis is going upwards and the beam direction defines the z-axis, pointing to LHC Point 8 with a slope of $-1.23\,\%$. The part of the detector with positive z is defined to be the A-side, while negative z indicate the C-side.

The azimuthal angle $\phi = 0$ corresponds to the positive x-axis and increases clock-wise looking into the direction of positive z. It is measured in the range $[-\pi, +\pi]$. The polar angle θ is measured from the positive z-axis in the range of $[0, +2\pi]$. On hadron colliders, the pseudo-rapidity η is preferred over the angle θ, because of the Lorentz boost invariance of $\Delta\eta$ along the beam axis. The pseudo-rapidity is defined as:

$$\eta = -\ln\left[\tan\left(\theta/2\right)\right]. \tag{2.1}$$

With the usage of η, a distance ΔR in the pseudorapidity-azimuthal angle space is defined as:

$$\Delta R = \sqrt{\Delta\eta^2 + \Delta\phi^2} \tag{2.2}$$

Unless stated otherwise, all transverse variables like the transverse momentum p_T, the transverse energy E_T and the missing transverse energy $E_{\mathrm{T}}^{\mathrm{miss}}$ are defined in the x-y plane, perpendicular to the LHC beam axis.

2.2.1. The Inner Detector System

The **Inner Detector System** (**ID**) consists of three different tracking devices and the central solenoid magnet. A schematic view is shown in Figure 2.3. It allows the trajectories of charged particles to be reconstructed in order to measure the positions of the primary vertex and of possible secondary vertices from heavy flavour decays. Furthermore, the particle momenta are measured with high precision from the track curvature in the magnetic field of the central solenoid. This allows also a determination of the sign of the charge of the particle.

The **Pixel Detector** (**PIX**) is the inner most tracking device. It is 1.3 m long and has a diameter of 300 mm. It consists of 1744 rectangular modules of the size 19 mm $\times$ 63 mm, where each sensor has 46080 pixel of the size 50 μm $\times$ 400 μm. 1456 of these modules are located in the 3 cylindrical barrel layers while the remaining 2×144 modules are in the 2×3 endcap disks. Since the minimum distance to the beam line is only 50.5 mm, the development of the pixel detector required radiation hardness in a special manner. The pixel detector is with 80.4 million readout channels the sub-detector with the highest granularity.

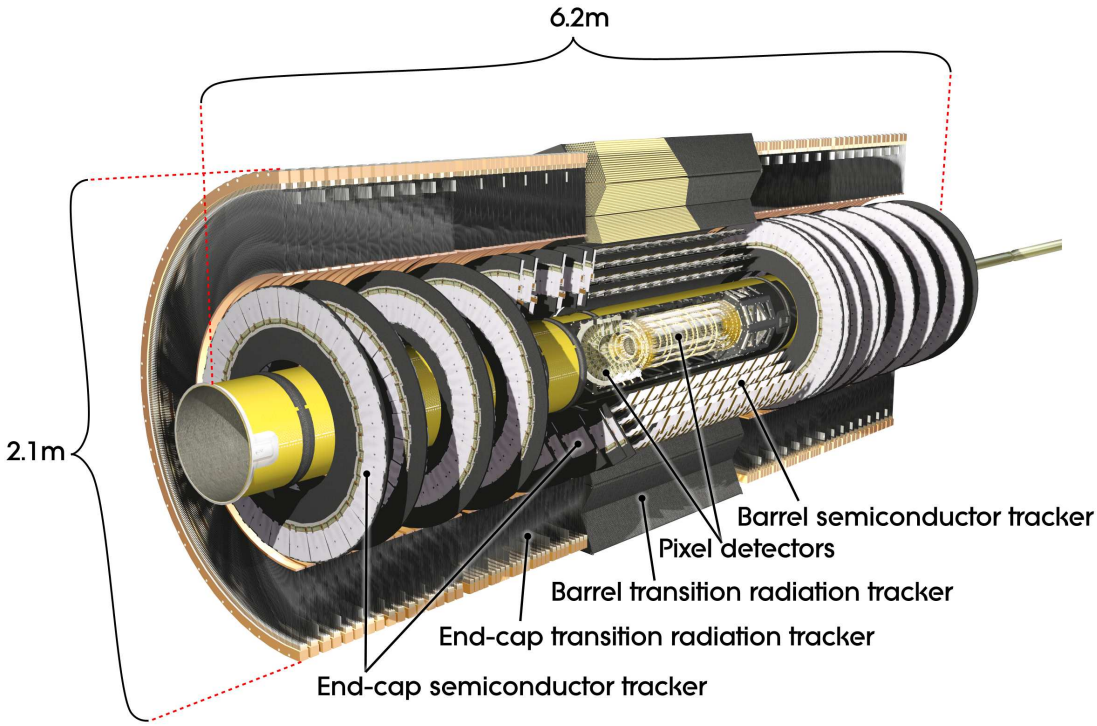

Figure 2.3.: Cut-away view of the ATLAS inner detector system.

The **Semiconductor Tracker** (**SCT**) is designed to provide additional precision space point measurements per track and covers $|\eta| < 2.5$. Each of the 4088 SCT modules consists of single sided 80 μm pitch silicon strip sensors. The two sensors per module are rotated by a stereo angle of 40 mrad in order to obtain a measurement of the z-coordinate. The modules are arranged in four barrel layers at radii of 300, 373, 447 and 520 mm plus nine endcap disks on each side. With its 6.3 million readout channels, the SCT has a fundamental impact on the track reconstruction.

The **Transition Radiation Tracker** (**TRT**) is the outer tracker of ATLAS. It is a combined straw tube tracker and transition radiation detector. The TRT consists of 350000 kapton straw tubes with a diameter of 4 mm. The straw tubes are filled with a $Xe/CO_2/O_2$ gas mixture. The 30 mm thick readout anode is made from gold plated tungsten-rhenium wire. As transition radiation material polypropylene fibres (barrel) and foils (endcap) are used which allows for electron identification. In average, the TRT provides 36 hits per track and has an important impact on the track momentum resolution.

The magnetic field for the three tracking detectors is provided by the **Central Solenoid**. It covers an inner diameter of of 2.5 m and a length of 5.8 m with a homogeneous 2 T axial magnetic field. The superconducting solenoid magnet consists of a steel barrel equipped with Al/NbTi coil windings and is operated at a temperature of 4.5 K. In order to minimise the built-up material in front of the calorimeters, it shares the cryostat with the liquid argon calorimeters where the iron absorber of the tile calorimeter is used as return yoke.

2.2.2. The Calorimeter System

In addition to a precision track and momentum measurement, the energy measurement for all final state particles is crucial for most of the physics analyses. Here, the ATLAS calorimeter system [46] plays a central role and provides a precision energy measurement for electrons and photons as well as for particle jets initiated by quarks and gluons. It allows further for a measurement of the particles direction due to its reasonable granularity and its hermetic coverage in ϕ and in pseudo-rapidity up to $|\eta| < 4.9$. This is in particular important for neutral particles, which do not leave tracking hits in the inner detector. Combining both, energy and direction measurement, allows to determine missing transverse energy ($E_{\mathrm{T}}^{\mathrm{miss}}$) with high resolution, an important variable in order to identify neutrinos or super-symmetric particles.

All ATLAS calorimeters are based on the heterogeneous sampling calorimeter technique and thus consist of alternating layers of absorber and active material. Here, the energy of particles to be measured is mostly absorbed by showering up in the absorber material layers. While passing the active material in between, these showers of secondary particles create a signal proportional to the deposited energy of the initial particles.

In general, the average ratio between signals from electromagnetic and hadronic particles (e/h) of the same initial energy is material- and energy-dependent. As for non-compensating calorimeters, the response for electromagnetic particles is higher than for hadronic particles (e/h > 1) in the ATLAS calorimeters system. Finally, a dedicated calibration strategy for both classes is needed in order to set the absolute energy scale of the calorimeters. In order to achieve a very good signal response linearity over a wide energy range, the detector material chosen has been optimised for the different needs of the specific electromagnetic and hadronic calorimeter parts. Furthermore, a small spatial energy resolution $\sigma(E)/E$ is important, in particular for precision measurements. The energy resolution can be generally parametrised as the quadratic sum ($\oplus$) of three terms with different origin:

$$\frac{\sigma(E)}{E} = \frac{a}{\sqrt{E}} \oplus b \oplus \frac{c}{E}. \tag{2.3}$$

Here, the first term, referred to as sampling term, accounts for intrinsic statistical shower fluctuations. The second term, referred to as constant term, accounts for leakage energy due to incomplete containment of a shower in the calorimeter, inhomogeneities inside the calorimeter in general and the non-compensating characteristic (e/h $\neq 1$). The last term describes the electronics noise. The $1/E$-dependence ensures its constance at all energies for fixed size clusters.

For the layout of the ATLAS calorimeter system, two different technologies are used. The inner part is based on a Liquid Argon (LAr) technology, thus LAr as active material combined with different absorber materials. The signal is induced by ionisation of the LAr and the deposited charge is collected using a high voltage electric field.

As copper-coloured indicated in Figure 2.4, the LAr calorimeter system is sub-divided in four components: the electromagnetic barrel calorimeter (EMB), the electromagnetic endcap calorimeters (EMEC), the hadronic endcap calorimeters (HEC) and the forward calorimeters (FCal). In order to keep the liquid argon at its operation temperature of about 80 K, the LAr calorimeters are housed in three cryostats, one for the barrel and two for the endcap calorimeters.

Only the outermost part of the ATLAS calorimeter system, the hadronic tile calorimeter (Tile), is based on a different technology and thus is operated at room temperature. It is based on steel absorber plates and plastic scintillators as active material. The Tile calorimeter, indicated in grey in Figure 2.4, includes the barrel part as well as the two extended barrel partitions, which enclose the cryostats housing the LAr endcap calorimeters.

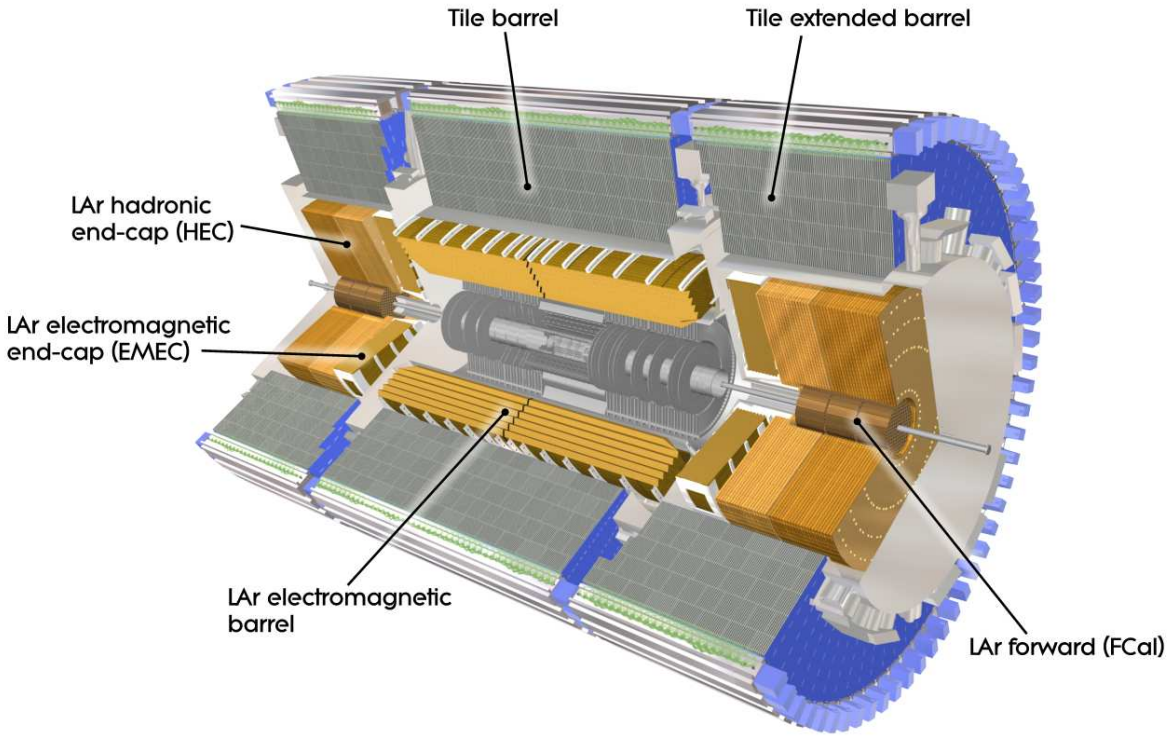

Figure 2.4.: Schematic view of the ATLAS Calorimeter System.

The **Electromagnetic Barrel Calorimeter (EMB)** consists of two cylinders and covers the central region within $|\eta| < 1.475$. The absorber material chosen is lead, which is sandwiched between 0.2 mm stainless steel foil for mechanical support. The readout electrodes in the LAr filled gaps are kept in position between the absorber plates by a honeycomb spacer-mat. As shown in Figure 2.5, a complex accordion shape geometry was chosen in order to guarantee a fast signal collection and to avoid any discontinuities in the ϕ-coverage. The accordion waves are axial, thus the signals in the different samplings are collected on one electrode which makes a further summation unnecessary.

The EMB has three sampling layers within $|\eta| < 1.35$, and two layers in the regions up to $|\eta| < 1.475$. The cell size of the first layer is about $\Delta\eta \times \Delta\phi = 0.025/8 \times 0.025$ and becomes coarser in the outer layers. This results into a shower containment of the calorimeter between $24 - 33$ radiation lengths (X_0), depending on the η region. The sampling fraction of the EMB is about $16 - 20\,\%$ and varies with ϕ as consequence of the accordion geometry.

A characteristic feature of the electromagnetic calorimeters is the finely segmented presampler in front, housed in the same cryostats. It is a first active LAr layer of 11 mm and provides a first sampling information which helps for electron/photon identification and to distinguish the $\pi^0 \to \gamma\gamma$ decay from other photons. Furthermore, the presampler provides information to identify energy losses in material in front of the calorimeters, mainly due to cryostat walls and the barrel solenoid. This is an important input to the calorimeter energy calibration.

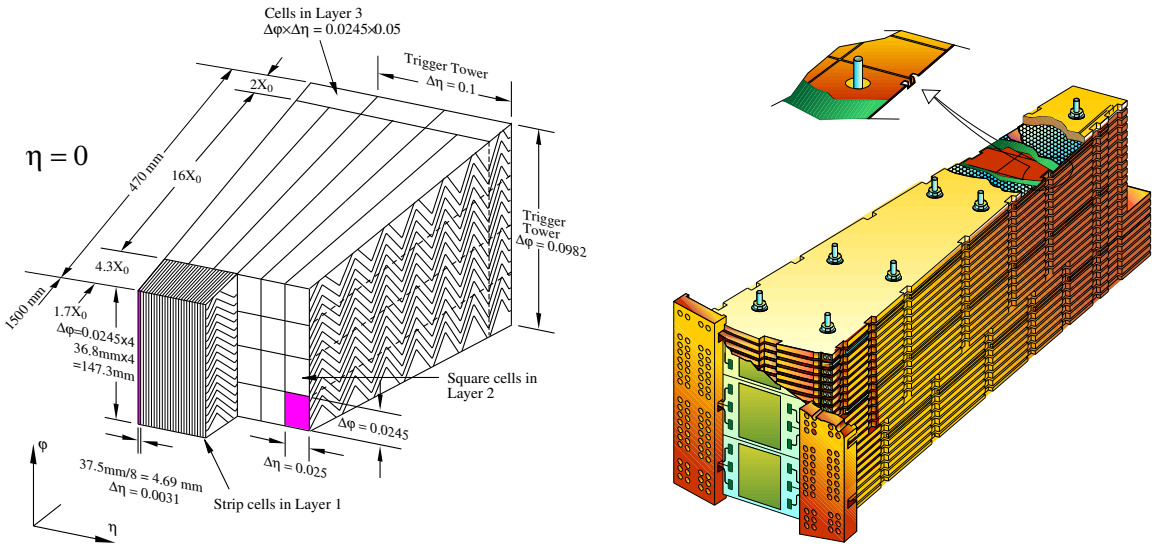

Figure 2.5.: Left: Sketch of an EMB module. The different layers are clearly visible with the convolution of the electrodes in ϕ. The cell granularities in η and ϕ are shown for each of the three layers and the trigger towers. [46]. Right: Artist's view of one HEC module (ϕ-wedge) [46]. On the outer side, the pre-amplification and summing boards are indicated and the zoom in shows the readout electrode at the position of a tie rod.

The **Electromagnetic Endcap Calorimeter (EMEC)** is based on the same technology and design as the EMB and covers the two endcap regions within $1.375 < |\eta| < 3.2$. In contrast to the EMB, the accordion waves are arranged in radial direction. With increasing radius, the accordion wave "amplitude" and hence the LAr gap since increases, while the absorber thickness is kept constant. This requires the high voltage to vary with the radius in order to keep the electric field strength, and thus the drift time constant.

Like the EMB, the EMEC has either two or three sampling layers depending on the η region and a presampler layer in front. The cell sizes vary from $\Delta\eta \times \Delta\phi = 0.025 \times 0.025$ to $\Delta\eta \times \Delta\phi = 0.1 \times 0.1$ and the shower containment is between 24 and $38\,X_0$. The sampling fraction in the EMEC is about $7 - 10\,\%$ and varies with η due to the orientation of the accordion waves.

The two **Hadronic Endcap Calorimeters (HEC)** are housed in the same cryostats as the EMEC and cover the region of $1.5 < |\eta| < 3.2$. Each side is structured in two wheels, HEC1 and HEC2, with two layers per wheel. The HEC has a classical geometry of alternating layers of LAr and ultra-pure copper absorber plates, arranged vertical to the beam axis.

As shown in Figure 2.5, these copper plates are stacked to ϕ-wedges on stainless steel tie rods and have a thickness of 25 mm in the front wheel (HEC1) and 50 mm in the rear wheel (HEC2). The LAr gap width of 8.5 mm is guaranteed by honeycomb spacer on the tie rods between the copper plates. The LAr gaps are sub-divided into four sub-gaps by the readout and high voltage electrodes as illustrated in Figure 2.6.

The sampling fraction in the HEC is constant in each wheel, due to its simpler geometry compared to the electromagnetic calorimeters. It is 4.4 % in the front wheel and 2.2 % in the rear wheel, where the copper absorber plates are double as thick. The hadronic shower containment of the HEC is in total about 11 hadronic interaction length (λ_I). The cell size of the HEC is constant in η and ϕ with smaller cell sizes of $\Delta\eta \times \Delta\phi = 0.1 \times 0.1$ for $|\eta| < 2.5$ and bigger cell sizes of $\Delta\eta \times \Delta\phi = 0.2 \times 0.2$ for $|\eta| > 2.5$.

The characteristic feature of the HEC is its readout electronics, which is partly located inside the cryostat and thus is operated at temperatures of about 80 K (cold electronics). The advantage of having the signal summation as well as a pre-amplification in the cold is a reduced electronics noise level and a faster signal summation. This allows in particular to keep the third term of the energy resolution parametrisation relatively small.

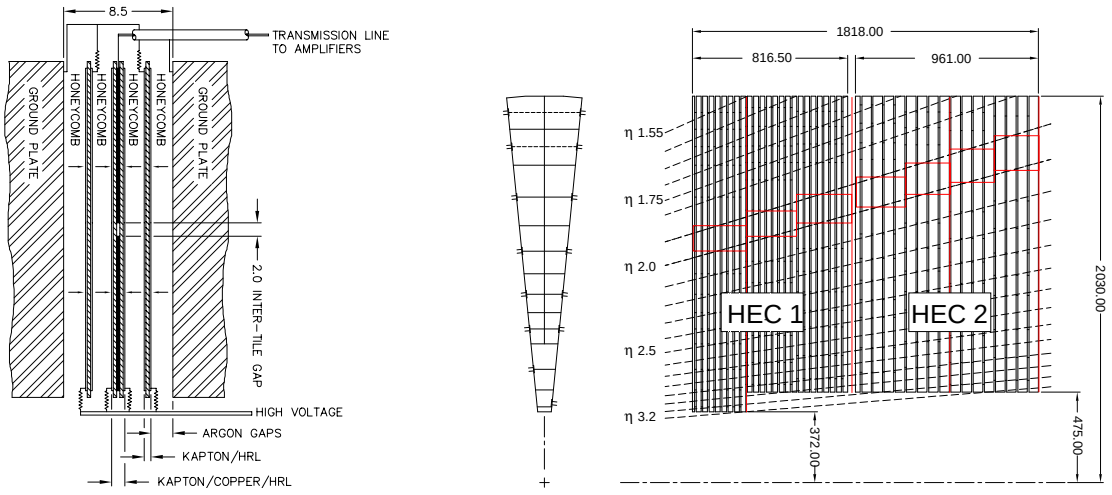

Figure 2.6.: Left: The HEC LAr gap between two copper plates with the Electro Static Transformer (EST) consisting of three different high voltage (HV) and readout boards, separated by a honeycomb spacer [47]. Right: Schematic $R - \phi$ (left) and $R - z$ (right) view (dimensions in mm) of the hadronic endcap calorimeter [47]. The semi-pointing layout of the readout electrodes is indicated by the dashed lines, while the red lines show the cells in the four samplings.

The third calorimeter housed by the endcap cryostats is the **Forward Calorimeter (FCal)**. It covers the region closest to the beam pipe within $3.1 < |\eta| < 4.9$ and thus requires to be optimised to radiation hardness. The FCal is sub-divided into three segments: the front one, with copper as absorber material, serves as electromagnetic part while the two rear segments with tungsten absorber serves as hadronic calorimeter. Also the layout of the FCal modules follows a different design. Tubes holding the cylindrical electrodes are inserted in a matrix of absorber material and form a cylindrical shell LAr gap as shown in Figure 2.7. Depending on the module, the gap size varies from 269 to 508 μm.

The size of the readout cells increases outwards from $\Delta x \times \Delta y = 3.0 \times 2.6\,\mathrm{cm}^2$ in FCal1 over $\Delta x \times \Delta y = 3.3 \times 4.2\,\mathrm{cm}^2$ in FCal2 up to $\Delta x \times \Delta y = 5.4 \times 4.7\,\mathrm{cm}^2$ in FCal3. In general, the cells at the inner radius of all three FCAL layers are slightly smaller. The total shower containment of the combined FCal segments is about $210\,\mathrm{X}_0$ and $10\,\lambda_\mathrm{I}$, where FCal1 with the finest granularity has $29\,\mathrm{X}_0$. Since the geometry is not pointing to the interaction point, the sampling fraction depends strongly on the particles incident angle which is in average in the order of 1 %.

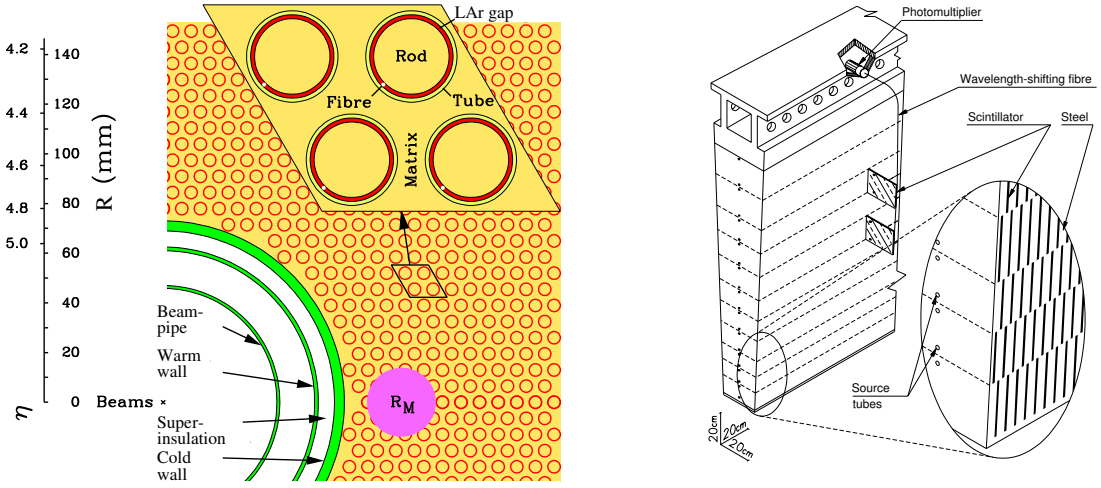

Figure 2.7.: Left: Electrode structure of the first FCal module [46]. The copper matrix, tubes and rods with the LAr gaps are indicated. Right: Sketch of a Tile calorimeter segment including the optical readout system.

The outermost part of the ATLAS calorimeter system is the hadronic **Tile Calorimeter**. It covers the region within $|\eta| < 1.7$ and is composed of three partitions: one central barrel plus two extended barrels enclosing the endcap cryostats. The name refers to the geometry, where tiles of plastic scintillator are used as active material, combined with steel absorber plates. The characteristic feature of its design is the orientation of the scintillating tiles which are placed in planes perpendicular to the colliding beams and are staggered in depth. The signal (scintillation light) produced by the particle shower in the scintillator tiles is read out by wavelength-shifting optical fibres and amplified by photo-multipliers tubes, which guarantees a fast response time.

The schematic view of a Tile calorimeter module in Figure 2.7 shows the orientation of the scintillator tiles perpendicular to the beam line. But even in the very central region, where the particle trajectories are nearly parallel to the sampling layers, the lateral shower fluctuations are large enough in order to generate a signal. All Tile calorimeter partitions have three sampling layers with a cell granularity of $\Delta\eta \times \Delta\phi = 0.1 \times 0.1$. Depending on the η-region, the shower containment ranges from $8 - 14\,\lambda_{\mathrm{I}}$ and the sampling fraction is in the order of 3 %.

The ATLAS calorimeter system consists in total of 187652 cells (channels). In order to extract a well calibrated energy measurement per cell, the LAr and Tile calorimeters have very precise charge-injection and calibration systems to calibrate the response of the front-end electronics boards. The aim of the LAr electronics calibration is to determine calibration factors to interpret the measured ADC counts into a current in μA. For this purpose, a well defined calibration pulse from the special calibration boards is injected into the read out chain. The final conversion factors to transform the signal from μA into GeV has been obtained from test-beam measurements and agree with predictions based on detector simulations. The Tile calorimeter calibration system can be divided into three independent parts. A charge injection system for the front-end electronics, a laser system to calibrate the photo-multipliers and finally a ^{137}Cs-γ source for the scintillator tiles and the optical system.

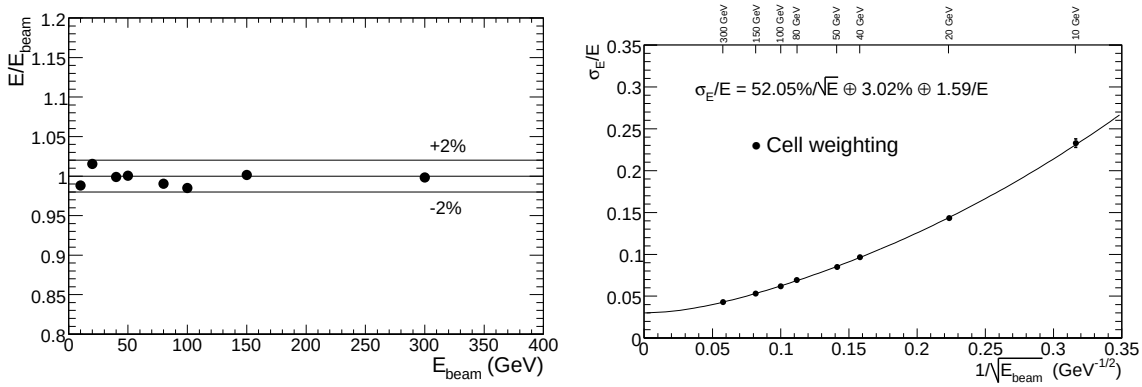

Figure 2.8.: Linearity (left) and fractional resolution (right) of the energy response as function of the pion beam energy E_{beam} for combined LAr and Tile calorimeter test beam corresponding to $|\eta| = 0.25$ [48]. The curve in the right plot corresponds to the result of a fit to the data points with the functional form as described in Equation 2.3 [48].

Also the performance of the ATLAS calorimeter system has been studied in detail with dedicated test-beam setups [49, 48]. Figure 2.8 shows the combined performance of the electromagnetic LAr barrel and the hadronic Tile calorimeter in test-beam measurements. The hadron beam consisted of pions with an energy dependent proton component. It is shown, that the hadron response deviation from linearity is within 2 % over the entire beam-energy range from 10 to 300 GeV. Furthermore, the fractional energy resolution is well fitted by the sum in quadrature:

$$\frac{\sigma(E)}{E} = \frac{(52.0 \pm 1.0)\,\%}{\sqrt{E}} \oplus (3.0 \pm 0.1)\,\% \oplus \frac{1.6\,\mathrm{GeV} \pm 0.1\,\%}{E}. \tag{2.4}$$

2.2.3. The Muon Spectrometer

Except of neutrinos, which cannot be measured with the ATLAS detector, muons are the only particles passing the calorimeter system. Since muons are crucial for many Higgs boson and top quark related analyses, a very precise measurement of their transverse momenta is required. The ATLAS Muon Spectrometer provides such a clean muon identification and a precise determination of the transverse momentum up to 1 TeV. It is the outermost subdetector and is instrumented with dedicated tracking and trigger chambers as shown in Figure 2.9. In the barrel region they are installed in three cylindrical layers around the beam axis at radii of about 5, 7.5 and 10 m. The chambers in the endcap regions are arranged in four wheels perpendicular to the beam axis at distances in z of 7.4 m, 10.8 m, 14.0 m and 21.5 m from the primary vertex position. The precision momentum measurement is finally based on the magnetic deflection of the muon tracks in the magnetic field generated by three air-core toroids.

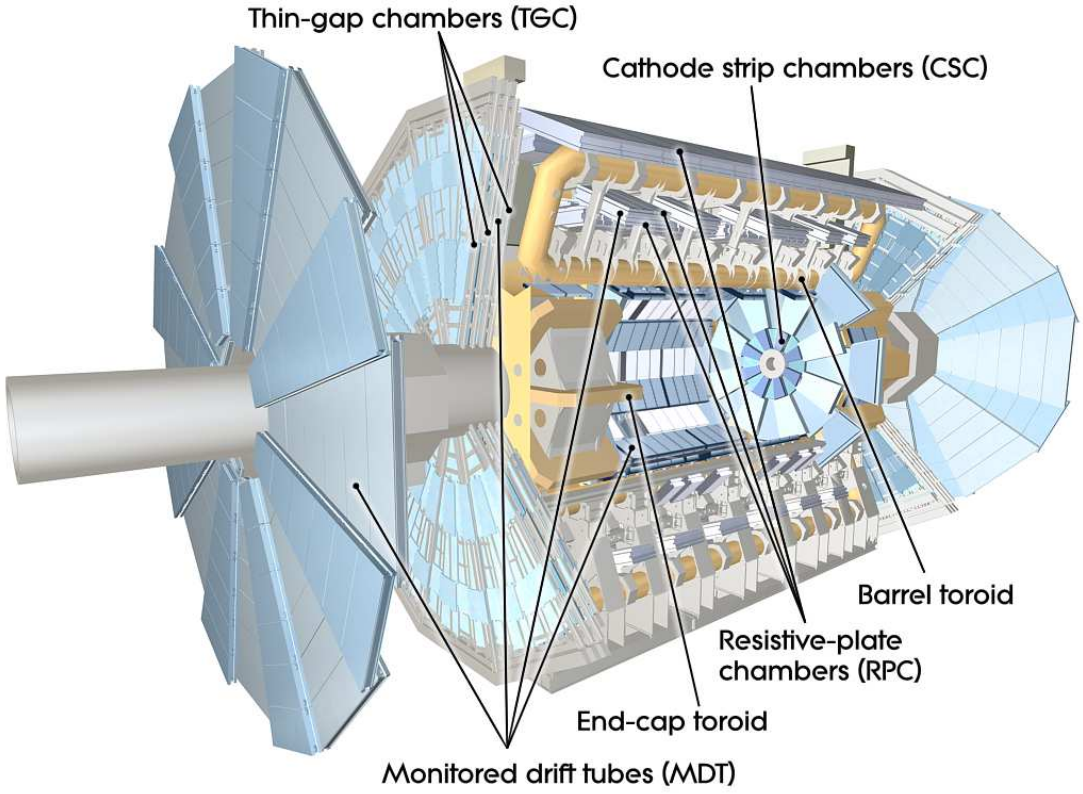

Figure 2.9.: Schematic view of the ATLAS Muon Spectrometer System.

The first kind of tracking chambers are equipped with **Monitored Drift Tubes (MDT)** and cover the central region up to $|\eta| < 2.0$. These aluminium tubes have a diameter of 30 mm and are filled with an $\mathrm{Ar}(93\,\%)\mathrm{CO}_2(7\,\%)$ gas mixture at a pressure of three bar. The coaxial readout anode wire is made from a tungsten-rhenium alloy. At an operation voltage of 3080 V, the maximal drift time is about 700 ns and gives a spatial resolution of about 80 μm for a single tube or about 35 μm per chamber.

In the innermost layer of the endcap wheels, thus in the forward region between $2.0 < |\eta| < 2.7$, another kind of tracking chambers is needed due to the high particle fluxes. These **Cathode Strip Chambers (CSC)** are multi-wire proportional chambers with strip-segmented cathodes. In the bending plane the spatial resolution per chamber is about $35\,\mu$m and in contrast to the MDT chambers, the CSCs provide also a rough measurement of the ϕ-coordinate with a resolution of about 5 mm.

Also the trigger chambers are equipped with two different techniques. The **Resistive Plate Chambers (RPC)** cover the barrel region and consist of two parallel electrode plates spanning a 2 mm wide gap filled with a $C_2H_2F_4/\mathrm{Iso}-C_4H_{10}/SF_6$ (94.7/5.0/0.3 %) gas mixture. The RPCs are read out by metallic strips on the outer faces via capacitive coupling. The operation can be either in avalanche or streamer mode at an electric field of $\sim 4.9\,\mathrm{kV/mm}$. The spatial resolution of the RPCs is about 10 mm in the z- as well as in the ϕ-coordinate.

In the regions of higher η-values between $1.5 < |\eta| < 2.4$, **Thin Gap Chambers (TGC)** are used as trigger chambers. In order to deal with the higher muon rates in the forward region, the TGCs are multi-wire proportional chambers. Here "thin" refers to the fact, that the wire-to-cathode distance of 1.4 mm is smaller than the wire-to-wire distance of 1.8 mm. In order to cope with the high muon rate, a higher granularity in combination with a highly quenching gas mixture of CO_2 and $\mathrm{n}-C_5H_{12}$ (n-pentane) is used. The spatial resolution of these TGCs is about $2-6$ mm in the radial component and $3-7$ mm in the ϕ-measurement.

In order to measure the momenta of charged particles, a magnetic field is essential. In the case of the ATLAS muon spectrometer, the magnetic field is provided by three large air-core toroid magnets. The reason to choose an air-core toroid system is to minimise the material to be passed by the muons and thus multiple scattering effects. These toroids are 25 m long in the barrel and 5 m long the two endcap regions. Each of them consists of eight coils arranged symmetrically around the beam axis.

As shown in Figure 2.9, the endcap toroids are located in the forward region of the detector, right after the hadronic endcap calorimeters, but still inside the barrel toroid. In contrast to the barrel toroid, where each coil is placed in a separate vacuum vessel, there is only one vacuum vessel per endcap toroid. At a nominal operation current of 20.5 kA, the barrel toroid provides a magnetic field strength in the range of $0.2-2.5$ T, whereas the endcap toroids have an enlarged range of $0.2-3.5$ T. In order to provide radial overlap and to optimise the bending power in the interface regions of both coil systems, the endcap coils systems are rotated by 22.5 degree with respect to the barrel toroid.

2.2.4. Trigger and Data Acquisition

With all proton bunches filled and a bunch crossing time of 25 ns, the total event rate in the ATLAS detector is 40 MHz. Even if it would be interesting to record and analyse each event, the data recording is limited to about ~ 200 Hz (~ 300 MB/s) by offline computing power and storage capacity. In order to reduce the event rate by selecting and recording interesting physics events only, a fast and highly efficient trigger and data acquisition system has been set up. In order to achieve these requirements, the ATLAS trigger system is composed of three consecutive levels of event selection: the hardware based **Level 1** (**L1**), the **Level 2** (**L2**) and the final **Event Filter** (**EF**). The L2 and the EF are based on software algorithms and collectively referred to as **High Level Trigger** (**HLT**). Each level is using more detailed information in order to refine the decision with respect to the previous level.

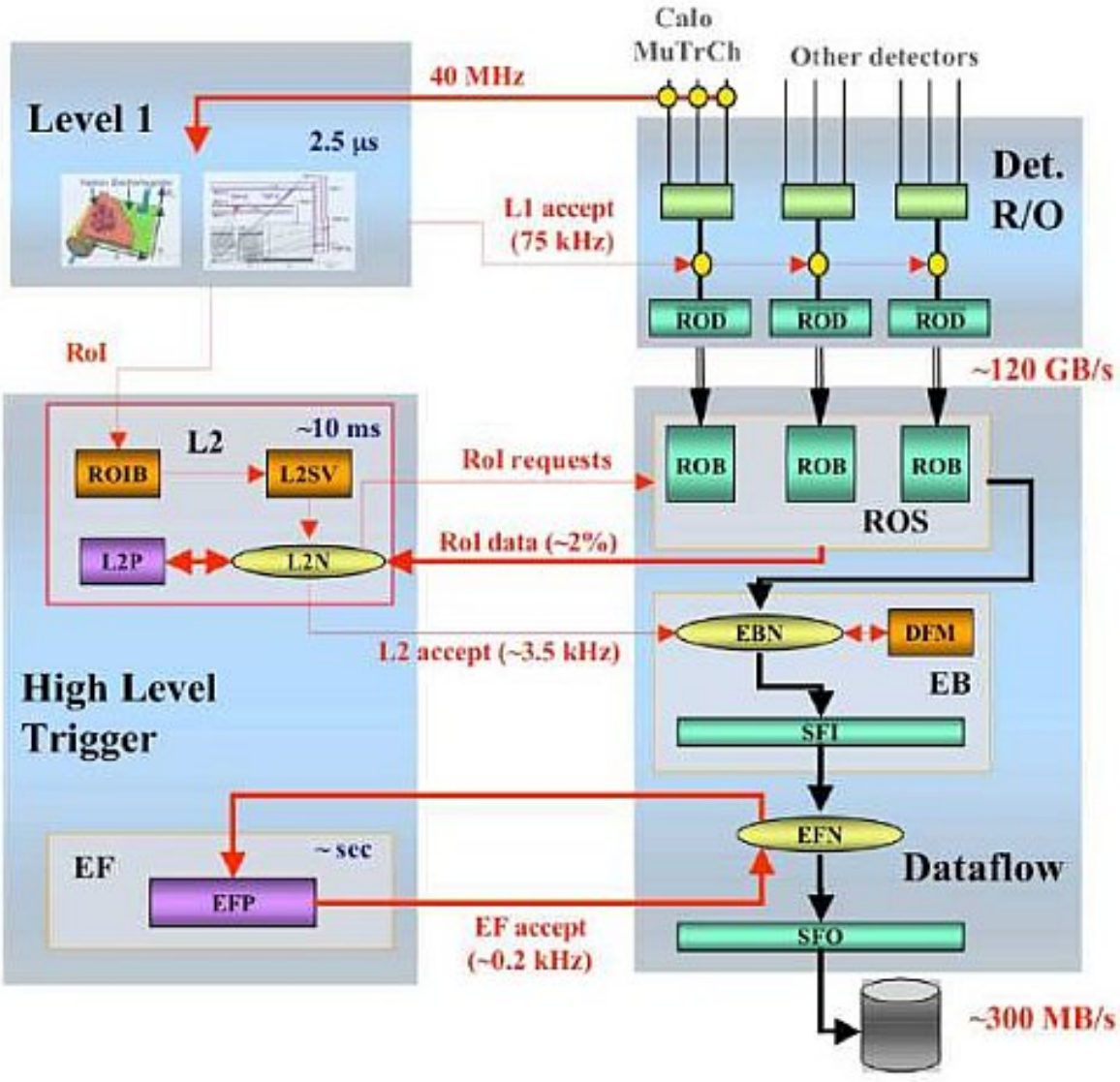

Figure 2.10.: Sketch of the ATLAS trigger system.

In a first step, the hardware based Level 1 trigger decision is used to decrease the initial event rate of 40 MHz down to 75 kHz ($\sim$ 120 GB/s), limited by the bandwidth of the readout system. This decision, made within 2.5 μs, is based on information from the calorimeter and muon systems only. The ATLAS calorimeters provide energy information with a reduced granularity (L1 trigger towers). That allows events with large missing and total transverse energy or groups of high energetic trigger towers to be selected. In addition, events with high transverse momentum muons are selected using information from the muon trigger chambers. At the end, the L1 trigger defines in each selected event a so-called **Regions of Interest** (**RoI**), i.e. those η-ϕ-regions, where interesting patterns for the decision have been identified.

These RoIs, about $\sim$ 2 % of the data, are investigated in more detail by the Level 2 trigger. Here, the decision is based on software algorithms, using pre-reconstructed information from all available sub-detectors at full granularity and precision. The processing is performed on a dedicated farm of computers, returning a decision within 40 μs. Finally, all events fulfilling the L2 trigger conditions are passed to the Event Builder (EB) with an output event rate of about 3.5 kHz ($\sim$ 2 GB/s).

The final online event selection is performed at the Event Filter level, using software algorithms to reduce the event rate down to 200 Hz ($\sim$ 300 MB/s). It has direct access to the complete data for each event and the reconstruction is usually performed using the more refined offline reconstruction algorithms. The event processing time of the EF is about 4 s. Following the EF decision, dedicated trigger streams are defined, e.g. all events with at least one muon with a transverse momentum of $p_T > 10$ GeV (`EF_mu10`).

All events selected by the trigger system are recorded on a mass-storage for further distribution and reconstruction. But the enormous data volume of approximately 1 PB/year cannot be stored and processed on a single local computing centre. Therefore, the recorded data is distributed to a worldwide, hierarchical organised grid of computing centres, the **LHC Computing Grid** (**LCG**). Here, the full reconstruction of the data as well as the physics analyses are performed.

3. Reconstruction and Energy Calibration of Calorimeter Jets

Quarks and gluons cannot be directly measured. Instead, they initiate parton showers which hadronise due to the colour confinement into showers of colour-neutral secondary particles. These shower particles finally interact with the detector material and generate a signal related to the initially scattered parton.

In general, the individual identification of these shower particles is not necessary to describe the four-vector of the initial parton. Instead, the entire particle shower is grouped together and treated as one physics object. This so-called **Jet** represents the initiated particle shower, and thus the causative parton, by one single four vector object. In addition, a jet is defined being an expanded object with three-dimensional shape and an inner structure. In order to describe those, so-called jet shape variables can be defined.

As illustrated in Figure 3.1, a jet is a generic object and can represent a particle shower at several levels, depending on its constituents. It can be reconstructed from Monte Carlo generated partons (**Parton Jets**), from shower particles after hadronisation (**Particle Jets**), from energy deposits of these particles in the calorimeter system (**Calorimeter Jets**) and even from tracks of charged particles in the inner detector system (**Track Jets**). In order to reconstruct a collection of jets from a collection of constituents, generic jet reconstruction algorithms are defined.

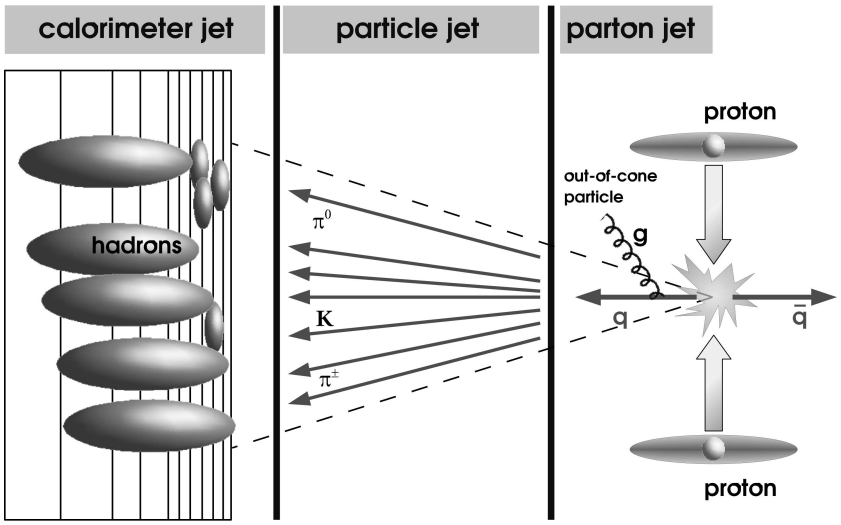

Figure 3.1.: Sketch of the different reference levels of jets, depending on their constituents.

The following chapter is focusing on the situation within the ATLAS experiment, where calorimeter jets are used for early data analyses like QCD studies or top quark mass measurements. One important issue concerning calorimeter jets is the precise determination of their energy. In order to keep the systematic uncertainties on the absolute **Jet Energy Scale** (JES) and **Resolution** small, a good energy calibration of all calorimeter objects, from the cell up to the jet level, is required. Only this allows finally for precision measurements of hadronic final states with the ATLAS detector.

3.1. Jet Reconstruction Algorithms

The reconstruction of jets from a collection of physics objects (like Monte Carlo generated particles or calorimeter cells) is performed using generic jet finder algorithms. All of these jet reconstruction algorithms have in common to group subsets of jet input objects and recombine their four-vectors to final jet objects. Thus a collection of jets can be well defined by its constituents type and the reconstruction algorithm applied. In order to achieve a good correspondence between the reconstructed jet and the initiating parton, several quality requirements have been defined. These are important to retrieve a stable definition in a multi-particle final state environment. It is necessary to ensure [50, 40]:

- **Infrared Safety**, which means that the presence or absence of additional soft particles beyond the fragmentation should not affect the number nor the kinematics of jets in the final state.

- **Collinear Safety**, which means that the jet reconstruction should be independent of the fact that a certain amount of transverse momentum is carried by one particle, or if this particle is split into two collinear particles.

- **Order Independence**, which means that the same hard scattering process should be reconstructed independent of the physics level (e.g. particles from Monte Carlo simulation or calorimeter cells).

- **Detector Technology Independence**, which means independence of the specific signal characteristics including detector inefficiencies.

- **Environment Independence**, which means that the jet reconstruction result should be independent of the luminosity and thus the number of multiple interactions.

Within the ATLAS analysis framework `Athena` [51], two different types of jet reconstruction algorithms are implemented. The first uses a fixed cone size to collect the jet constituents while the other sequentially recombines their four-vectors. Both types are implemented to accept any type of four-vector based input collection, thus MC generated as well as detector level objects.

3.1.1. Fixed Cone Size Algorithms

The standard fixed cone size algorithm within the ATLAS framework is implemented as an iterative and seeded algorithm. This means that all input objects within a fixed cone size around a preassigned seed object are combined to so-called proto-jets. In case of shared constituents between the proto-jets, dedicated split and merge procedures are defined. In more detail, the algorithm runs through the following steps:

1) In a first step, any input collection is ordered by transverse momentum p_T.

2) Starting with the highest p_T-object exceeding the threshold p_T^{seed}, all input objects within a cone of $\Delta R < R^{cone}$ are combined with the seed object. Typical values for the fixed cone radius R^{cone} are in the range from 0.4 to 0.7.

3) The combined four-vector of the proto-jet constituents defines a new direction and the ΔR-scan is repeated until the proto-jet axis is stable. It can happen, that an input object of the first iteration doesn't belong to the final jet after updating the cone direction.

4) Restart of the procedure with the next seed object in the p_T-ordered input collection until no input object exceeding p_T^{seed} is left.

Since the input objects collected by one jet are not excluded from the input collection, it is possible to share constituents between two different jets. Furthermore, the jet finding might loose input objects with low transverse momenta during the iteration due to the updated direction. Thus the ATLAS Cone algorithm is not infrared safe. In addition, possible seed objects can be left unconsidered if the input object is split, hence collinear safety is not ensured. Both effects can be partly resolved applying split and merge procedures. In case of shared constituents, jets are either merged or split depending on the energy fraction of the shared constituents with respect to the less energetic jet.

A more sophisticated solution is the Seedless Infrared Safe Cone (SISCone) [52] jet algorithm. Instead of using a seed object, all possible stable cones are searched in the input collection before applying as well split and merge procedures. This reduces the bias from the seed object and should recover infrared and collinear safety.

3.1.2. Sequential Recombination Algorithms

As an alternative approach for jet reconstruction, sequential recombination algorithms [53, 54] have been implemented within the ATLAS framework. Here, input objects are combined to

proto-jets with respect to their distance in a specific four-vector metric. This distance d_{ij} of two input objects is defined as:

$$d_{ij} = \min\left(k_i^{2p}, k_j^{2p}\right)\frac{\Delta R_{ij}^2}{R^2}, \tag{3.1}$$

where ΔR_{ij} is their distance in the η-ϕ space as defined in Eqn. 2.2 and R is the distance cut-off parameter which is typically chosen within a range of 0.4 to 1.0. In addition, the distance d_i^{beam} of each input object to the beam axis is defined as:

$$d_i^{beam} = k_i^{2p} \tag{3.2}$$

The variable k is related to the energy of the input object and is chosen to be either E, E_T, E_T^2, p_T or p_T^2, depending on the recombination schema. The parameter p is set to $p = 1$ in case of the **kt algorithm** and to $p = -1$ in case of the **anti-kt algorithm** [55]. The actual algorithm starts with the calculation of all distances d_{ij} and d_i^{beam} plus the determination of the minimal distance $d_{min} = \min\left(d_{ij}, d_i^{beam}\right)$ in the event.

In the **inclusive mode**, one distinguishes between two cases:

1) If d_{min} is of the type d_{ij}, the two input objects i and j are combined and replaced by the new object in the input list.

2) If d_{min} is of the type d_i^{beam}, the object i is classified as jet and removed from the input list.

The calculation of all distances and the determination of d_{min} is repeated until no input object is left. This means that all input objects are either combined to jets or classified itself as jets.

The **exclusive mode** is usually chosen to select specific event topologies. In principal it follows the routine of the inclusive mode, but stops if d_{min} exceed a given cut-off value d_{cut}. All remaining input objects are classified as jets.

1) If d_{min} is of the type d_{ij}, the two input objects i and j are combined and replaced by the new object in the input list as in the inclusive mode.

2) But if d_{min} is now of the type d_i^{beam}, the object i is interpreted as originated from the beam remnant and thus is rejected.

This iterative process continues until the end of the input object collection is reached. A modification of the exclusive mode allows further to predefined the maximum number of jets instead of the $\mathrm{d_{cut}}$-value.

Sequential recombination algorithms don't allow for shared constituents between two jets. Furthermore, the definition of seed objects is not needed. As a consequence, these jet reconstruction algorithms fulfil the requirements of infra-red and collinear safety, which can be even theoretically proved. One inconvenience are the irregular shapes of the jets, in particular from the kt-algorithm. It can be explain, that in the case of $p = 1$, the distances d_{ij} between soft objects are small and they therefore dominate the clustering. This has been solved with the anti-kt algorithm, where the clustering is dominated by the hard objects which leads to cone-like shapes of the resulting jets.

3.2. Truth Particle Jets

Most of the shower particles cannot directly be identified from the detector signal. Thus particle jets can be only built in simulated events. They are reconstructed using the four-vectors from stable particles produced by the fragmentation model of the Monte Carlo generator.

Within the ATLAS framework, the definition of stable particles includes all particles with a lifetime of more than 10 ps. They are collected in a so-called TruthParticleContainer and serve as input for the jet reconstruction algorithms. Since neutrinos are not measurable with the ATLAS detector and muons are only minimal ionising in the calorimeter system, they are excluded from the jet making.

As a result one obtains a collection of particle jets, also referred to as **Truth Particle Jets**. Those represent the "truth" reference for many jet performance studies and are also used in simulation based jet energy calibration approaches (particle jet level).

3.3. Calorimeter Jets

Reaching the calorimeter system and interacting with the detector material, the shower particles initiate secondary particle showers and deposit their energy. The generated signal of the calorimeter cells is readout and a four-vector can be defined for each of them. In principal, these calorimeter cells can serve as a direct input to the jet algorithms. In practise, it is advantageous to combine these calorimeter cells into larger calorimeter signal objects in order to minimise the number of input four-vectors and to separate noisy cells.

Within the ATLAS framework, two different concepts to reconstruct those higher level calorimeter objects are available: **Projective Signal Towers** and **Topological Cell Clusters**. In contrast to the cell four-vectors, the four-momenta of these towers and clusters are physically meaningful and show a better correspondence to the initial shower particles.

3.3.1. Projective Signal Towers

Projective Signal Towers are reconstructed by projecting calorimeter cells onto a fixed grid in the η-ϕ space. In the whole acceptance region of the calorimeter system, the tower bin size is $\Delta\eta \times \Delta\phi = 0.1 \times 0.1$ which results into 6,400 towers per event. While projective calorimeter cells fully contribute to the tower signal, non-projective cells or cells larger than the grid size contribute only fractional, depending on the overlap area with the towers. This contribution is expressed by a geometrical weight which is calculated from the ratio of the tower bin area over the projective cell area in the η-ϕ space. All calorimeter cells are finally included into the collection of towers and the tower signal is defined as the non-discriminatory sum of possible weighted cell signals.

The inclusion of all calorimeter cells leads to the problem, that even cells with pure electronics noise contribute to the towers. In order to at least partly resolve this problem, noise suppression procedures help to reject towers which only consist of noisy calorimeter cells. Nevertheless, the noise contribution within towers including real signal is still high.

3.3.2. Topological Cell Clusters

In order to improve the noise suppression of the calorimeter signal as well as the correspondence of calorimeter objects to particles, the concept of **Topological Cell Clusters** (**Topo-Clusters**) [56] has been developed. In contrast to the fixed size tower concept, the calorimeter cells are dynamically grouped around preselected seed cells based on predefined noise thresholds. Afterwards, dedicated split procedures are applied in order to consider local energy maxima.

In practise, the algorithm consists of the following individual steps, exemplary illustrated in Figure 3.2:

1) First, the algorithm searches for seed cells, which exceed the expected total noise fluctuations by a factor of 4 in $|E_{cell}|$.

2) Then, neighbouring cells in all three dimensions are attached to the seed cells if they exceed the expected noise fluctuation by $|E_{cell}|/\sigma_{noise} > 2$. This process is iterated until no 2σ-cells can be attached any more. Finally, two proto-clusters are merged, if they share at least one neighbour cell.

3) Finally, all perimeter cells of the proto-clusters are attached if they pass a third noise threshold. In the default case, where the threshold is $|E_{cell}|/\sigma_{noise} > 0$, all perimeter cells are attached.

4) In a last step, large clusters are split, if at least two local maxima are found. Here, local maxima are defined as cells exceeding a fixed energy threshold of $E_{cell} > 500\,\text{MeV}$, with at least 4 neighbouring cells and no neighbour with higher energy. The cells of the proto-cluster are then regrouped around these local maxima without any noise thresholds.

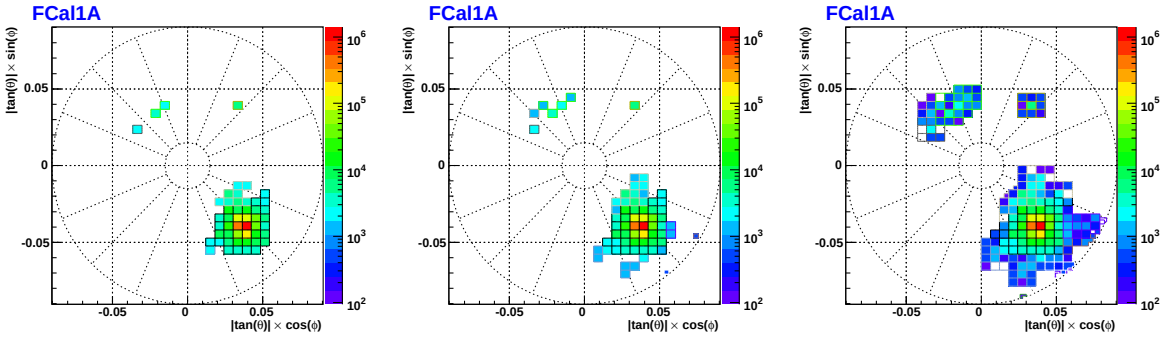

Figure 3.2.: Exemplary illustration of the topological cell clustering algorithm, shown in the x-y plane of the first FCAL layer. After searching for seed cells with $|E_{cell}|/\sigma_{noise} > 4$ (left), all neighbour cells with $|E_{cell}|/\sigma_{noise} > 2$ are attached to the seed cells. (centre) Finally, all perimeter cells with $|E_{cell}|/\sigma_{noise} > 0$ are attached as well, before dedicated split algorithms are applied. (right)

The result of the topological cell clustering process is a collection of topological cell clusters (`CaloTopoClusters`). In general, the noise thresholds can be individually chosen, depending on the analyses purpose. Nevertheless, it has been shown in the past [56], that the default choice of $|E_{cell}|/\sigma_{noise} > 4/2/0$ results into the best description of a particle shower by a TopoCluster. Due to the dynamic growing, a better correspondence between individual clusters and stables particles has been obtained [40].

3.4. Energy Calibration of Calorimeter Jets

The ATLAS calorimeter system is the main device to measure the energy of the shower particles. Thus, the precise energy calibration of calorimeter jets is a fundamental point in order to provide meaningful jet four-vectors, mirroring the initiated particle showers or even the initial partons. Furthermore, the magnitude of the jet energy resolution and thus the systematic uncertainty of the jet energy scale plays an important role in precision measurements from hadronic final states.

The energy of the calorimeter cells is initially provided at the so-called **Electromagnetic Scale** (**EM Scale**), which is obtained by applying dedicated calibration factors, derived from test beam measurements with electron beams. The total energy of a calorimeter jet reconstructed from these cells shows a significant difference from the expected energy of a matched truth particle jet, unless the jet consists of γ, e and π^0 only.

The reason are several detector related effects, which can be summarised as follows:

a) The non-compensating character of all ATLAS calorimeters leads to a reduced response of hadronic showers with respect to electromagnetic showers.

b) On their way to the calorimeters, the particles pass the inner detector material as well as readout cables and the cryostat wall. Thereby, they already loose energy or can be even stopped completely in the material.

c) Another important point is the deflection of low energetic particles in the magnetic field of the solenoid. In principal, particles can be bent that far, that cluster or jet algorithms allocate them wrongly.

In order to compensate these energy losses, dedicated energy calibration concepts have been developed. In general, the calibration process is subdivided into three different levels:

1) At **Calorimeter Level**, a hadronic calibration of the calorimeter objects (cells, towers, clusters) is applied, mainly to restore the energy response of the non-compensating calorimeters to hadronic showers.

2) Residual detector effects are then treated at **Jet Level** in order to calibrate the calorimeter jet with respect to the expected energy of a matched truth particle jet (**Particle Level**).

3) Finally, data driven in-situ calibration approaches are applied in order to set the absolute jet energy scale as close as possible to the scale of the initial parton (**Parton Level**), independent from Monte Carlo simulation.

In the following paragraphs, these three calibration levels are described in more detail. At the end of this chapter, a summary of the most important jet calibration sequences within the ATLAS framework is provided and illustrated in the overview schema in Figure 3.6.

3.4.1. Hadronic Calibration of the Calorimeter Objects

In contrast to electromagnetic showers, which consist of short and narrow e^+e^--$\gamma\gamma$-cascades, hadronic showers are much longer and have a more complex substructure. As illustrated in Figure 3.3, a hadronic shower can be subdivided into four different energy components. The **electromagnetic** component ($\sim 50\,\%$) from electromagnetic sub-showers is mainly initiated by neutral pions while the **non-electromagnetic** component ($\sim 25\,\%$) is dominated by hadronic cascades of charged pions. Furthermore, there is an **invisible** component ($\sim 23\,\%$) from nuclear split-offs mainly from neutrons and an **escaped** energy component ($\sim 2\,\%$) from particles like neutrinos, not leaving any signal in the calorimeter system.

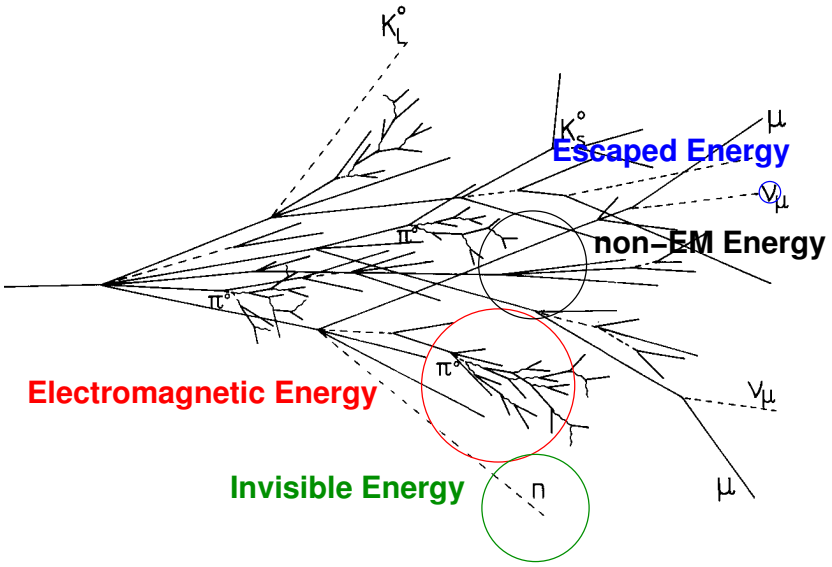

Figure 3.3.: Illustration of the hadronic shower profile indicating the electromagnetic (red), non-electromagnetic (black), invisible (green) and escaped energy components (blue).

As described in Chapter 2, the ATLAS calorimeters are all non-compensating, which means that the energy response to hadrons is lower than the response to electrons and photons. This has to be corrected through the hadronic calibration of the calorimeter signal. In order to distinguish between electromagnetic and non-electromagnetic components, a characteristic feature of the calorimeter system is used. Using absorber material with large proton numbers Z, the electromagnetic radiation length (X_0) is much smaller than the hadronic interaction length (λ_I) and thus electromagnetic showers are shorter, more narrow and create a larger cell energy density than hadronic showers.

Both major hadronic calibration concepts in ATLAS, the Global Cell Weighting and the Local Hadron Calibration are taking this into account. Based on simulated events, cell weights are applied in order to correct for the non-compensating character of the calorimeters. Furthermore, several detector effects are already treated at this level, but in a conceptional opposite way.

Global Cell Weighting

The goal of the **Global Cell Weighting** (**GCW**) approach is to apply dedicated hadronic weights to the cells of a calorimeter jet in order to correct the non-compensating character of the calorimeter technology. They are derived from a comparison of reconstructed calorimeter jets with truth particle jets, both in simulated events. As input to the calorimeter jet reconstruction either signal towers or topological clusters at electromagnetic energy scale are used. The energy of the calorimeter jet is therewith defined as the sum of all contributing cell energies.

In order to derive the hadronic cell weights, pairs of matched calorimeter and truth particle jets are selected in simulated QCD dijet events. Here, the Monte Carlo generator `Pythia` [57] has been used in combination with a `Geant4` [58] detector simulation. The calorimeter jet is matched to a truth particle jet if their jet axes overlap within a cone of $\Delta R < 0.2/3$. Considering only the jet pair with the highest transverse momentum per event, the following quantity is minimised using the dedicated software package `MINUIT` from the CERN program library [59]:

$$\chi^2 = \sum_{e=events} \left(\frac{E_{reco}^{(e)} - E_{true}^{(e)}}{E_{true}^{(e)}} \right)^2 . \tag{3.3}$$

The summation is done over a large set of events, where in each event $E_{reco}^{(e)}$ is the energy of the weighted four-vector of the reconstructed calorimeter jet and $E_{true}^{(e)}$ is the energy of the matched truth particle jet. Considering, that the reconstructed calorimeter jet consists of a set of cells with the energy E_i and the energy density ρ_i dependent cell weight w_i, the reconstructed cell energy E_{reco} is defined as:

$$E_{reco} = \sum_{i=cells} w_i \left(\rho_i\right) E_i. \tag{3.4}$$

Due to the large number of calorimeter cells and thus the large number of possible cell weights, the number of parameters to be computed needs to be reduced for performance reasons. Taking into account similar characteristics of cells in the same detector region and modelling a correlation between different cells, the number of free fit parameters is significantly reduced to 45.

The result of the minimisation is a set of hadronic cell weights depending only on the cell energy density $\rho = E_{cell}/V_{cell}$. They are applied to the cells of the calorimeter jet after reconstruction and improve the jet energy response significantly. Since the cell weights are derived from a jet comparison, a systematic dependence from the jet reconstruction algorithm used is expected. And even if the global cell weighting approach already includes several detector effect, there are still non-linearities of the jet energy response which can not be compensated at this level. For this reason, a dedicated correction at the final jet level has to be applied.

Local Hadron Calibration (LCW)

The aim of the **Local Hadron Calibration** (**LCW**) is to provide a meaningful energy calibration for topological cell clusters. In contrast to the GCW approach, the LCW concept doesn't require any jet reconstruction and thus their weights are independent of the actual jet reconstruction algorithm.

One key point of the LCW approach is to treat different detector related effects as individual as possible. Thus the calibration schema uses topological clusters at electromagnetic scale and accounts for the following three types of energy losses:

1) the lower energy response of hadronic showers,

2) energy losses outside of the clusters due to the reconstruction noise thresholds

3) and energy losses outside the active calorimeter material.

In order to define a reference energy for calorimeter cells, the concept of **Calibration Hits** is exploited. Using the detector simulation framework `GEANT4`, the energy fraction of the four hadronic shower components (em, non-em, invisible and escaped) is calculated for each calorimeter cell. From those, a true cell energy E_{cell}^{true} is defined and used to derive dedicated calibration weights.

The calculation of local hadron calibration weights is done using Monte Carlo events, where the energy response of single pions is simulated using `GEANT4`. The advantage is, that the entire calorimeter signal corresponds to a single particle with a well defined energy.

The calibration sequence starts with a **Classification** of the topological clusters at electromagnetic scale. Based on its properties it is decided if a cluster stems mainly from an electromagnetic or an hadronic type of shower. The phase-space exploit consists of the cluster energy E_{cl}, its pseudo-rapidity $|\eta_{cl}|$, the cluster depth in the calorimeter λ_{cl} and its energy density ρ_{cl}. If the probability of finding a neutral pion in the respective phase-space bin exceeds 0.5, the cluster is classified as electromagnetic, otherwise as hadronic. Each of the following correction steps takes this decision into account, applying interpolated weight depending on the em-probability found.

In a first correction step, each cell within clusters being classified as hadronic receive a **Hadronic Weight** (**W**) in order to recover the lower response of the hadronic showers in the non-compensating ATLAS calorimeters. These weights are derived inverting the average ratio of the reconstructed cell energy E_{cell}^{reco} over the true cell energy E_{cell}^{true} from the calibration hits. The phase-space is defined by E_{cl}, $|\eta_{cl}|$, the sampling layer of the respective cell and its energy density ρ_{cell}. The result are clusters with corrected cell energies, but in order to fully restore the energy of the initial particle, additional corrections need to be applied.

One reason stems from the topological cluster reconstruction algorithm itself. Due to the noise thresholds it can happen, that energy deposits inside the calorimeter are not included into any cluster. These energy losses are recovered by the **Out-Of-Cluster Corrections** (**OOC**). In order to derive dedicated weights, the calibration hit energy of all cells outside of any cluster are associated to clusters within a wide cone radius. Here, sharing of cells between multiple clusters is allowed. The derived weights are applied depending on E_{cl}, $|\eta_{cl}|$, λ_{cl} and the cluster isolation.

The second kind of correction are developed to recover the energy losses in the upstream material, the calorimeter crack regions, the cryostat walls and even the leakage energy. These so-called **Dead Material Corrections** (**DM**) are calculated using a special type of `GEANT4` calibration hits outside of the instrumented regions of the calorimeters. A correlation of these energy losses to cluster properties is very complex, in particular in cases of large correction factors. The variables used in the phase-space are E_{cl}, $|\eta_{cl}|$, λ_{cl} and the sampling layer of the cluster.

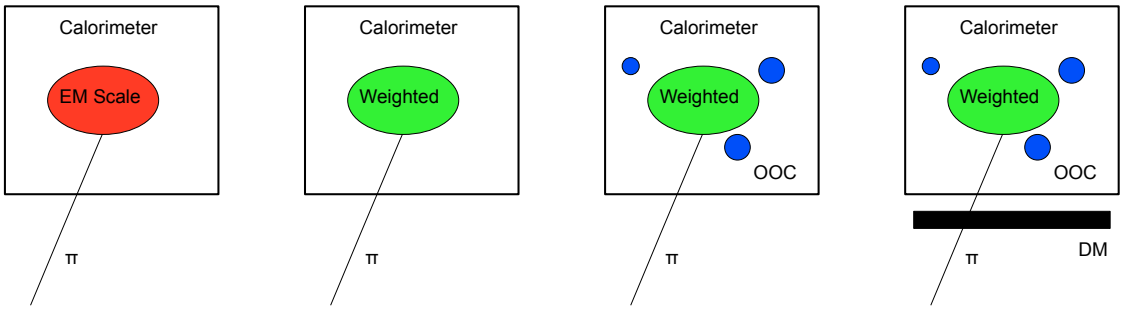

Figure 3.4.: Sketch of the various contributions to Local Hadron Calibration. It starts with TopoClusters at em-scale (red), which receive hadronic weights in order to recover the hadronic energy (green). Finally, dedicated corrections for out-of-cluster (blue) and dead material energy (black) are applied.

An important feature of the approach is, that apart from the classification all correction steps are independent of each other, thus they can be updated individually. The performance of the local hadron calibration on events from single pion simulations is shown in Figure 3.5. The sequential improvement of the energy response linearity for each of the three cluster correction steps leads to a final deviation within $\pm 2\,\%$ for a wide range of pion energies. Furthermore, the energy response resolution could be improved as well with each calibration step.

The result of the local hadron calibration is a set of calibrated clusters (`CaloCalTopoCluster`) which can be used as input objects to the jet reconstruction algorithms. It is expected, that the result of the jet making slightly changes with respect to the reconstruction from clusters at electromagnetic scale.

3.4.2. Monte Carlo based Jet Level Corrections

Any correction on cell or cluster level cannot compensate for so-called out-of-cone effects from the jet reconstruction. Those can be the deflection of low energetic particles in the solenoid field or particles which never reach the active calorimeter material due to energy losses in the upstream material. These effects lead to residual non-linearities of the jet energy response even after hadronic calibration of the constituents.

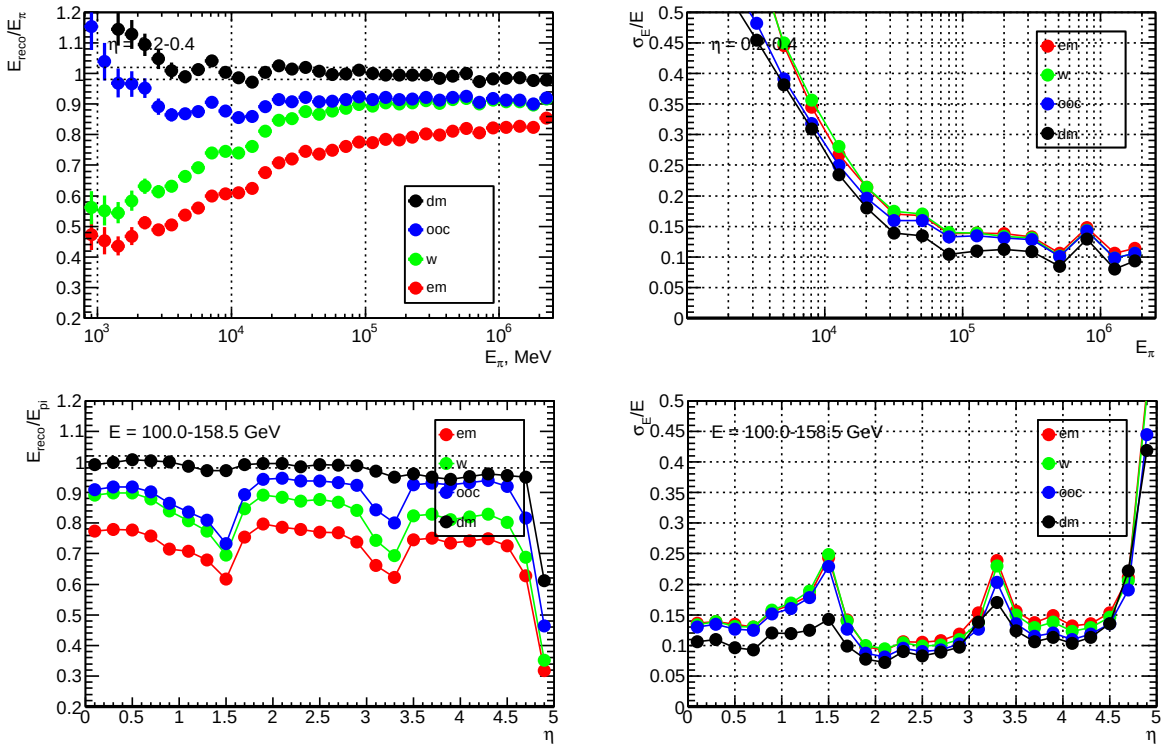

Figure 3.5.: Linearity (left) and resolution (right) of the energy response as function of the pion energy (top) and the calorimeter region (bottom) for simulated single pion events after each step of the local hadron calibration. The electromagnetic scale (red), after hadronic weighting (green), after out-of-cluster corrections (blue) and after dead material corrections (black) [40]. The major contribution comes from dead material and out-of-cluster corrections, in particular at low energetic and in the crack regions of the calorimeter system. At higher energies, the cells weights are dominating.

These detector related effects are recovered applying dedicated **Jet Level Corrections** derived from a comparison to the energy of truth particle jets. Thus the calibration is done with respect to the particle level. The common approach within theATLAS framework is to calculate weights through the inversion of the a set of response functions $R\left(p_{T,jet}^{true}\right)$:

$$R\left(p_{T,jet}^{true}\right) = \left\langle p_{T,jet}^{reco} / p_{T,jet}^{true} \right\rangle \tag{3.5}$$

evaluated in bins of the pseudo-rapidity η_{jet}^{true} and $p_{T,jet}^{true}$. Here, $p_{T,jet}^{reco}$ is the transverse momentum of the jet at the energy scale of its constituents (EM, GCW or LCW) and $p_{T,jet}^{true}$ is the transverse momentum of the matched truth particle jet within a cone of $\Delta R < 0.3$ around the jet axis. Typically, events from simulated QCD dijet samples are used in order to calculate the response function.

The so-called **Numerical Inversion** method is now used to estimate the response function $R\left(p_{T,jet}^{reco,est}\right)$ through inversion of $R\left(p_{T,jet}^{true}\right)$ in bins of $p_{T,jet}^{reco,est}$ and replacing η_{jet}^{true} by η_{jet}^{reco}:

$$R\left(p_{T,jet}^{reco,est} = R\left(p_{T,jet}^{true}\right) \times p_{T,jet}^{true}\right) = R\left(p_{T,jet}^{true}\right)^{-1}. \tag{3.6}$$

The result of Equation 3.6 is finally used to calibrate the reconstructed calorimeter jets to particle level. As a consequence, the jet response linearity is restored within $\pm 2\,\%$ over a wide range of jet transverse momenta and pseudo-rapidities.

In order to improve the performance of these jet level corrections, several different concepts have been recently developed. In particular to improve the jet energy resolution, additional information from inner detector tracks or jet shape variables from the calorimeter system are taken into account. One of those approaches has been developed during this thesis and is described in detail in Chapter 4.

3.4.3. Data Driven in-situ Jet Calibration

The result of the jet reconstruction and energy calibration within the ATLAS framework are `JetCollections` calibrated to the truth particle level and thus representing the particle shower. In order to set the jet four-vector to the energy scale of the initial parton, a final calibration step needs to be applied.

This in-situ correction depends in general very much on the analysis scope since the origin of the jet (hard quarks or gluons, soft radiation) matters at this scale. Furthermore, a direct association of the four-vectors of coloured partons with colour-neutral shower particles is theoretical extremely disputable, since the colour-flow would be neglected. Therefore, it is preferred to take the energy of well defined colour-neutral bosons in order to define a reference energy scale.

The first approach requires a transverse momentum balance between particles at electromagnetic scale and the hadronic recoil from jets. This is commonly used in γ+jets or Z+jets events, where the Z-boson decays in electrons.

A second approach uses average values of previous measurements in order to set a reference scale. In particular in top quark pair events, the W-boson reconstructed from jets is compared to the known mass [2] of the W-boson.

3.5. Calorimeter Jet Sequences in ATLAS

In the following the major jet reconstruction and calibration sequences within the ATLAS framework are briefly described. As shown in Figure 3.6, each of them starts with calorimeter cells at electromagnetic energy scale and ends with calibrated calorimeter jets.

Sequence I, starts with the reconstruction of signal towers which are taken as input to the jet reconstruction algorithm after applying a noise suppression procedure. The global cell weighting approach is used for the hadronic calibration before jet level corrections are applied. The final step is an analysis dependent in-situ calibration.

Sequence II, is very similar to sequence I, but here topological cell clusters are used instead of signal towers. The advantage is the automatic noise suppression and cluster-particle correspondence as a consequence of the cluster algorithm. After jet finding, sequence II follows exactly sequence I.

Sequence III, is using topological clusters as well, but they are calibrated using the local hadron calibration approach before the jet finding. Thus the result of the jet making are jets already calibrated to the hadronic scale. Finally, dedicated jet level corrections are applied before an analysis depended in-situ calibration.

In order to simplify the jet energy calibration sequence for early data analyses, a reduced calibration sequences can be applied as well. Here, one abstains from pre-calibration of the calorimeter objects and directly scales the jet energy from electromagnetic scale to truth particle level.

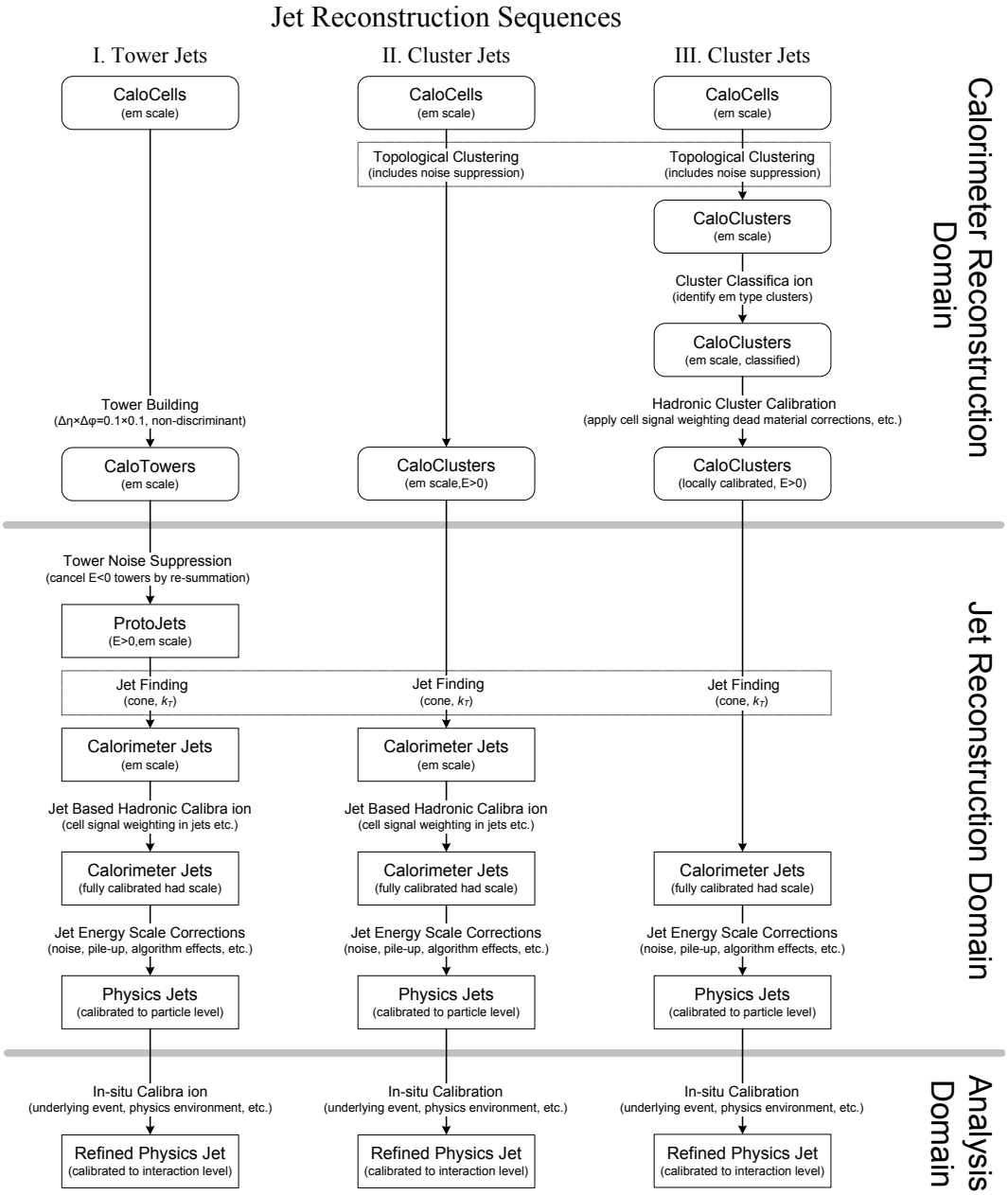

Figure 3.6.: Schematic view on the reconstruction sequences for jets from calorimeter towers (left), uncalibrated (centre) and calibrated (right) topological calorimeter cell clusters in ATLAS. The reconstruction (software) domains are also indicated. [40]

4. Jet Energy Calibration using Jet Shape Information

In the previous chapter, the process of jet energy calibration within the ATLAS analysis framework, from calorimeter cell weighting to data driven in-situ calibration methods, are described. Since data driven in-situ methods are very specific to the analysis performed, collections of jets, calibrated with respect to the Monte Carlo truth particle level, are generally used instead as a common basis for most of the physics analyses.

In order to restore the energy of the truth particle level, pre-calibration methods for the constituents of the jets, for example Local Hadron Calibration for topological cell clusters, show already very good results [40, 60]. Nevertheless, a full compensation for all energy losses is hardly achievable with calibration methods on cell or cluster level only. In particular two effects:

1. the stopping of low energetic particles in the non-instrumented upstream material

2. and the deflection of low energetic charged particles in the magnetic field

are not recoverable at constituent level. Those particles don't leave any signal in the considered calorimeter region and thus it is not possible to correlate their energy to individual clusters which are initiated by completely different particles. Instead, both effects need to be corrected at jet level through the application of dedicated calibration weight factors to the jet four-vector, exploiting correlations of these particles with the jet composition.

One way to derive a set of calibration weights is the comparison of calorimeter jets with their corresponding truth particle jets in Monte Carlo simulated events. The current approach within the ATLAS analysis framework, described in Section 3.4.2, uses a set of calibration weights, depending on the jet four-vector properties transverse momentum p_T and pseudo-rapidity η.

However, the ATLAS calorimeter system with its high cell granularity offers a more detailed description of a jet object than only its four-vector properties. It is possible to define meaningful jet shape variables in order to derive information on the sub-structure of a jet, especially on its energy distribution inside.

If one of those jet shape variables shows a strong correlation to the amount of missing jet energy, it can be considered to extend the phase space for the calculation of a more refined set of jet energy calibration weights.

In the following sections, the development of this new jet energy calibration method is described. The jet energy response of `LCTopoJets` is studied and several jet shape variables are defined and tested with respect to their ability to enlarge the phase space for the calculation of calibration weights.

One of those jet shape variables, the fraction of transverse energy hold by low energetic clusters, is taken to calculate a new set of jet energy calibration weights. The jet energy response of the re-weighted jet collection is finally tested for linearity and resolution improvement as well as for stability in different physics channels.

The software to calculate and to apply the calibration weights to a collection of jets has been implemented into the ATLAS analysis framework and is available to the whole collaboration.

4.1. Jet Energy Response

The most important key figure to determinate the precision of the jet energy calibration is the jet energy response R_{jet} with respect to Monte Carlo truth particle jets. It is defined as the ratio of the energies of a reconstructed calorimeter jet (E_{jet}^{reco}) to a corresponding truth particle jet (E_{jet}^{true}) from the same Monte Carlo event

$$R_{jet} = E_{jet}^{reco} / E_{jet}^{true}. \tag{4.1}$$

In order to identify corresponding pairs of reconstructed and truth particle jets, a matching criteria has to be defined. In the following, a geometrical criteria, using the spatial distance ΔR from Eqn. 2.2, is chosen. More precisely, a truth particle jet matches a reconstructed jet if it is the closest in ΔR and is within a predefined cut-off distance

$$\Delta R < \Delta R_{cut}. \tag{4.2}$$

The distribution of the jet energy response R_{jet} shows usually a peak but is not necessarily Gaussian. Since the shape of the jet energy response distribution varies with the phase space position, robust and shape independent estimators are chosen to quantify the result. The average jet energy response $\langle R_{jet} \rangle$ is given by the arithmetic mean

$$\langle R_{jet} \rangle = \frac{1}{N_{jet}} \sum_{j=1}^{N_{jet}} R_{jet}^{j} \tag{4.3}$$

and the spread is represented by the root mean square

$$\sigma_{R_{jet}} = \sqrt{\frac{1}{N_{jet}} \sum_{j=1}^{N_{jet}} \left(R_{jet}^{j} - \langle R_{jet} \rangle \right)^2}. \tag{4.4}$$

Since the absolute value of the root mean square scales with energy of the jets it is common to examine the relative error, the jet energy resolution

$$\Delta_{R_{jet}} = \sigma_{R_{jet}} / \langle R_{jet} \rangle . \tag{4.5}$$

The jet energy response has a direct impact on the systematic uncertainty and thus on the precision of measurements with hadronic final states involved. In order to minimise this impact it is important to achieve an average jet energy response close to $\langle R_{jet} \rangle = 1$, stable and linear over all detector regions and a wide range of jet energies. It is further important to keep the resolution as small as possible in order to minimise statistical fluctuations of the jet energy scale.

4.2. Jet Energy Response of LCTopoJets

The basis of the following studies are `AntiKt4LCTopoJets` which are calorimeter jets reconstructed from topological cell clusters (`TopoCluster`) after pre-calibration with Local Hadron Calibration (`LC`). The reference is a collection of `AntiKt4TruthJets` using a tight matching criteria of $\Delta R < 0.1$. Both collections of jets are reconstructed using the anti-kt jet algorithm with a distance parameter of $d = 0.4$ and an intrinsic transverse energy cut of $E_T^{jet} > 7\,\text{GeV}$.

Since the energy of the matched calorimeter jets fluctuate around the energy of the reference jet, a symmetric cut for both jet collections would bias the response studies. In order to also allow down fluctuations of the energy response with respect to the reference jet, an additional transverse energy cut of $E_T^{true} > 20\,\text{GeV}$ has been set for the truth particle jets.

The sample of jets to be analysed is taken from Monte Carlo QCD events of a generated $2 \to 2$ process (dijet). The events are generated with the `Pythia` event generator plus `Geant4` detector simulation. The final set of events is a combination of the so-called `J0` to `J7` samples which are subdivided with respect to the generated transverse momentum of the hard scattering process (cf. Appendix A.1). For each of the `JX` samples about $1 \cdot 10^5$ events were considered.

The distribution of the average jet energy response of `AntiKt4LCTopoJets` is shown in Figure 4.1. On the left side, the $\phi_{\text{jet}}^{\text{true}} - \text{E}_{\text{jet}}^{\text{true}}$ plane, the general trend shows a rising energy response towards larger jet energies from about $\langle R_{jet} \rangle \sim 0.8$ for $E_{jet}^{true} = 20\,\text{GeV}$ up to $\langle R_{jet} \rangle \sim 0.9$ for $E_{jet}^{true} = 1\,\text{TeV}$. In contrast, the energy response is constant within a ϕ-region.

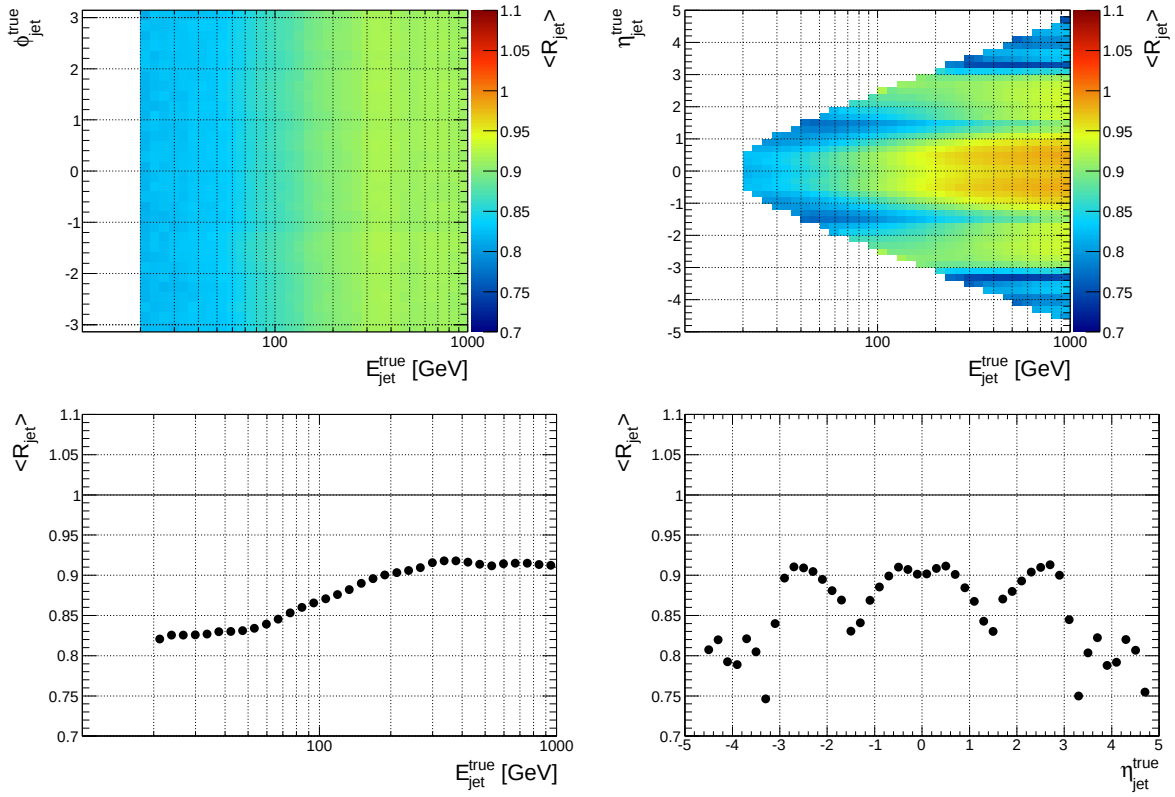

Figure 4.1.: Average jet energy response $\langle R_{jet} \rangle$ of `AntiKt4LCTopoJets` with respect to `AntiKt4TruthJets`. The upper row shows the $\phi_{\text{jet}}^{\text{true}} - \text{E}_{\text{jet}}^{\text{true}}$ (left) and $\eta_{\text{jet}}^{\text{true}} - \text{E}_{\text{jet}}^{\text{true}}$ plane (right), while the projections to the E_{jet}^{true}- (left) and η_{jet}^{true}-axis can be found in the lower row. The colour code indicates areas with a lower response in blue, changing over green and yellow to red for areas with higher jet energy response. While the average jet energy response is linear in ϕ, it fluctuates depending on the jet energy and the η-position.

The picture changes in the $\eta_{\text{jet}}^{\text{true}} - \text{E}_{\text{jet}}^{\text{true}}$ plane on the right side of Figure 4.1. In addition to the rising behaviour towards higher energies, a significant dependence on the η-position is observed. The more central the region, the closer to $\langle R_{jet} \rangle = 1$ is the energy response. Especially in the non-instrumented gap regions between the calorimeter subsystems around $\eta \sim 1.4$ and $\eta \sim 3.2$, the energy response drops down compared to other η-regions with the same jet energies. The population of the $\eta_{\text{jet}}^{\text{true}} - \text{E}_{\text{jet}}^{\text{true}}$ phase space is constrained by the transverse momentum cut of $E_T^{true} > 20\,\text{GeV}$ for the truth particle jets which correlates the energy and η-position of the jets.

4.3. Jet Shape Variables and Jet Energy Response Sensitivity

Due to the high granularity of the ATLAS calorimeter system, calorimeter jets can be described as combined objects of their constituents, e.g. cells or clusters. Thus a calorimeter jet is not any longer represented by a four-vector only, it is further possible to define jet shape variables, giving important information on the substructure of a jet and how energy is distributed inside.

The following studies exemplarily analyse some of the possible jet shape variables. In addition to the definition and distribution of those variables, the focus is set on the sensitivity to the non-linearity of the jet energy response distribution. A high sensitivity makes the variable a good candidate to extend the phase space for the calculation of a new set of jet energy calibration weights.

4.3.1. Jet Width

Since calorimeter jets in ATLAS are more-dimensional objects it is possible to measure the width of the jet. Here, the jet width is defined as the p_T-weighted sum of the constituent clusters distances ΔR with respect to the jet axis and describes how collimated the initiating hadron shower is

$$\text{jet width} = \frac{1}{p_{T,jet}} \cdot \sum_{i=1}^{N_{cl}} \Delta R\left(jet, cl_i\right) \cdot p_{T,cl_i}. \tag{4.6}$$

On the left side of Figure 4.2, the distribution of the jet width is shown for the central barrel region. The distribution is bell-shaped with a peak around ~ 0.1 rising from 0, where the jets consist of one cluster only, and falling towards its maximum value around 0.25, which is mainly affected by the size of the distance parameter of the anti-kt reconstruction algorithm.

The jet energy response distribution on the right side of Figure 4.2 shows the expected correlation with the energy of the jets. A lower response of about 0.8 is observed for lower energetic jets with a width above 0.1, but a strong correlation of the jet energy response with the width of the jets is not visible.

4.3.2. Eccentricity

The eccentricity [61] of a jet describes its profile in the calorimeter. It is a measure of the jet elongation in a range from 0, for perfectly circularly symmetric jet shapes, to 1, for infinitely elongated jet shapes.

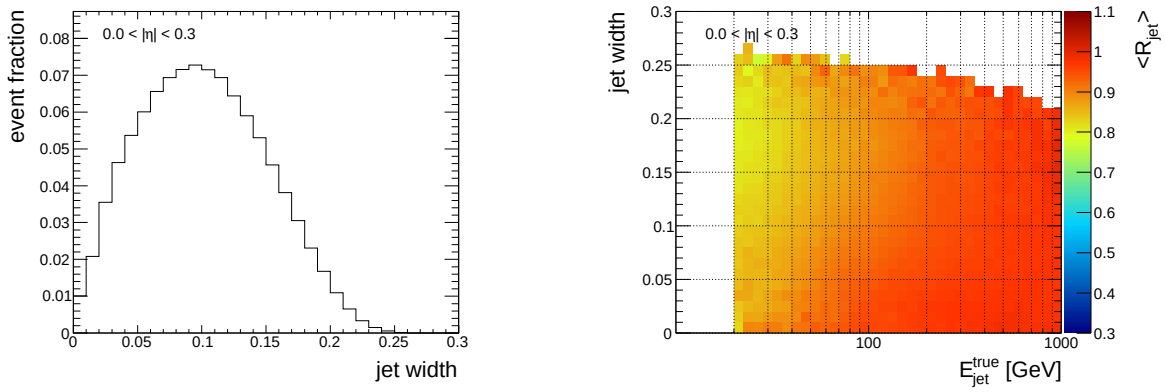

Figure 4.2.: Distribution of the jet width (left) and average jet energy response in the jet width – E_{jet}^{true} plane (right) for `AntiKt4LCTopoJets` in the central η-region. Further η-regions are shown in Appendix A.2.

The distribution of the jet eccentricity in the central η-region is shown on the left side of Figure 4.3. While only very few jets have a perfectly circular profile with an eccentricity of 0, the distribution has its peak position around 0.65 and falls afterwards steeply to 1.

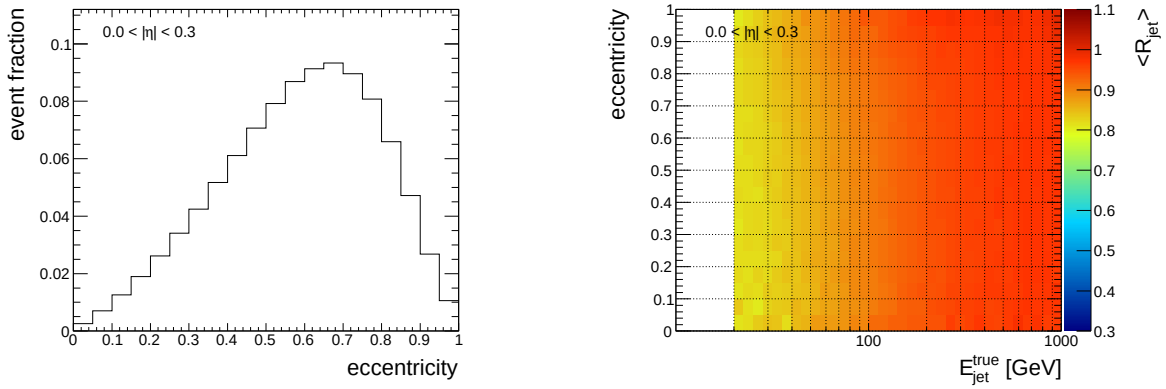

Figure 4.3.: Distribution of the jet eccentricity (left) and average jet energy response in the jet eccentricity – E_{jet}^{true} plane (right) for `AntiKt4LCTopoJets` in the central η-region. Further η-regions are shown in Appendix A.2.

The correlation of the jet energy response with the eccentricity of the jets is shown on the right side of Figure 4.3. Since the distribution is uniform with the eccentricity, no sensitivity to the non-linearity of the jet energy response are visible.

4.3.3. Isolation distance

A part from the variables describing the geometrical shape of the jets it is also interesting to analyse the environment of each jet. Since jets might be affected by other close-by jets or are split during reconstruction, it is interesting to study if the jet energy response depends on the isolation distance of a jet.

The isolation distance ΔR_{iso} is defined as the minimal distance to the axis of the closest jet in the event. Since two overlapping jets would be merged during the jet reconstruction, the minimal ΔR_{iso} is constrained by the distance parameter of the algorithm. In the case of `AntiKt4LCTopoJets`, the minimal distance between two jets is about $\Delta R_{iso} \sim 0.4$. The distribution on the left side of Figure 4.4 shows further, that about one third of the jets can be considered as close-by, up to an isolation distance of $\Delta R_{iso} \sim 0.6$. Beyond this, the spectrum is falling with larger distances up to perfectly isolated jets.

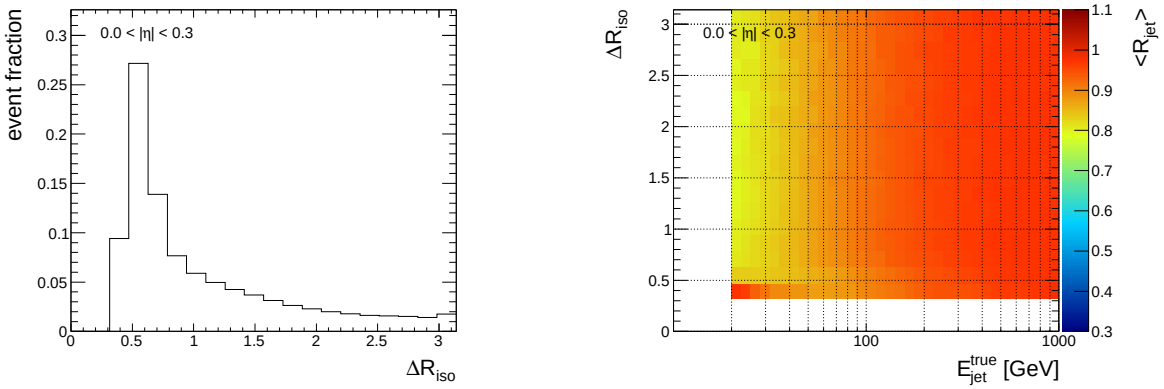

Figure 4.4.: Distribution of the isolation distance (left) and the average jet energy response in the $\Delta R_{iso} - E_{jet}^{true}$ plane (right) for `AntiKt4LCTopoJets` in the central η-region. Further η-regions are shown in Appendix A.2.

On the right side of Figure 4.4, the distribution of the average jet energy response in the $\Delta R_{iso} - E_{jet}^{true}$ plane is shown. In general, no strong correlation of the response with respect to the isolation distance is observed. The upwards fluctuation of the response in case of low energetic jets and very small distance to near by jets is due to statistical effects. In this case both the true jet energy and the distance ΔR_{iso} are on threshold.

4.3.4. Depth in the calorimeter

One cause of the non-linearity of the jet energy response is that hadron showers can already start in the upstream material before entering the calorimeter system. Thus the shower is not fully contained in the calorimeter. A helpful variable to study this effect is the depth of the jet inside the calorimeter system. This information can be extracted from the constituents of the jets, in particular from the cluster moment λ_{centre}^{cl} [40]. The depth of a jet in the calorimeter system, thus λ_{centre}^{jet}, is now defined as the energy weighted mean of the λ_{centre}^{cl} moment of its topological clusters.

$$\lambda_{centre}^{jet} = \frac{1}{E_{jet}} \cdot \sum_{i=1}^{N_{cl}} E_{cl} \cdot \lambda_{centre}^{cl} \tag{4.7}$$

The distribution of λ_{centre}^{jet} as shown on the left side of Figure 4.5 is bell-shaped with a peak at about $\lambda_{centre}^{jet} \sim 500\,\text{mm}$. It shows that most of the jets have a depth in the calorimeter between 100 and 1200 mm. Only a very small fraction of the jets enters deeper than 1200 mm.

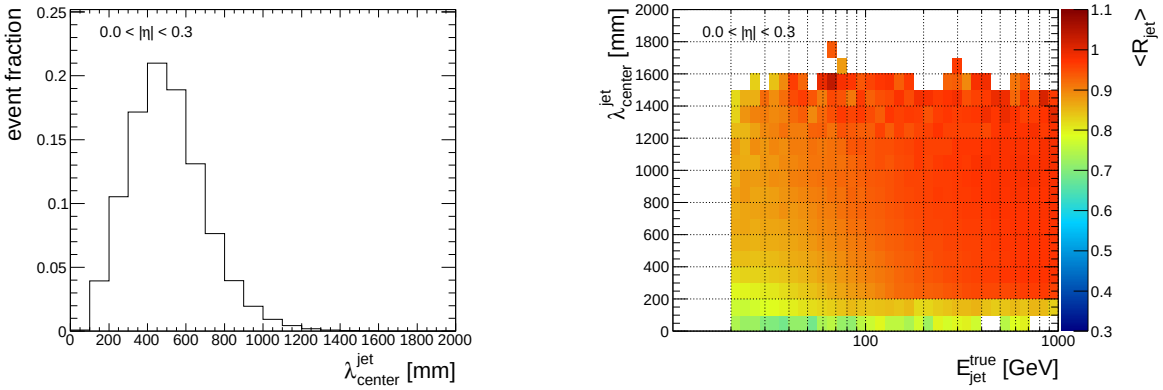

Figure 4.5.: Distribution of λ_{centre}^{jet} (left) and the average jet energy response in the $\lambda_{centre}^{jet} - E_{jet}^{true}$ plane (right) for `AntiKt4LCTopoJets` in the central η-region. Further η-regions are shown in Appendix A.2.

Figure 4.5 shows on the right side the jet energy response distribution in the $\lambda_{centre}^{jet} - E_{jet}^{true}$ plane. And this time, a clear dependence of the jet energy response from the depth in the calorimeter system is observed. Jets with a very small λ_{centre}^{jet} have an average response of about $\langle R_{jet} \rangle \sim 0.7$, while jet deeper located in the calorimeter, especially with higher energies have an response much closer to $\langle R_{jet} \rangle \sim 1$.

4.3.5. Transverse energy fraction of low energetic clusters

Hadron showers consist of particles within a wide spectrum of particle energies. In general, a certain fraction of the low energetic tail is cut because those particle are either stopped in the upstream material or far bended in the magnetic field. As a consequence, jets having a large fraction of low energetic particles might loose relatively more energy than jets having a smaller contribution from low energetic particles.

Since the number of jet constituents varies in different calorimeter regions, the transverse energy fraction of low energetic `TopoClusters` E_T^{frac} is found to better describe the contribution from low energetic particles. In the following a cluster is identified as low energetic if its transverse energy is just above the sensitivity threshold of the calorimeter and therefore less than $E_T^{cl} < 1\,\text{GeV}$. Hence, the transverse energy fraction E_T^{frac} is defined as the sum of the transverse energies of all low energetic clusters divided by the transverse energy of the entire jet

$$E_T^{frac} = \frac{1}{E_T^{jet}} \sum_{i=1}^{N_{cl}} E_T^{cl} \,(< 1\,\text{GeV}). \tag{4.8}$$

The distribution of E_T^{frac} is shown on the left side of Figure 4.6 for the central barrel region. It shows that more than 30 % of the jets have a significant contribution from low energetic `TopoClusters` to their transverse energy. Those jets are mostly low energetic and require a higher energy correction compared to higher energetic jets where E_T^{frac} is less dominant.

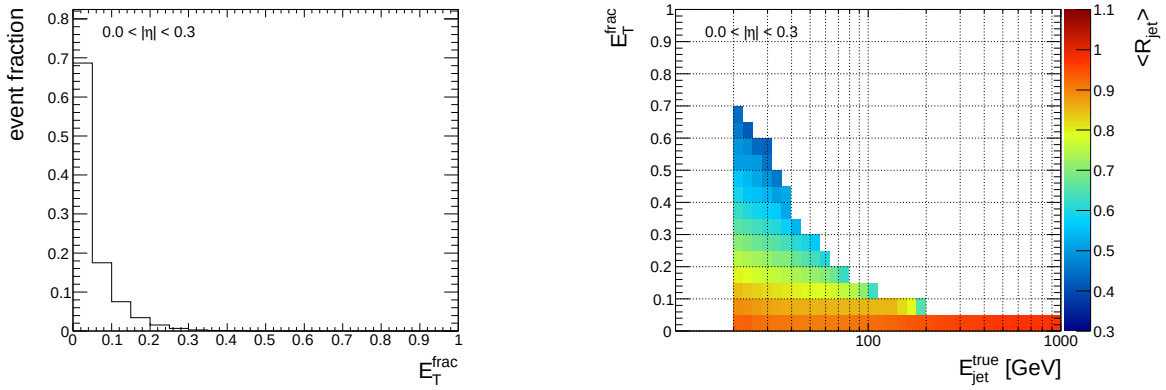

Figure 4.6.: Distribution of E_T^{frac} (left) and the average jet energy response in the $E_T^{frac} - E_{jet}^{true}$ plane (right) for `AntiKt4LCTopoJets` in the central η-region. More than 30 % of the jets have a significant contribution from low energetic clusters and show a sensitivity to the fluctuations of the average jet energy response. Further η-regions are shown in Appendix A.2.

On the right side of Figure 4.6, the distribution of the jet energy response in the $E_T^{frac} - E_{jet}^{true}$ plane is shown. While the average jet energy response is close to $\langle R_{jet} \rangle = 1$ for high energetic jets, it drops significantly down for low energetic jets in particular the higher the transverse energy fraction of low energetic clusters is. Compared to other jet shape variables of the analysis before, the fluctuations of the response are much larger here and a significant correlation to the E_T^{frac} variable is clearly visible. In particular for low energetic jets which require the largest corrections, the E_T^{frac} shows the best sensitivity and is thus the best candidate to be further studied as a phase space variable for the jet energy calibration.

4.4. Jet Energy Calibration Weight Factors

In order to derive a set of jet energy calibration weights, it is necessary to identify a phase space Φ made out of variables, which are sensitive to the non-linearity of the jet energy response. The studies in Section 4.2 show that the energy response fluctuates depending on the energy and the η-position of the jets but independently of the ϕ-position. For this reason, the ϕ-position can be neglected as a phase space variable.

Furthermore, the jet shape studies in the previous section show that the (E_{jet}, η_{jet})-phase space can be extended by the jet shape variable E_T^{frac}, which was found to show the best sensitivity to the non-linearity of the jet energy response. The result is the 3-dimensional phase space

$$\Phi^k = \Phi\left(E_{jet}^k, \eta_{jet}^k, E_T^{frac}\right), \tag{4.9}$$

where the energy and the η-position can be either taken from the reconstructed calorimeter jets ($k = reco$) or from the truth particle jets ($k = true$). Since the jet shape variable E_T^{frac} is only defined for calorimeter jets it has to be taken in any case from them. Finally, the goal is to derive a set of calibration weight factors in the phase space Φ^{reco} in order to be able to apply them to calorimeter jets in data.

The first step of the calculation process is finding pairs of reconstructed calorimeter jets and truth particle reference jets in a sample of simulated jet events. The geometrical matching criteria applied is a ΔR-cut of $\Delta R\,(reco, true) < 0.1$. Since both types of jets have an intrinsic transverse energy cut of $E_{T,jet} > 7\,\text{GeV}$ applied during the reconstruction algorithm, an additional cut to the collection of truth particle jets of $E_T^{true} > 14\,\text{GeV}$ is required. The asymmetric cut is needed to allow down fluctuations of the calorimeter jet energy E_{jet}^{reco} with respect to the truth reference.

In a second step, the jet energy response $R_{jet} = E_{jet}^{reco}/E_{jet}^{true}$ is calculated for all pairs of jets and filled into the respective phase space bin of Φ^{true}. As a result, the average jet energy response $\langle R_{jet}\rangle$ can be calculated and inverted for each phase space bin. This approach is preferred with respect to filling the phase space Φ^{reco} with the inverse response $1/R_{jet} = E_{jet}^{true}/E_{jet}^{reco}$ directly, because E_{jet}^{reco} suffers from large fluctuations. For this reason, it is neither used in the denominator of the jet energy ratio nor as a dimension of phase space to be filled.

In the last step, the binned response function $\langle R_{jet}\rangle\left(\Phi^{true}\right)$ is inverted into $\langle R_{jet}\rangle^{-1}\left(\Phi^{reco}\right)$. This requires the transformation of the η-position and the jet energy. Due to the tight matching criteria of $\Delta R\,(reco, true) < 0.1$, the η-positions of the matched jets are nearly identical and thus the η-transformation can be approximated by $\eta_{jet}^{reco} = \eta_{jet}^{true}$.

The fluctuations of the jet energies are much bigger and thus a numerical inversion procedure is required in order to convert the truth particle jet energies E_{jet}^{true} into calorimeter jet energies E_{jet}^{reco}. In order to allow for bin migration, the transformation $E_{jet}^{reco} = \langle R_{jet}\rangle\left(E_{jet}^{true}\right) \cdot E_{jet}^{true}$ is performed in sufficiently small steps by dividing each E_{jet}^{true}-bin into 10 sub-bins.

The resulting set of jet energy calibration weight factors is now given by the binned distribution of the inverse jet energy response

$$\text{calibration weight factor } = \langle R_{jet}\rangle^{-1}\left(\Phi^{reco}\right). \tag{4.10}$$

An additional advantage of inverting the average jet energy response instead of averaging the inverse jet energy response is that the calibration weight factor distribution in bins of E_{jet}^{reco} is getting independent of the initial energy spectrum from the generated jet sample.

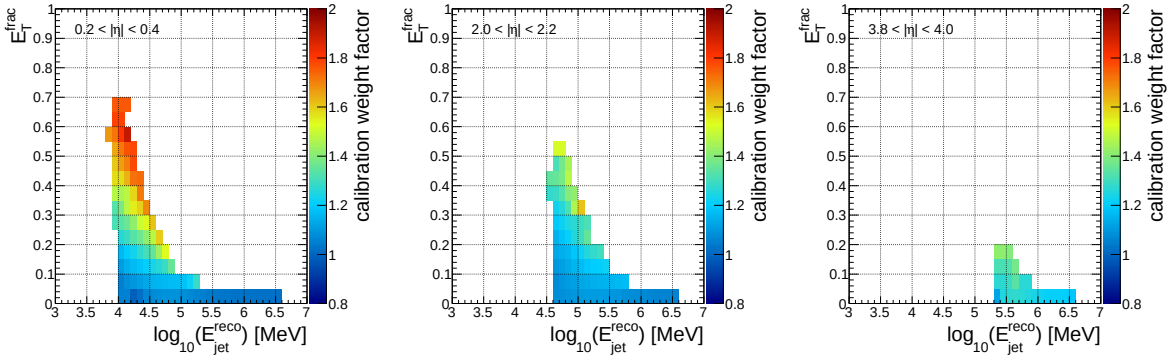

Figure 4.7.: Value of the jet energy calibration weight factors (colour code) in bins of $\log_{10}(E_{jet}^{reco})$ and E_T^{frac} for a characteristic η-region in the barrel (left), the endcap (centre) and the forward region (right). Low energetic jets with a big fraction of low E_T-clusters need larger corrections than low energetic jets with a smaller E_T^{frac} or higher energetic jets.

The set of jet energy calibration weight factors is shown in Figure 4.7, exemplarily for three characteristic η-regions. It is derived from simulated events of the combined QCD dijet samples (J0-J8), generated with `Pythia` [57] plus detector response simulation with `Geant4` [58]. Low energetic jets with a big E_T^{frac} receive larger corrections than low energetic jets with a smaller E_T^{frac} or higher energetic jets in general. For very high energetic jets, the sensitivity of the jet shape variable vanishes and the correction becomes independent of E_T^{frac}.

The jet-by-jet application of the weight factors and thus the energy calibration of the jets is part of the jet reconstruction and calibration process within the ATLAS framework. After the jet reconstruction from `LCTopoClusters`, the transverse energy fraction E_T^{frac} is calculated and the respective weight factor is looked up from a database, considering the jet energy and its η-position. The weight factor is applied to the jet four-vector, modifying its energy and momentum but leaving its direction unchanged. Due to the very high statistics of the QCD dijet samples, the phase space Φ^{reco} is very well covered. Nevertheless it can happen, that a required phase space bin is empty and thus no calibration weight factor exists. In those very rare cases, the four-vector remains unchanged.

4.5. Validation and Performance in Monte Carlo Events

The result of the jet reconstruction and energy calibration process is a collection of calorimeter jets, calibrated with respect to the truth particle level. In the following, the jet energy calibration method previously described is validated, analysing the linearity and resolution of the jet energy response. For consistency, the same QCD dijet processes used for the calculation of the weights

are taken. In addition, the performance of the jet energy calibration is tested considering different physics processes and thus different types of jets. Doing so, the impact of the jet shape variable and the magnitude of possible systematic biases are studied.

Similar to the studies presented in Section 4.2, the calorimeter jets are reconstructed from local hadron calibrated topological cell clusters using the anti-kt jet algorithm with a distance parameter of $d = 0.4$ (`AntiKt4LCTopoJets`). In addition the jet energy calibration weight factors are applied. As a reference, a collection of `AntiKt4TruthJets` is used with a tight matching cut of $\Delta R < 0.1$ and an additional transverse energy cut of $E_T^{true} > 20\,\mathrm{GeV}$.

4.5.1. Validation

In order to validate the jet energy calibration method, the linearity and resolution of the jet energy response is analysed. In particular, the jets are selected from a statistical independent sub-sample of the QCD dijet events used for the weights calculation before.

Figure 4.9 shows the distribution of the average jet energy response of `AntiKt4LCTopoJets` with respect to `AntiKt4TruthJets` after the final calibration step. In the $\phi_{\mathrm{jet}}^{\mathrm{true}} - \mathrm{E}_{\mathrm{jet}}^{\mathrm{true}}$ plane on the left side as well as in the $\eta_{\mathrm{jet}}^{\mathrm{true}} - \mathrm{E}_{\mathrm{jet}}^{\mathrm{true}}$ plane on the right side its is shown that the average jet energy response is restored to $\langle R_{jet} \rangle \sim 1.0$ within 1 %. Residual non-linearity of in maximum 3 % are only observed in the gap regions between the calorimeter subsystems around $|\eta| \sim 1.4$ and $|\eta| \sim 3.2$ as well as in the very forward region.

The development of the jet energy response for the three different energy calibration levels of `AntiKt4LCTopoJets` are shown in Figure 4.9 with respect to the energy of the truth particle reference jet. In the upper row, the average response is shown for a characteristic η region in the central barrel (left) and in the calorimeter endcap (right). Below each figure, the corresponding resolution is presented. The colour code of the figures indicates the jets on the electromagnetic scale (em scale) in red, the scale after local hadron calibration of the constituents (const scale) in yellow and after final calibration (final scale) in blue.

Similar in all detector regions, the average jet energy response improves with each calibration step from the electromagnetic to the final scale. It is restored to $\langle R_{jet} \rangle \sim 1.0$ with residual non-linearity of the order of 1 %. Consistently with the distribution of the calibration weight factors, the size of the final correction step varies with energy and η-region. It is getting smaller for higher jet energies and bigger going forward to higher η-values.

Also the development of the response resolution shows a general improvement after each calibration step. Compared to the improvement after the constituent calibration step, the correction after the final calibration step is relatively small, but significant for all energies and η-regions.

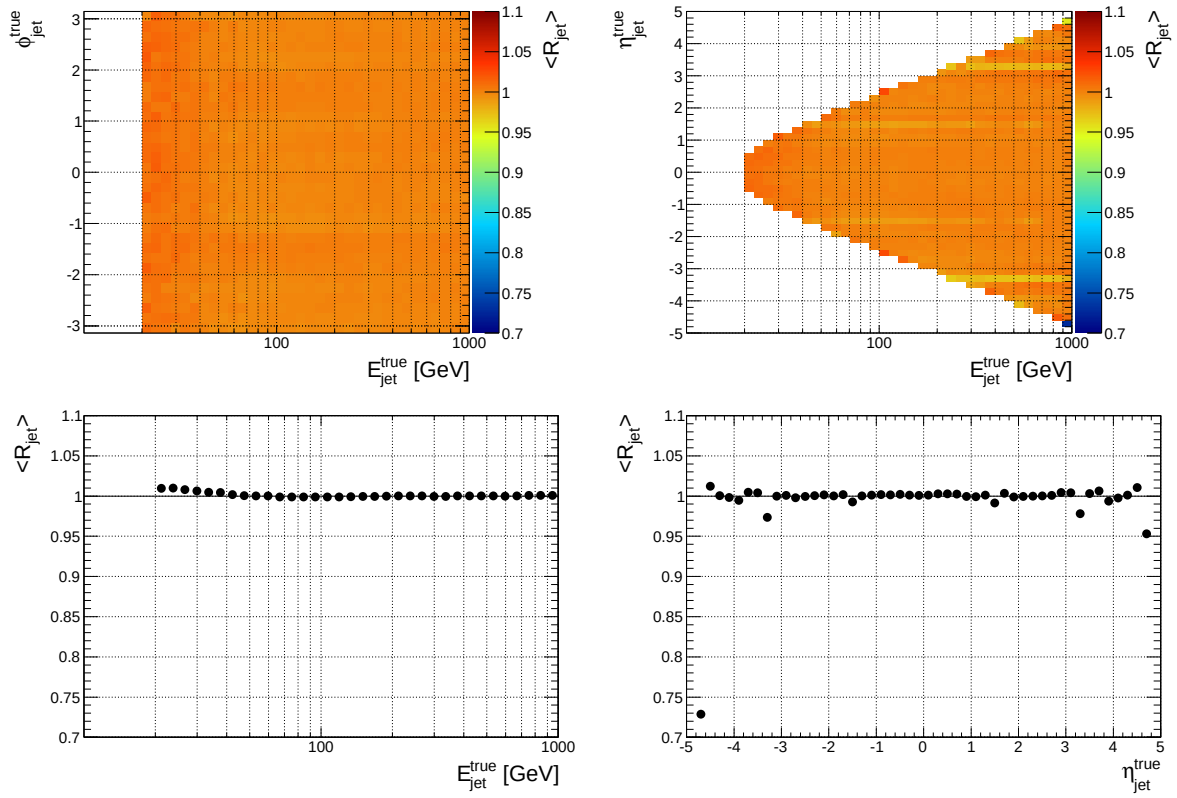

Figure 4.8.: Average jet energy response $\langle R_{jet} \rangle$ of `AntiKt4LCTopoJets` with respect to `AntiKt4TruthJets` after the final calibration step. The upper row shows the $\phi^{\text{true}}_{\text{jet}} - \text{E}^{\text{true}}_{\text{jet}}$ (left) and $\eta^{\text{true}}_{\text{jet}} - \text{E}^{\text{true}}_{\text{jet}}$ plane (right), while the projections to the E^{true}_{jet} (left) and η^{true}_{jet}-axis can be found in the lower row. The colour code indicates areas with a lower response in blue, changing over green and yellow to red for areas with higher jet energy response. After the calibration process, the average jet energy response is linear in ϕ, η and jet energy within 1 % with larger non-linearity of in maximum 3 % only in the gaps between the calorimeter subsystems as well as in the forward region.

4.5.2. Performance

In order to study the performance of the calibration method, the impact of the jet shape variable on the result of the calibration is analysed. Therefore, a second set of calibration weight factors is calculated, excluding E_T^{frac}. This results in an effective (E_{jet}, η_{jet})-phase space. On the other hand, the same sample of jets and the same calculation and application algorithms are used in order to ensure a consistent comparison of the samples with and without considering the jet shape variable for the energy calibration.

In addition to this, the dependence of the underlying physics process is studied. The goal is to get an estimation of the size of the expected systematic biases if the origin of the calorimeter jets differs from the weight calculation process. Therefore, the jets on the final calibration scale are analysed in three different Monte Carlo samples, varying the physics process and the Monte Carlo event generator.

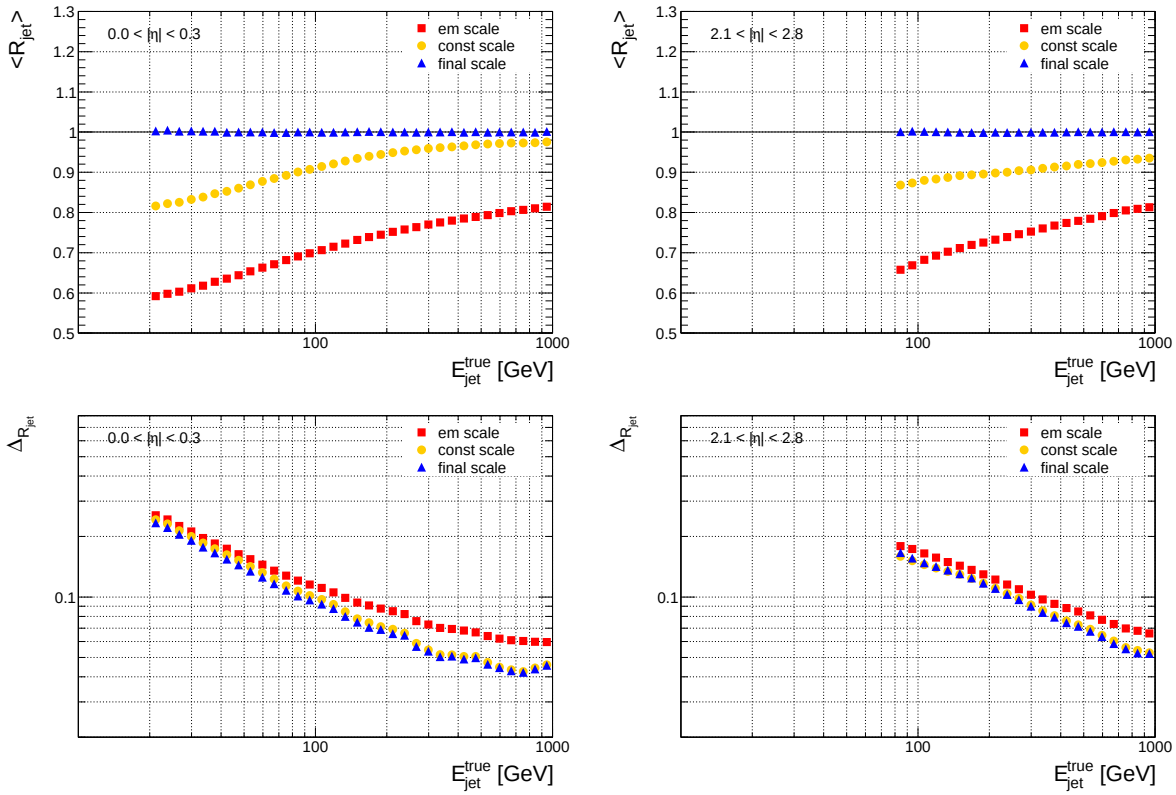

Figure 4.9.: Development of the average jet energy response $\langle R_{jet} \rangle$ of `AntiKt4LCTopoJets` with respect to `AntiKt4TruthJets` for three different calibration steps. The electromagnetic scale (em scale) is indicated in red, the scale of the calibrated constituents (const scale) in yellow and scale after final calibration to the truth particle level (final scale) in blue. For both η-regions, the central barrel (left) and the endcap calorimeter (right), an improvement of the response linearity is observed after each calibration step. Furthermore, also the resolution of the jet energy response $\Delta_{R_{jet}}$ improves after calibration as shown in the figures of the lower row.

QCD Dijet Events

The first jet sample is derived from the same QCD dijet sample described and validated above. Since the calibration weight factors are derived from similar events, the expected deviations from $\langle R_{jet} \rangle = 1.0$ are very small.

Figure 4.10 shows a comparison of the performance of the final calibration level with and without taking the jet shape variable E_T^{frac} into account for the calculation of the weights. The non-linearity observed are very small and within less than 1 %, but especially in the central barrel region of the calorimeter system, the jet corrections which consider the E_T^{frac}-variable have smaller deviations from $\langle R_{jet} \rangle = 1.0$. Nevertheless, the differences are much below the percent level. In addition, no significant difference of the resolution among the two cases is observed.

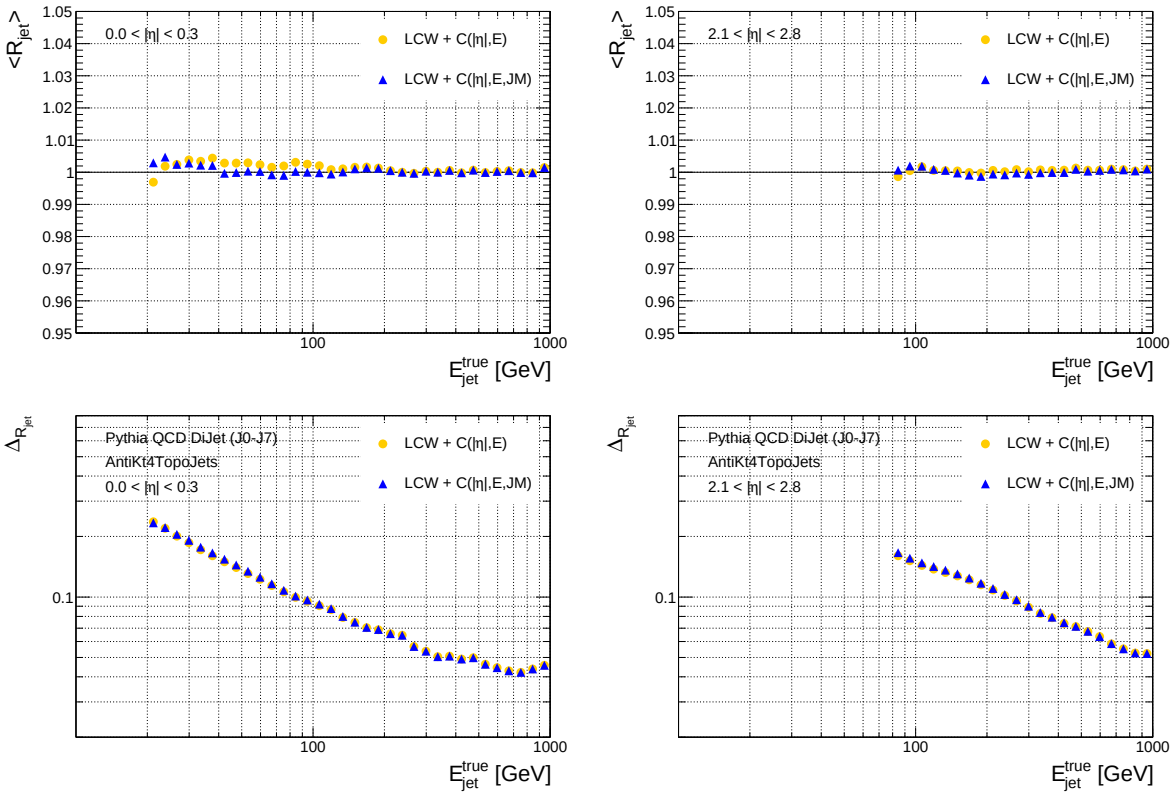

Figure 4.10.: Average jet energy response $\langle R_{jet} \rangle$ of `AntiKt4LCTopoJets` with respect to `AntiKt4TruthJets` in QCD dijet events. Both sets of jets are shown after the final calibration step, with (blue) and without (yellow) taking the jet shape variable E_T^{frac} into account. While in the central barrel (left) the set considering E_T^{frac} is in general closer to $\langle R_{jet} \rangle = 1$, both sets of jets show similar results in the endcap region (right). The resolution $\Delta_{R_{jet}}$ is shown in the lower row and is similar for both sets of jets in all detector regions.

The result of this study shows, that the discriminative power of the jet shape variable E_T^{frac} is limited when the constitution of the jet sample is close to the sample where the calibration weight factors are derived from. In this case, the impact of the jet energy and of the η-position of the jet is dominating.

QCD Multijet Events

An analysis of the QCD multijet samples allow for an independent cross check of the calibration method in QCD jet events. In contrast to the dijet samples generated with the `Pythia` [57] generator, the `Alpgen` [62] event generator allows for a full leading order calculation of the matrix element, including multi parton final states from processes up to $2 \rightarrow 6$. While for the dijet samples `Pythia` is used for the parton showering as well, `Herwig` [63] is used in case of the multijet events. Nevertheless, the resulting `Alpgen`-multijet sample and the `Pythia`-dijet sample have a similar quark/gluon composition and only small differences in few phase space regions are expected.

In Figure 4.11, the comparison of the final calibration level with and without considering the jet shape variable E_T^{frac} is shown. Even if the calibration weights are applied here to a set of jets derived from a different Monte Carlo sample, the deviations from $\langle R_{jet} \rangle = 1.0$ are very small and within 1 %. In general, the average jet energy response of the jet sample considering E_T^{frac} is closer to $\langle R_{jet} \rangle = 1.0$. However, no significant differences on the performance of the response resolution are observed.

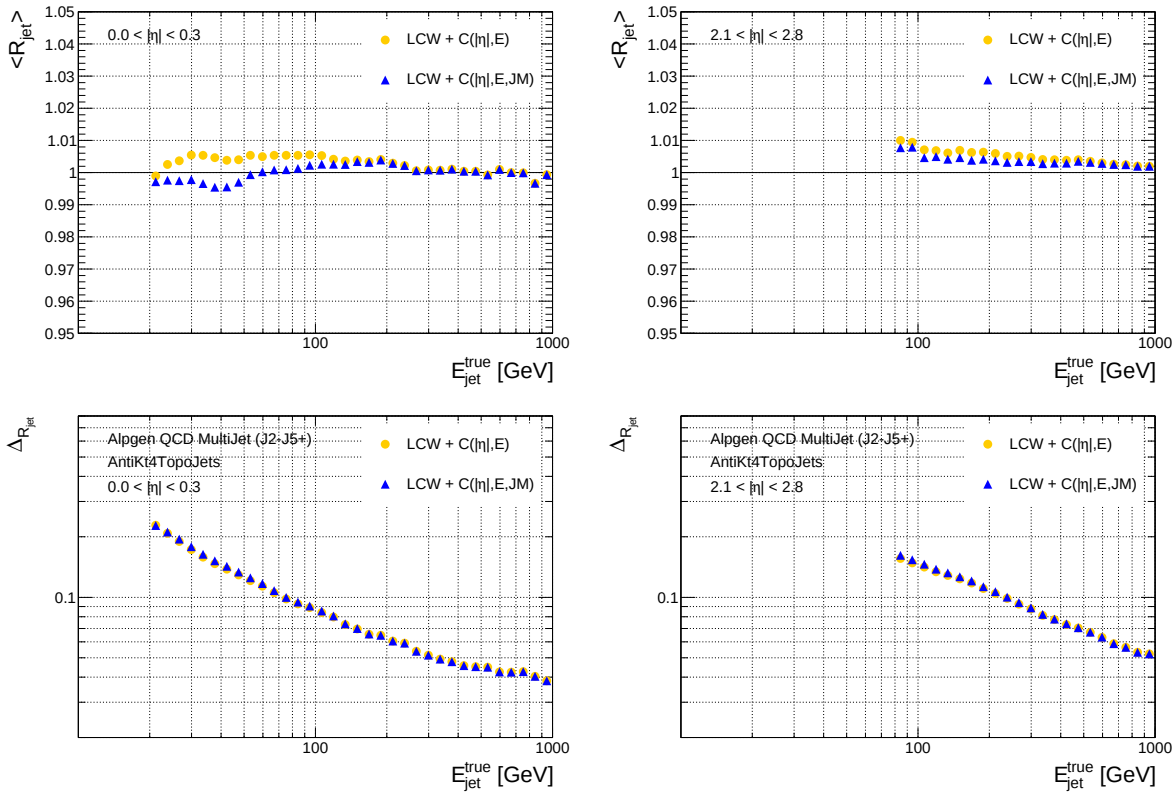

Figure 4.11.: Average jet energy response $\langle R_{jet} \rangle$ of `AntiKt4LCTopoJets` with respect to `AntiKt4TruthJets` in QCD multijet events. Both sets of jets are shown after the final calibration step, with (blue) and without (yellow) taking the jet shape variable E_T^{frac} into account. In the central barrel (left) as well as in the endcap region (right), the set considering E_T^{frac} is closer to $\langle R_{jet} \rangle = 1$. The resolution $\Delta_{R_{jet}}$ is shown in the lower row and is similar for both sets of jets in all detector regions.

All Hadronic Top Quark Pair Decays

The QCD jet samples previously studied are dominated by gluon jets since the quark/gluon ratio in $2 \rightarrow 2$ processes decreases from 10% to 1% towards higher jet energies. In order to analyse the impact of the calibration method on a quark jet dominated sample, all hadronic $t\bar{t}$-events are studied. The events are generated with the `MC@NLO` [64] event generator, using `Herwig` [63] for the parton showering and `Jimmy` [65] for the hadronisation process. The resulting jet sample consists of jets from light and heavy quarks with a small fraction of jets from gluon radiation.

Figure 4.12 shows a comparison of the performance of the final calibration with and without taking the jet shape variable E_T^{frac} into account for the calculation of the weights. Compared to the QCD jet samples, the deviations from $\langle R_{jet} \rangle = 1.0$ are bit larger, in particular for lower jet energies. Here, the consideration of the jet shape variable for the weights calculation shows a significant impact on the size of the non-linearity. Taking the jet shape variable E_T^{frac} into account for the energy calibration leads to an improvement of the maximum deviation of the average response from 3 % to 1.5 %. Even if no significant difference for the resolution of the response is observed, the dependence of the calibration method from the nature of the jets is significantly reduced.

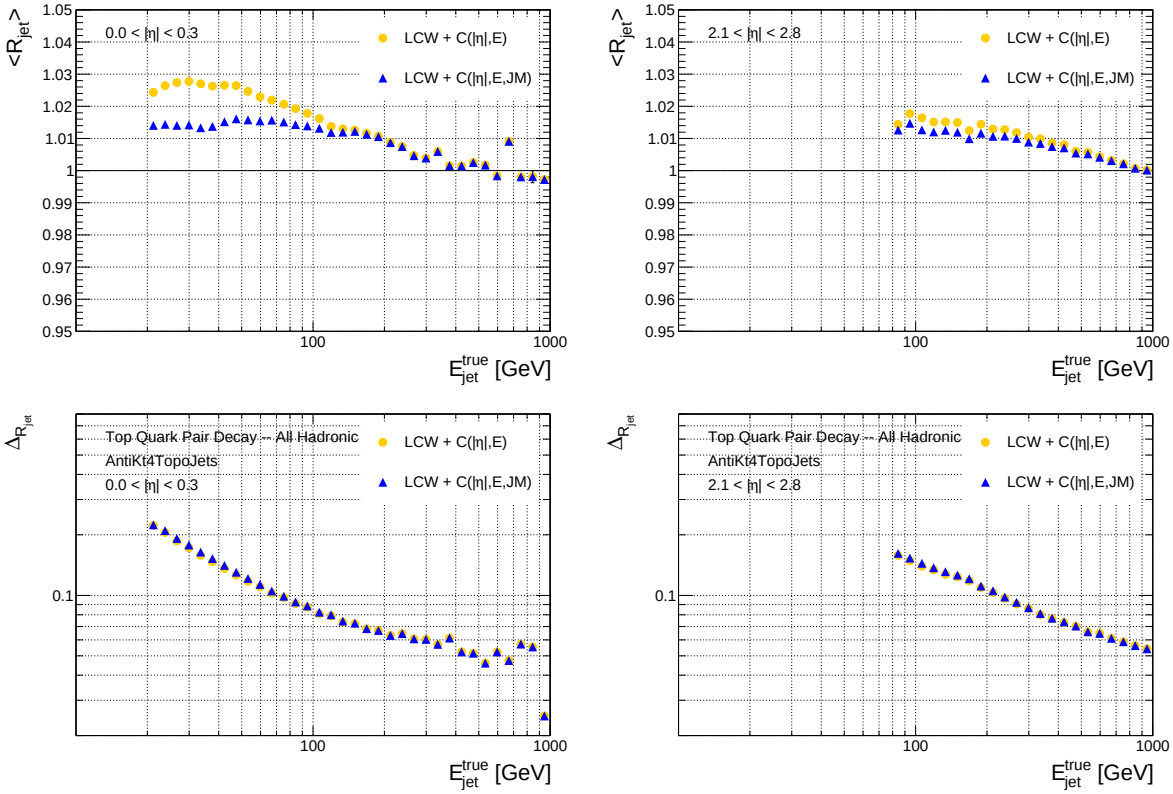

Figure 4.12.: Average jet energy response $\langle R_{jet} \rangle$ of `AntiKt4LCTopoJets` with respect to `AntiKt4TruthJets` in all hadronic top quark pair events. Both sets of jets are shown after the final calibration step, with (blue) and without (yellow) taking the jet shape variable E_T^{frac} into account. In the central barrel (left) as well as in the endcap region (right), the set considering E_T^{frac} is closer to $\langle R_{jet} \rangle = 1$. The resolution $\Delta_{R_{jet}}$ is shown in the lower row and is similar for both sets of jets in all detector regions.

4.6. Validation and Performance in First Data Events

The Large Hadron Collider was successfully restarted on the 20th of November 2009. Only three days later, the first proton-proton collisions were established with the ATLAS detector. In the following few weeks, the beam conditions were stabilised and proton-proton collision data at

a centre-of-mass energy of $\sqrt{s} = 900\,\text{GeV}$ was taken. In the following, the recorded events of these early runs are studied in order to validated the performance of the jet energy calibration method in comparison with Monte Carlo simulation.

The events were selected using the level 1 minimum bias trigger scintillators (MBTS). This special trigger devices are installed on both sides of the ATLAS detector and cover a pseudo-rapidity range of $2.09 < |\eta| < 3.84$ [46]. In order to remove events from cosmic muons, from beam halo interaction and from proton scattering on beam gas particles, further offline cleaning cuts are applied on the MBTS hits and the calorimeter timing. In addition, collision runs are only considered if the inner detector system, the calorimeter system and the solenoid magnet were fully operational at data taking [66].

The result is a dataset of 330810 events which is studied and compared to events from a Monte Carlo simulation of proton-proton collisions based on a combination of non-, single- and double-diffractive processes. The events are generated with `Pythia` [57] including ATLAS MC09 tuning [67] and the detector response is simulated with `Geant4` [58]. The same trigger and the same event selection criteria are applied to Monte Carlo and data.

4.6.1. Validation of Jet Properties

The first step of the data analysis is a comparison of jets in early data events to jets from Monte Carlo simulation. Therefore, the distributions of a basic set of jet properties are presented in Figure 4.13. In both cases, the jets are reconstructed from pre-calibrated topological cell clusters using the anti-kt algorithm with a distance parameter of $D = 0.4$. For the energy calibration of the jets, local hadron calibration is used for the clusters and an additional jet level calibration considering the jet shape variable E_T^{frac} is applied (cf. Section 4.4).

The jet properties shown in Figure 4.13 are the number of jets (upper left), the transverse energy (upper right), the η- (middle left) and ϕ-position (middle right), the energy (lower left) and the jet shape variable E_T^{frac} (lower right). The results from data are shown as black dots with vertical error bars for the statistical error while the expectation from Monte Carlo simulation is shown as orange shaded histogram. In order to make the different statistics of data and Monte Carlo comparable, the area of the distributions from Monte Carlo simulation is normalised to the area of the data histograms.

The results show, that already at a centre-of-mass energy of $\sqrt{s} = 900\,\text{GeV}$, up to three jets with $E_{T,jet} > 7\,\text{GeV}$ per event are expected and also measured. The measured transverse energy of the jets goes up to $E_{T,jet} \sim 40\,\text{GeV}$ which fits the expectation of the simulated minimum bias events. Also the spherical distribution of the jets, the η- and ϕ-position, follow the expectation and show their typical symmetric distribution.

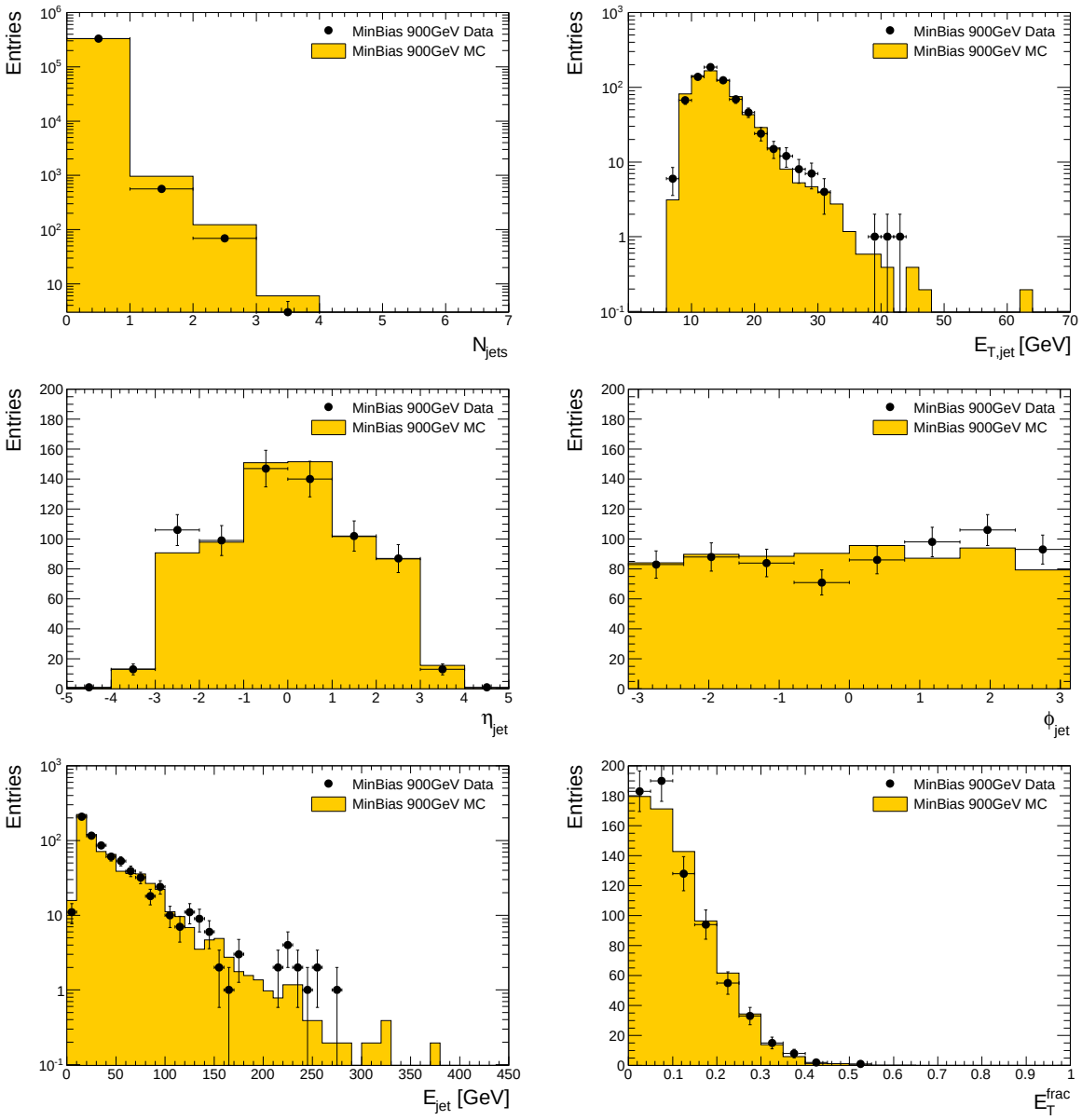

Figure 4.13.: Comparison of jets in early data events (black dots) and from Monte Carlo simulation (orange area). The distributions for the basic jet properties, number of jets (upper left), transverse energy (upper right), the η- (middle left) and ϕ-position (middle right), the jet energy (lower left) and the jet shape variable E_T^{frac} (lower right) are presented. The overall agreement of data and Monte Carlo is reasonable and most of the differences are within statistical errors.

In order to complete the set of input variables of jet energy calibration, the distribution of the jet energy and the jet shape variable E_T^{frac} are presented. As well, both variables show a good agreement of data and Monte Carlo within statistical errors which gives confidence to the input parameters of the jet energy calibration.

In general, the distributions from data and Monte Carlo simulation show a reasonable agreement, in particular considering the very early phase of data taking and Monte Carlo tuning [66]. Most

of the differences are within statistical fluctuations or result from the low statistics of the small dataset. Since the data taking is going on and the recorded integrated luminosity as well as the centre-of-mass energy are increasing, deviations from statistical fluctuations will play a minor role in the future and a further tuning of the Monte Carlo simulation can be performed.

4.6.2. Validation of the Jet Energy Calibration

In the second part of the data analysis, the performance of the jet energy calibration method is studied in events from early data taking. In order to validate the jet energy scale after the final calibration step, the energy ratio with respect to the previous calibration levels is calculated for each jet individually. In particular, the ratio of the final calibration scale to the electromagnetic scale $E_{jet}^{fi}/E_{jet}^{em}$ and the ratio of the final calibration scale to the pre-calibrated constituent level $E_{jet}^{fi}/E_{jet}^{co}$ are considered.

The distribution of these two energy ratios is studied with respect to the three input variables of the jet energy calibration method, E_{jet}, η_{jet} and E_T^{frac}. The result from early data is shown as black dots with vertical statistical error bars in the upper part of the Figures 4.14 to 4.16. It is compared to Monte Carlo simulation, indicated by the range of the statistical error shown as orange shaded band. In order to quantify the agreement of data and Monte Carlo simulation, the ratio of both distributions is shown in the bottom part of each figure.

Figure 4.14 shows the distribution of $E_{jet}^{fi}/E_{jet}^{em}$ (left) and $E_{jet}^{fi}/E_{jet}^{co}$ (right) with respect to the energy of the jet at the electromagnetic scale. Compared to the phase space of the calibration weight factors, the minimum bias events are dominated by low energetic jets within the sensitivity range of the jet shape variable. The overall correction from electromagnetic to final scale is about ~ 1.7 for jet energies up to $E_{jet}^{em} \sim 30\,\text{GeV}$ and drops down to ~ 1.4 towards $E_{jet}^{em} \sim 100\,\text{GeV}$.

The corrections from constituent level to final calibration scale on the right side of Figure 4.14 are smaller and included in the energy ratio of the right side. Their average is about ~ 1.15 for jet energies up to $E_{jet}^{em} \sim 30\,\text{GeV}$ and drops down to ~ 1.1 towards $E_{jet}^{em} \sim 100\,\text{GeV}$. For both cases, the agreement between data and Monte Carlo simulation is very good and within about $\sim 2\,\%$ over the entire energy range up to $E_{jet}^{em} \sim 100\,\text{GeV}$. Beyond this, the statistics of the dataset is to limited in order to draw a conclusion.

In Figure 4.15, the energy ratios of $E_{jet}^{fi}/E_{jet}^{em}$ (left) and $E_{jet}^{fi}/E_{jet}^{co}$ (right) are shown with respect to the η-position of the jets. As expected, the size of the correction fluctuates very much with the η-position. In particular, the average correction get larger in the cap regions between the calorimeter subsystems around $|\eta| \sim 1.4$ and $|\eta| \sim 3.2$. The overall agreement between data and Monte Carlo simulation is still within $2\,\%$, but suffers from the limited statistics of the dataset in the forward regions beyond $\eta > 3.2$.

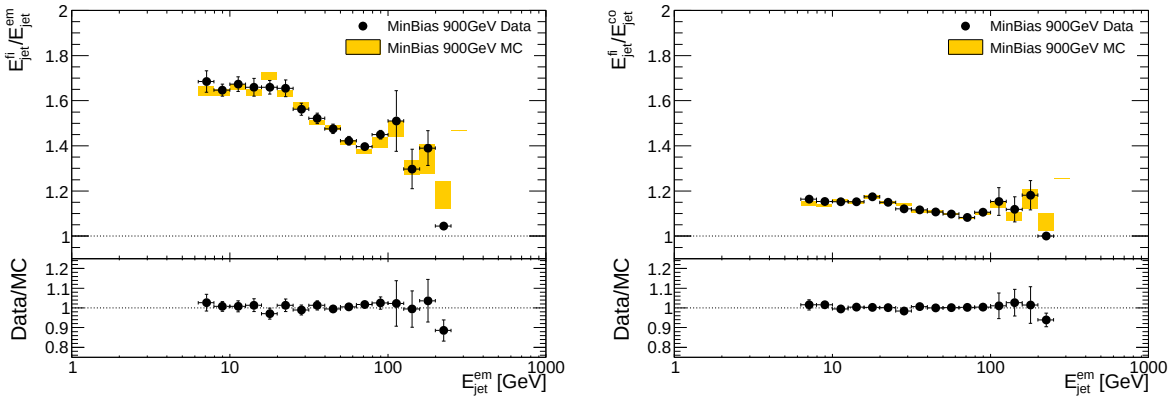

Figure 4.14.: Distribution of the average energy ratios $E_{jet}^{fi}/E_{jet}^{em}$ (left) and $E_{jet}^{fi}/E_{jet}^{co}$ (right) with respect to the energy of the jet E_{jet}^{em}. Events from early data are indicated with black dots including vertical statistical error bar and compare to Monte Carlo simulation, where the orange shaded areas represent the statistical error. In the bottom part of each plot, the ratio of the mean between data and Monte Carlo is shown. The result is an overall agreement within $\sim 2\,\%$ over almost the entire energy range.

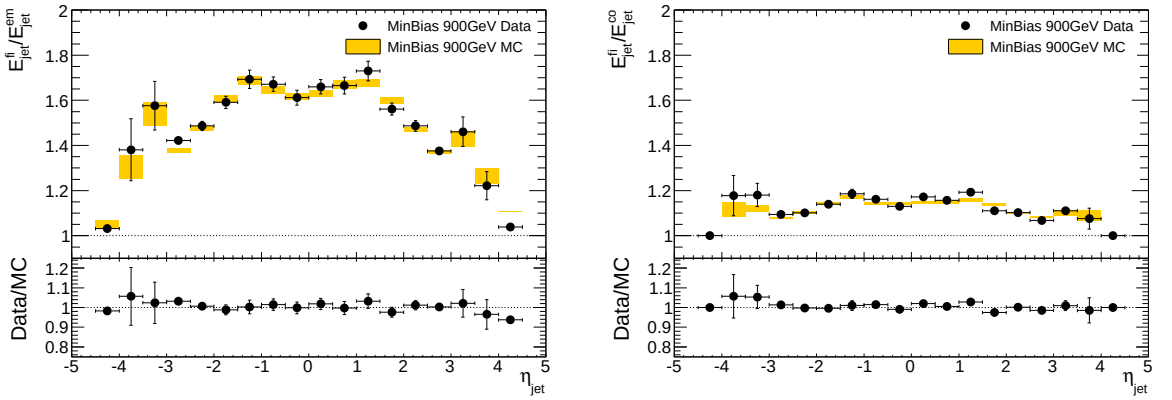

Figure 4.15.: Distribution of the average energy ratios $E_{jet}^{fi}/E_{jet}^{em}$ (left) and $E_{jet}^{fi}/E_{jet}^{co}$ (right) with respect to the η-position of the jets. Events from early data are indicated with black dots including vertical statistical error bar and compare to Monte Carlo simulation, where the orange shaded areas represent the statistical error. In the bottom part of each plot, the ratio of the mean between data and Monte Carlo is shown. The result is an overall agreement within $\sim 2\,\%$ over almost the entire η-range.

The distributions of the energy ratios of $E_{jet}^{fi}/E_{jet}^{em}$ (left) and $E_{jet}^{fi}/E_{jet}^{co}$ (right) with respect to the jet shape variable E_T^{frac} are shown in Figure 4.16. The overall trend shows larger corrections the larger the transverse energy fraction of low energetic clusters is. The magnitude of the second correction step on the right side of Figure 4.16 is consistent with the magnitude of the energy calibration weight factors.

In the bottom part of both plots, the ratio of the mean between data and Monte Carlo is shown. The agreement of data and Monte Carlo simulation is reasonable up to values of $E_T^{frac} \sim 0.4$ and within $2\,\%$. Beyond this, the result suffers from the limited statistics of the dataset.

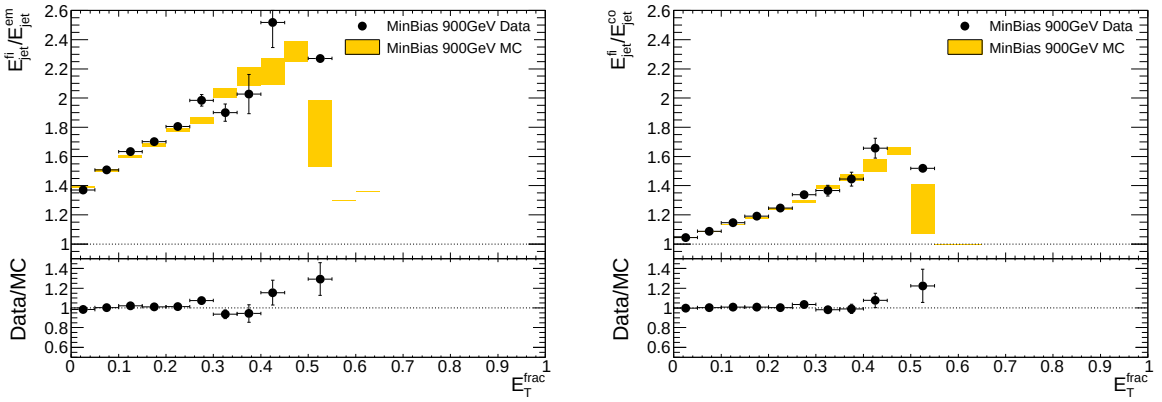

Figure 4.16.: Distribution of the average energy ratios $E_{jet}^{fi}/E_{jet}^{em}$ (left) and $E_{jet}^{fi}/E_{jet}^{co}$ (right) with respect to the jet shape variable E_T^{frac}. Events from early data are indicated with black dots including vertical statistical error bar and compare to Monte Carlo simulation, where the orange shaded areas represent the statistical error. In the bottom part of each plot, the ratio of the mean between data and Monte Carlo is shown. The result is an overall agreement within $\sim 2\,\%$ over the entire range of E_T^{frac}.

4.6.3. Conclusion

The first results on jets from minimum bias proton-proton collisions at a centre-of-mass energy of $\sqrt{s} = 900\,\text{GeV}$ are very promising. The overall agreement between early ATLAS data and Monte Carlo simulation is reasonable and shows a good understanding of the detector already in this early phase.

The distributions of all analysed jet properties are in reasonable agreement with the expectations from Monte Carlo simulation within statistical errors. Furthermore, a consistency check for the energy of the jets after final calibration has been performed with respect to the electromagnetic and the constituent scale. The result is an overall agreement between data and Monte Carlo simulation within $2\,\%$. Similar studies were performed for the various calibration levels of the local hadron calibration [66].

4.7. Summary and Outlook

In order to develop a new jet energy calibration method for ATLAS, a large set of jet shape variables has been analysed. For calorimeter jets, reconstructed from local hadron calibrated topological cell clusters, the sensitivity to the non-linearities of the jet energy response has been investigated. Among the various jet shape variables only the transverse energy fraction of low energetic clusters E_T^{frac} shows a significant sensitivity and thus is considered to extend the phase space for the calculation of the calibration weight factors.

In the next step, a new set of calibration coefficients was calculated within the 3-dimensional phase space $\Phi\left(E_{jet}^{reco}, \eta_{jet}^{reco}, E_T^{frac}\right)$, using a numerical inversion technique to transform the jet energy dimension. The software packages for the calculation and application of the weight factors are fully integrated within the ATLAS software framework.

The result of the calibration process is a set of jets with an average jet energy response close to $\langle R_{jet} \rangle = 1.0$, linear over a wide range of energies and η-regions within 1 %. It was further shown that considering the jet shape variable E_T^{frac} helps to reduce the dependencies on the underlying physics process. A small improvement in resolution of the energy response $\Delta_{R_{jet}}$ was observed with respect to the constituent level.

In an analysis of the first minimum bias proton-proton collision data at a centre-of-mass energy of $\sqrt{s} = 900\,\text{GeV}$, a good agreement between data and Monte Carlo simulation was verified for the major jet properties including the input variables of the jet energy calibration.

Furthermore, a comparison of the final jet energy scale with the previous calibration steps showed a consistent behaviour in data and Monte Carlo, with an overall agreement within 2 %. These results are very promising and give confidence to the jet energy calibration method considering the jet shape variable E_T^{frac}.

The development of the jet energy calibration method is an ongoing process and thus several ideas for further improvements are going to be studied. Even if the jet shape variable E_T^{frac} showed already good results, the analysis of additional jet shape variables is still ongoing. One way to further improve the impact of the jet properties is to consider also track based jet shape variable reconstructed from hits in the inner detector system.

Besides, the software packages to calculate and apply the calibration weight factors leave space for further developments. In order to reduce the binning effect of the phase space holding the calibration weights, a multidimensional interpolation method can be applied. In addition, an extrapolation method is needed in order to cover empty phase space points. Those arising from low statistics as well as from an imperfect description of the data in the Monte Carlo simulation, in particular for lower jet energies.

5. Top Quark Mass Measurement in the Lepton plus Jets Channel

With the first proton-proton collisions at the Large Hadron Collider, a new era of top quark physics has started. Due to the high top quark production rate at the LHC, the properties of the top quark can be measured with an unprecedented accuracy. However, hadronic top quark decays can be used for jet energy calibration studies and as an input to in-situ calibration methods for light and b-quark jets.

One of the early data analyses feasible at the LHC is the measurement of the top quark mass in the **lepton plus jets** $t\bar{t}$-decay channel. As described in Chapter 1, this channel has a sufficient cross section and offers a clean trigger signature from the high energetic lepton of the W-boson decay. In the following, only cases where the lepton is either an electron (**electron channel**) or a muon (**muon channel**) are considered since both leptons are directly measurable with the ATLAS detector. In contrast, tau leptons are only measured through their decay products which decreases their detection efficiency significantly. While the leptonic branch serves further as an important input to the offline event selection, the hadronic branch offers the possibility of a full reconstruction of the top quark four-vector from calorimeter jets.

In the following chapter, a Monte Carlo study for a prospective top quark mass measurement is presented. It represents an analysis of $\mathscr{L} = 200\,\mathrm{pb}^{-1}$ of proton-proton collision data taken by the ATLAS experiment. The Monte Carlo samples for the signal and most important background processes originate from the **MC08** production and are generated with a centre-of-mass energy of $\sqrt{s} = 10\,\mathrm{TeV}$ including a full detector response simulation.

The first part of the analysis is a cut based selection of $t\bar{t}$-candidate events. Selection cuts on dedicated variables are optimised in order to assure the basic properties of the signal process. The goal is to select a significant amount of signal events and to efficiently reject events from physics background processes. The derived set of selected events is used as an input to the reconstruction of the top quark four-vector.

The event selection is followed by a study of three different methods to reconstruct the hadronic branch of the $t\bar{t}$-decay. The focus of this investigation is on minimising the background from wrong combinations of jets (**combinatorial background**). The reconstruction methods are compared to each other at several levels of Monte Carlo simulation, from the generated partons to the reconstructed calorimeter jet level including full detector simulation. This allows for a systematic study of possible biases in the event reconstruction.

In the final part of the analysis, a top quark mass measurement from the invariant mass distribution of the three selected jets is exercised for a typical pseudo experiment of $\mathscr{L} = 200\,\mathrm{pb}^{-1}$. A **Combined Fit** of the signal plus background 3-jet invariant mass distribution is performed, assuming the mean of the signal part as a good estimator of the top quark pole mass. Furthermore, a complete study of systematic uncertainties is performed, varying the most important parameters of the event generation and signal reconstruction.

5.1. Signal and Background Processes – Monte Carlo Samples

The expected dataset is simulated including all relevant signal and background processes for a top mass analysis at the LHC. The pseudo-data samples for each process are generated individually using different Monte Carlo generators assuming proton-proton collisions at a centre-of-mass energy of $\sqrt{s} = 10\,\mathrm{TeV}$ (**MC08** production). The detector response of ATLAS is simulated with `Geant4` [58] and the reconstruction of the detector signal is performed using the ATLAS software framework `Athena` (release version 14.2.10.1). All Monte Carlo samples have been centrally produced by the ATLAS collaboration and are described in more detail, including validation studies and a comparison of different generators, in the ATLAS note [68].

5.1.1. Signal Processes

The goal of the analysis is the measurement of the top quark mass in the **lepton plus jets** decay channel of top quark pair events (cf. Chapter 1). As described before, only the branches where the charged lepton is either an electron or a muon are considered as signal process. Thus, the expected event signature of the signal process in the detector is:

- exactly **1** isolated lepton (e or μ) with a high transverse momentum,
- at least **4** calorimeter jets with high transverse momentum from the quark-initiated particle shower
- and large missing transverse energy from the undetected neutrino of the leptonic W-boson decay.

For all $\mathrm{t\bar{t}}$-events, the hard scattering process is generated using the next-to-leading order Monte Carlo generator `MC@NLO` [64] and the `CTEQ6M` [69] parton distribution function which allows for taking additional gluon radiation into account. The parton shower and hadronisation process is simulated with `Herwig` [63] and the underlying event with `Jimmy` [65].

The reference top mass of the generated $t\bar{t}$-sample is fixed to

$$m_t^{gen} = 172.5\,\text{GeV}, \tag{5.1}$$

without Breit-Wigner description (switched off in MC@NLO for this production series). The NLO $t\bar{t}$-production cross section is scaled up to the NNLO value of

$$\sigma_{t\bar{t}}^{NNLO} = 401.60\,\text{pb}\,{}^{+3.7\%}_{-4.3\%}|_{\text{Scales}}\,{}^{+4.6\%}_{-4.5\%}|_{\text{PDFs}}\ [70], \tag{5.2}$$

taking a k-factor of 1.07 [38] into account. This cross section value is valid for the simulated centre-of-mass energy of $\sqrt{s} = 10\,\text{TeV}$ and is reduced by 55 % with respect to the LHC design centre-of-mass energy of $\sqrt{s} = 14\,\text{TeV}$, but about 2.5 times higher compared to the current centre-of-mass energy of $\sqrt{s} = 7\,\text{TeV}$.

Since all $t\bar{t}$-events with at least one lepton in the final state have been generated inclusively and share the same run number (105200), no pure Monte Carlo sample for the signal processes exists. In order to separate the $t\bar{t}$-decay channels, a filter on the generated decay products is applied. Furthermore, all $t\bar{t}$-events have been generated using the next-to-leading order event generator MC@NLO, which introduces negative event weights. As a consequence, each result in this analysis has been corrected with respect to the effective number of events.

5.1.2. Background Processes

The event signature of the signal processes can be **mimicked** by other physics processes with similar final states or **faked** by mis-reconstruction of physics objects. In addition, particles from ISR and FSR can play an important role. In order to give an estimate of the relevance and the size of these contributions, the following physics processes have been included into the Monte Carlo analysis:

Top Quark Pair Background

In principal, the **tau plus jets** decay channel ($t\bar{t} \to \tau\nu + \text{jets}$) can be interpreted as being a signal process. On the other hand, due to its very short life time of about $\tau_\tau \sim 3 \cdot 10^{-12}\,\text{s}$, τ-leptons can be reconstructed only indirectly from their manifold leptonic and hadronic decay channels.

Since the event selection of this analysis is optimized to trigger on isolated electrons or muons, the $\tau + \text{jets}$ decay channel is interpreted as a background process in this analysis. Obviously, in the case of a τ-decay into an isolated enough lighter lepton, this process mimics perfectly the signal signature.

The **di-lepton** final state ($t\bar{t} \to l\nu l\nu$) can fake the signal process through its large E_T^{miss} and if one of the leptons is not detected or mis-reconstructed as a jet. Due to its lower jet multiplicity (two b-jets only), additional light quarks and gluons from ISR and FSR are required.

The **all hadronic** final state ($t\bar{t} \to b\bar{b}q\bar{q}q\bar{q}$) fulfils the high jet multiplicity criteria, but has in general no isolated lepton nor large enough E_T^{miss}. Nevertheless, a lepton can be faked by either mis-reconstruction of electrons from light quark jets or an isolated muon from B-meson decays (b-jets) which would also result in a larger E_T^{miss} from the neutrino.

Single Top Quark Production

A second way to observe real top quark decays occurs from electroweak single top quark production (cf. Chapter 1). The signal process can be faked in both, the s- and t-channel, if the top quark decays leptonically, while the required jet multiplicity arises from ISR and FSR. Even more likely to mimic the signal is the Wt-channel, due to the existence of two real W-bosons. Different to top quark pair events, single top production is generated using the `AcerMC` [71] event generator, where only leading order matrix elements are taken into account. The cross section is then scaled to its NLO value considering a k-factor of about k = 0.98 [38].

W-Boson Production plus Jets

The most prominent physics background arises from $W(l\nu)$ + jets events, where the W-boson decays leptonically. If the jet multiplicity (either from additional produced partons or from ISR/FSR) is large enough, this process shows the exact same event signature as the signal process. Furthermore, its cross section can be very large, thus a significant contribution even after event selection is expected. All $W(l\nu)$ + jets events are generated using the `Alpgen` [62] Monte Carlo generator plus a cross section NLO scaling of k = 1.22 [38]. They are subdivided with respect to the lepton flavour of the W-boson decay and the number of additional produced partons (up to five partons). In addition, all processes where two of the additional partons are b-quarks ($W(l\nu)$ + bb + jets) are included.

Z-Boson Production plus Jets

The signal process can be also mimicked by Z-boson events with associated jet production Z(ll) + jets if one of the two leptons from the Z-boson decay is mis-identified. The required E_T^{miss} can arise from jet energy mis-calibration. This event class has been also generated using the `Alpgen` Monte Carlo generator (plus NLO scaling with k = 1.22 [38]), subdivided with respect to the lepton flavour and the number of additional produced partons.

Di-Boson Production

Events with two bosons in the final state (WW, ZZ or WZ) can also mimic the signal process, in particular if one of the two bosons decays leptonically and the other one hadronically. The samples are generated using the `Alpgen` MC generator plus cross section scaling of k = 1.81 [38]. Additional jets to satisfy the required jet multiplicity occur only from ISR and FSR.

QCD Multi Jet Production

QCD multi jet events appear from pure non-resonant production of partons via QCD processes. It is by far the background process with the largest cross section. An isolated lepton as well as large $E_{\mathrm{T}}^{\mathrm{miss}}$ occur either from mis-reconstruction or from events with two b-jets. The event generation of the QCD background is performed with the `Alpgen` Monte Carlo generation which allows for full evaluation of up to $2 \to 6$ processes at LO matrix element level.

The cross section of the various QCD multi jet sub-processes varies about several orders of magnitude. In order to account for this, a p_T-slicing similar to the `Pythia` samples has been chosen for the sample production. In the `Alpgen` case, the reference is the leading truth particle jet, obtained using a simple cone-like jet reconstruction algorithm. The p_T-boundaries for the resulting JX samples are described in Table A.1. The samples are further subdivided with respect to the number n of produced partons ($2 \to$ n) and if the $\mathrm{b\bar{b}}$-pair has been produced at the matrix element level or via gluon splitting in the parton shower.

Due to the high cross section of QCD events, only a fraction of the necessary number of events could be simulated with full detector response. In order to get a reasonable estimation, all JX samples are produced with an integrated luminosity of about $\mathscr{L} \sim 10\,\mathrm{pb}^{-1}$. In case of the J2 and J3 samples, this number refers to events after the application of an additional truth jet filter, which requires three jets with $p_T > 35\,\mathrm{GeV}$ plus one jet with $p_T > 17\,\mathrm{GeV}$. The filter application improves the cross section of the J2 and J3 samples significantly and would reject all events of the J0 and J1 samples. For practical reasons, all samples beyond J4 are combined to one J5+ sample.

An overview of all physics processes taken into account in this top quark mass analysis can be found in Table 5.1.

A general limitation is the fact that all Monte Carlo samples have been produced neglecting contributions from the underlying event, i.e. multiple parton interactions from the same hadron of the hard scattering process, pile-up from additional scattering of other hadrons in the same bunch crossing, beam remnant and associated ISR/FSR. An analysis of these effects is an open issue addressed to future studies.

Sample	Physics Processes	ME Generator	k-factor
	$t\bar{t}$-Signal		
Electron plus Jets	$pp \to t\bar{t} \to b\bar{b}\,W(\to e\nu)\,W(\to q\bar{q})$	MC@NLO	1.07
Muon plus Jets	$pp \to t\bar{t} \to b\bar{b}\,W(\to \mu\nu)\,W(\to q\bar{q})$	MC@NLO	1.07
	$t\bar{t}$-Background		
Tau plus Jets	$pp \to t\bar{t} \to b\bar{b}\,W(\to \tau\nu)\,W(\to q\bar{q})$	MC@NLO	1.07
Di-Lepton	$pp \to t\bar{t} \to b\bar{b}\,W(\to l\nu)\,W(\to l\nu)$	MC@NLO	1.07
All Hadronic	$pp \to t\bar{t} \to b\bar{b}\,W(\to q\bar{q})\,W(\to q\bar{q})$	MC@NLO	1.07
	Other Background Processes		
Single Top	$pp \to (q, b, W)t$	AcerMC	0.99
W plus Jets	$pp \to W(\to l\nu) + (0-5)p$	Alpgen	1.22
Z plus Jets	$pp \to Z(\to ll) + (0-5)p$	Alpgen	1.22
Di-Boson	$pp \to WW, WZ, ZZ$	Alpgen	1.81
QCD Multi Jet	$pp \to (2-6)p$	Alpgen	–

Table 5.1.: Monte Carlo generated signal and background samples including k-factors [38].

5.2. Event Reconstruction – Reconstruction of the Top Quark Decay Products

With the exception of neutrinos, all top quark decay products are supposed to be detected by ATLAS detector. While electrons and muons leave a direct signal in the detector, quarks and gluons are only measured indirectly through their particle shower as described in Chapter 3. In order to reconstruct and calibrate the properties of all physics objects, standard algorithms within the ATLAS software framework `Athena` are used.

5.2.1. Electrons

Electrons are reconstructed around a seed cluster in the electro-magnetic calorimeter with an associated track in the inner detector. The `egamma` algorithm used requires medium cuts on the track-to-cluster matching and the calorimeter-energy to track-momentum ratio. In particular, the following ATLAS specific settings are used:

- `ElectronAODCollection`,
- `AuthorElectron`,
- `ElectronMedium`,

which are described in detail in [40]. The reconstruction efficiency for electrons in $t\bar{t}$-events with a transverse momentum above 20 GeV is expected to be about 67 % with a purity of about 97 % and a fake rate of less than 0.01 % [40].

5.2.2. Muons

Combined information from the muon spectrometer and the inner detector allows the reconstruction of muons with a high momentum resolution. The `StacoMuon` algorithm combines inner detector tracks and muon chamber hits, accounting for multiple scattering and energy loss in the calorimeter system. This list of muon candidates is called:

- `StacoMuonCollection` [40].

The reconstruction efficiency of muons in $t\bar{t}$-events with a transverse momentum above 20 GeV is expected to be about 88 % with a fake rate of about 0.1 % [40].

5.2.3. Jets

The reconstruction and energy calibration of calorimeter jets has been already discussed in detail in Chapter 3. The jets used in the following are reconstructed from local hadron calibrated topological clusters in the calorimeter using the anti-kt algorithm with a cut parameter value set to R = 0.4. Finally, the jet level corrections described in Chapter 4 are applied. The collections involved are:

- `CaloCalTopoCluster` [40]
- `AntiKt4LCTopoJets` plus Jet Level Corrections (cf. Chapter 4)

In order to select only jets initiated by hadrons, energy from single electrons is removed. The method used for this electron-overlap removal is to veto the full jet if it is close in ΔR to an electron which contributes significantly to the jet energy. In particular, a jet is rejected if:

- $\Delta R(jet, el) < 0.2$ and $E_{el}/E_{jet} > 0.5$

5.2.4. Neutrino Reconstruction from Missing Transverse Energy

Missing transverse energy ($E_{\mathrm{T}}^{\mathrm{miss}}$) is a crucial event variable for many physics analyses. It is defined to be the vector balancing in the transverse plane the component-by-component sum of all energy loss in the detector. In this analysis the sub-contributions taken into account are [40]:

- `MET_LocHadTopoObj`, which summarises the $E_{\mathrm{T}}^{\mathrm{miss}}$ contribution from all calorimeter cells, energy corrected with the local hadron calibration scheme,
- and `MET_MuonBoy`, an $E_{\mathrm{T}}^{\mathrm{miss}}$ contribution calculated from the muon momenta.

Since jet level corrections have been applied to the jets, the $E_{\mathrm{T}}^{\mathrm{miss}}$-vector has to be corrected for those as well. The final $E_{\mathrm{T}}^{\mathrm{miss}}$ is calculated by:

$$E_{\mathrm{x}}^{\mathrm{miss}} = E_{\mathrm{x}}^{\mathrm{miss}}(\texttt{LocHadTopoObj}) + E_{\mathrm{x}}^{\mathrm{miss}}(\texttt{MuonBoy}) - E_{\mathrm{x}}(\text{jet level corrections}) \quad (5.3)$$

$$E_{\mathrm{y}}^{\mathrm{miss}} = E_{\mathrm{y}}^{\mathrm{miss}}(\texttt{LocHadTopoObj}) + E_{\mathrm{y}}^{\mathrm{miss}}(\texttt{MuonBoy}) - E_{\mathrm{y}}(\text{jet level corrections}) \quad (5.4)$$

In events with at least one non-detected neutrino, the $E_{\mathrm{T}}^{\mathrm{miss}}$ is expected to be large. Assuming that all missing transverse energy belongs to the non-detected neutrino, $E_{\mathrm{T}}^{\mathrm{miss}}$ can be interpreted as the transverse energy of one missing neutrino, E_{T}^{ν}. Since the z-component E_{z}^{ν} remains undefined its value is set to zero in this analysis, keeping in mind that this degrades all longitudinal properties including the mass.

5.3. Event Selection – Study of Background from other Physics Processes

The goal of the event selection is to select $\mathrm{t\bar{t}}$-candidate events from the signal processes and to reject events from other physics processes (physics background). A loose pre-filter is already applied through the online trigger system while a refined selection is obtained using offline cuts on properties of the reconstructed physics objects.

5.3.1. Online Trigger Selection

Due to the high pp-collision rate at the LHC it is technically impossible to record the entire set of events. The online trigger system of the ATLAS detector (cf. Chapter 2) is set up to select events fulfilling at least some minimal criteria. Only if an event passes through all three levels of the trigger system it is added to a so called trigger stream, depending on the selection criteria. In order to select $\mathrm{t\bar{t}}$-candidate events of the **lepton plus jets** decay channel, set-ups to trigger on leptons with large transverse momentum are chosen to efficiently select signal events and reject background [40].

The lepton trigger menus considered in this analysis are:

- `EF_e10_medium` for the electron channel, taking all events with at least one electron of $p_T^{\mathrm{el}} > 10\,\mathrm{GeV}$ and medium isolation,
- and `EF_mu10` for the muon channel, taking events with at least one muon of $p_T^{\mu} > 10\,\mathrm{GeV}$.

Both trigger menus are not pre-scaled and chosen to be loose compared to the offline selection cuts. This leads to a reasonable data-taking efficiency of about 81.2 % for the electron channel and 77.2 % for the muon channel, respectively.

Nevertheless there are also events rejected which would pass the offline event selection. The trigger efficiency quantifies this effect and is defined as the ratio of the number of events after offline selection, with and without taking the trigger selection into account. It is about 97.7 % for the electron channel and only 88.2 % for the muon channel. The main reason for this is the limited coverage and efficiency of the trigger chambers of the muon system [40].

5.3.2. Offline Event Selection

After passing the online trigger selection, the events of the ATLAS trigger streams are fully reconstructed using refined offline reconstruction algorithms as described in the previous section. In order to further reject events from physics background processes, an optimised set of stricter cuts are applied to the properties of the physics objects.

Basic Selection

Since the lepton plus jets decay channel of $t\bar{t}$-events is also promising for cross section measurements with early ATLAS data, previous studies based on Monte Carlo have been already performed [40]. The set of cuts which was found to be optimal in these studies is taken as a basis for this analysis too. The idea is to follow the event signature of the signal processes and to require some quality cuts in addition. The first cut is the **lepton cut**, where exactly one isolated lepton is requested. It is refining the trigger selection by applying stricter cuts on the four-vector properties and the isolation. Furthermore, an overlap removal with jets is applied in order to exclude double counting of detector signal. In case of an electron, a transverse momentum of at least $p_T^{el} > 25\,\text{GeV}$ is requested. In order to ensure small uncertainties for the electron reconstruction, only electrons within $|\eta^{el}| < 2.47$ are considered. Furthermore, measurements from the gap regions between the barrel and endcap calorimeters are excluded by rejecting electrons between $1.37 < |\eta| < 1.52$. Finally, electrons within hadronic showers must be excluded through an isolation cut. Here, the transverse energy within a ΔR-cone of $\Delta R < 0.2$ around the axis of the electron is calculated and requested to be smaller than $E_{T,Cone20}^{el} = 6\,\text{GeV}$.

If the lepton is a muon, the minimal transverse momentum cut is raised to $p_T^{\mu} > 20\,\text{GeV}$. Only muons within $|\eta^{\mu}| < 2.5$ are taken and the isolation cut is the same as in the electron case, $E_{T,Cone20}^{\mu} < 6\,\text{GeV}$. In order to ensure that the muon comes from the W-boson decay and not from semi-leptonic b-quark decays, muons are generally rejected if they overlap with calorimeter jets within a ΔR-cone of $\Delta R < 0.3$ around the muon axis.

The second important cut is the **jet cut** where at least four calorimeter jets with large transverse momentum are required. Earlier studies show that at least three jets with a transverse momentum of $p_T^{jet} > 40\,\text{GeV}$ plus one jet with at least $p_T^{jet} > 20\,\text{GeV}$ must be requested [40].

According to these studies, the p_T-cut of the 4th jet allows for further purification of the event sample. In order to ensure the quality of the jet reconstruction, only calorimeter regions within $\eta < 2.5$ are taken into account. A double counting of calorimeter signal is avoided by rejecting jets if they overlap with an electron within $\Delta R < 0.2$. An upper cut on the number of "good" jets is not taken into account to allow also jets from ISR and FSR.

Finally, the event signature requires a neutrino with large transverse momentum. Since neutrinos cannot be detected with the ATLAS detector, one considers that the undetected neutrino is determined by the magnitude of missing transverse energy in the detector. Thus, the $\mathbf{E_T^{miss}}$ **cut** requires a value of $E_{\mathrm{T}}^{\mathrm{miss}} > 20\,\mathrm{GeV}$.

Selection Improvement

The basic event selection reduces the number of background events significantly. Nevertheless, the ratio between the number of signal events (S) and the number of background events (B) in this analysis is only S/B ~ 0.34 in the electron channel but S/B ~ 0.82 in the muon channel due to the higher rejection power of the muon cut. The deviation compared to previous studies [40, 72] are mainly due to different QCD background samples. Here, QCD multi-jet events simulated with `Alpgen` are preferred over the `Pythia` simulated di-jet samples, which suffer from low statistics.

In order to improve the signal to background ratio and thus further reject events from QCD background, a cut on the missing transverse energy significance is chosen. It is defined as

$$E_{\mathrm{T}}^{\mathrm{miss}}\text{-Significance} = E_{\mathrm{T}}^{\mathrm{miss}}/(0.5 \cdot \sqrt{\sum E_T}) \tag{5.5}$$

and is a measure of how significant the missing transverse energy is compared to the E_T-sum of the entire event. It is expected to be larger in case of a real neutrino from the W-boson decay, while it should be smaller in case of fake $E_{\mathrm{T}}^{\mathrm{miss}}$ from mis-calibration of pure jet events.

The distribution of the $E_{\mathrm{T}}^{\mathrm{miss}}$-Significance for the electron channel and the two major background processes are shown in Figure 5.1. Due to the leptonic decay of the W-boson, the distribution for signal events and events from W+jets background are similar and reach very large values. In contrast to this, the QCD multi-jet background shows a large peak at lower values which allows to separate signal events and QCD background. The cut chosen to select an event is $E_{\mathrm{T}}^{\mathrm{miss}}$-significance > 3.5 which rejects most of the QCD background but also a large fraction of signal events.

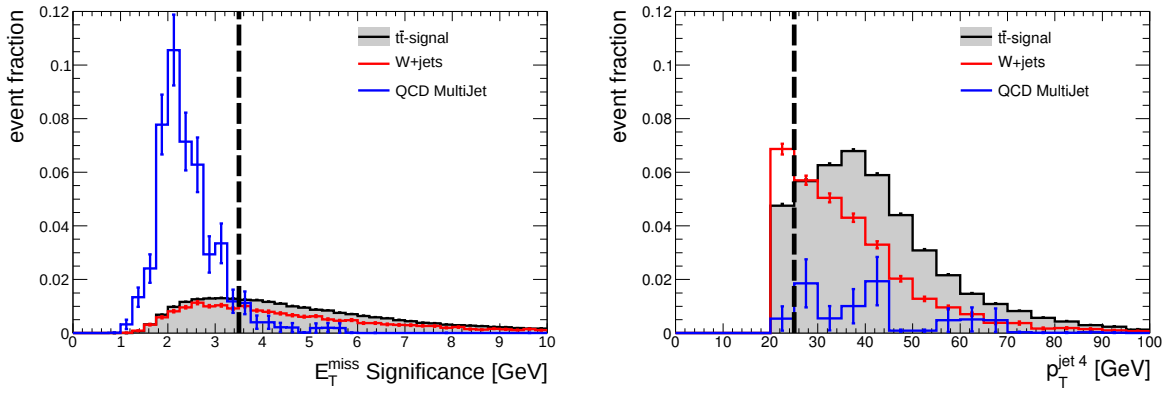

Figure 5.1.: Left: Distribution of the missing transverse energy significance after the basic event selection for the signal process (grey area) and the two major background processes: W+jets (red histogram) and QCD multi jet (blue histogram). The cut of $E_{T,miss}$-significance > 3.5 is indicated as black dashed line. Right: The distribution of the transverse momentum of the fourth jet (left) is shown after the basic selection plus the $E_{T,miss}$-significance cut. The improved cut of $p_T^{jet_4} > 25\,\text{GeV}$ is indicated as black dashed line.

The remaining major source of background events stem from W+jet processes. Since the signature of the W-boson decay is exactly the same as for the signal process, no differences are expected. On the other hand, the right hand plot in Figure 5.1 indicates that the p_T-spectrum of the fourth jet allows some discrimination, too. Thus, in order to reject more W+jet events, the p_T-cut was raised to $p_T^{jet_4} > 25\,\text{GeV}$.

5.3.3. Results

The final result of the online and offline event selection is a dataset with a signal to background ratio of S/B $\sim$ 0.85 for the electron channel and S/B $\sim$ 0.96 for the muon channel. This achievement allows for further studies including a top quark mass measurement. The step by step development for all processes is pictured for both signal channels in Figure 5.2 and numerically presented in the Tables 5.2 & 5.3.

Due to the hard selection cuts, the efficiency to select events from the signal processes is only 15.0 % for the electron channel and 14.6 % for the muon channel. On the other hand, the number of events from background processes are reduced by several orders of magnitude. In particular the lepton and $E_{\text{T}}^{\text{miss}}$-cuts reduce the dominant QCD multi-jet background to minor importance. The leading background process after event selection originates from W+jets processes which have an event signature closest to the lepton plus jets $\text{t}\bar{\text{t}}$-decay channel.

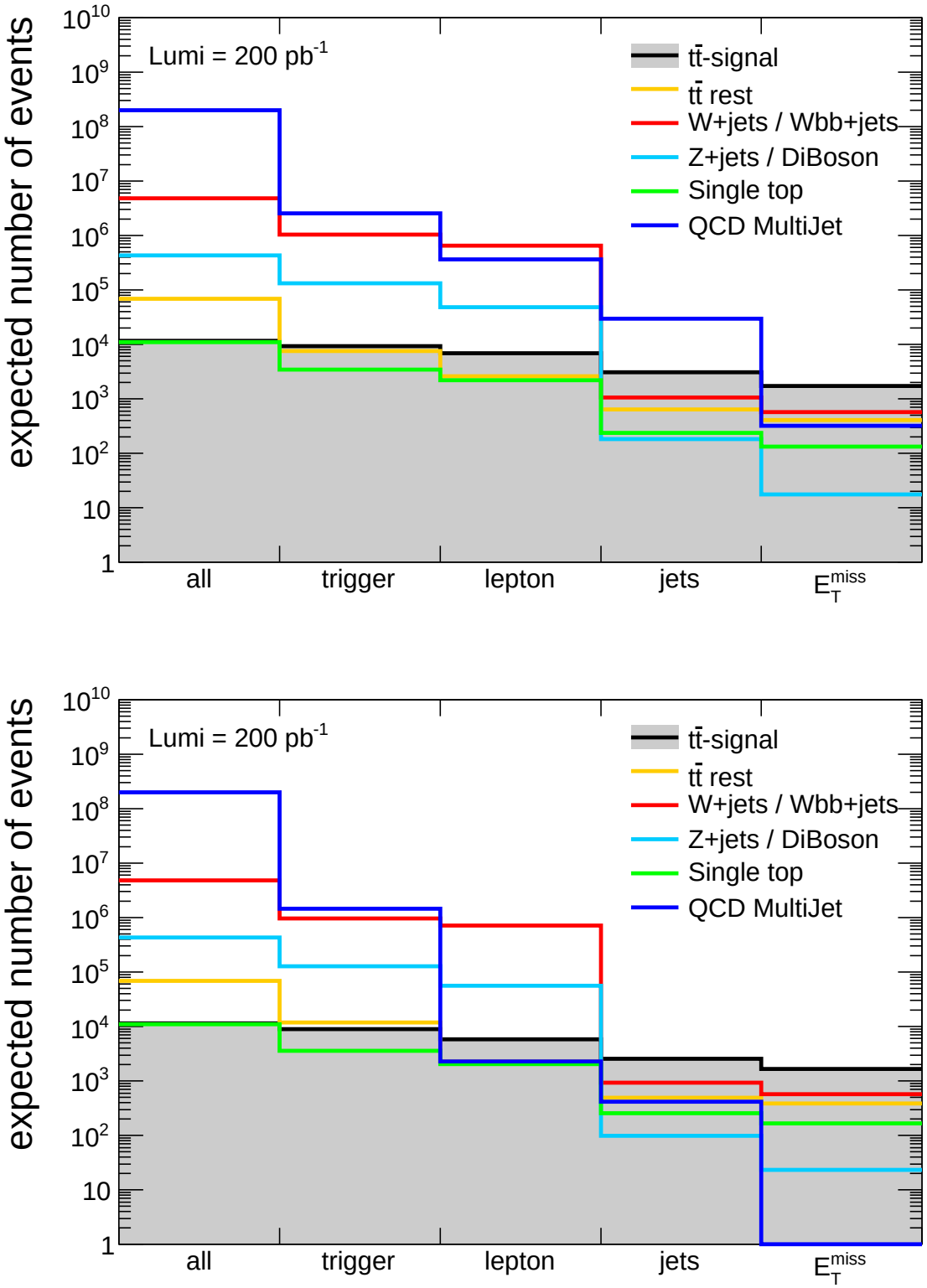

Figure 5.2.: Cut-flow diagram for the online and offline event selection in the electron channel (top) and the muon channel (bottom). The signal over background ratio is improved from S/B $\sim 10^{-5}$ to nearly S/B ~ 1 for both $t\bar{t}$-decay channels.

	Expected Number of Events / Sample						
	$t\bar{t}$-signal	$t\bar{t}$-rest	W+Jets	Z+Jets	DiBoson	Single Top	QCD
all events	11565	68385	$9.70{\cdot}10^6$	864893	3910	10971	$2.01{\cdot}10^8$
trigger selection	9387	7617	$2.07{\cdot}10^6$	263019	1682	3478	$2.54{\cdot}10^6$
after lepton cut	6901	2608	$1.29{\cdot}10^6$	96075	955	2198	364153
after jet cut	3072	637	2128	353	12	237	29778
after $E_{\mathrm{T}}^{\mathrm{miss}}$ cut	1739	407	1149	29	6	132	321
Combined	1739	2044					

Table 5.2.: Expected number of events after each selection cut for the electron channel and all relevant background processes. The analysis assumes an integrated luminosity of $\mathscr{L} = 200\,\mathrm{pb}^{-1}$.

	Expected Number of Events / Sample						
	$t\bar{t}$-signal	$t\bar{t}$-rest	W+Jets	Z+Jets	DiBoson	Single Top	QCD
all events	11541	68409	$9.70{\cdot}10^6$	864893	3910	10971	$2.01{\cdot}10^8$
trigger selection	8909	11809	$1.95{\cdot}10^6$	253837	1665	3600	$1.45{\cdot}10^6$
after lepton cut	5882	2299	$1.43{\cdot}10^6$	111310	924	2062	2268
after jet cut	2594	493	1876	188	10	263	473
after $E_{\mathrm{T}}^{\mathrm{miss}}$ cut	1689	388	1150	42	5	172	0
Combined	1689	1757					

Table 5.3.: Expected number of events after each selection cut for the muon channel and all relevant background processes. The analysis assumes an integrated luminosity of $\mathscr{L} = 200\,\mathrm{pb}^{-1}$.

One important difference between the electron and muon channel is the fact that muons do not leave a relevant signal within the calorimeter system. Instead they are measured using the dedicated muon chamber system. Due to this, it is much more unlikely to fake a high-p_{T} muon in a multi jet environment compared to an electron. This results into the significant reduction of the QCD multi jet background which is observed after the muon cut (cf. Figure 5.2 below).

5.4. Top Quark Reconstruction – Study of Combinatorial Background

After the final selection of $t\bar{t}$-candidate events, the top quark is reconstructed from its decay products. Due to the undetected neutrino on the leptonic side, only the four-vector of the hadronically decaying top quark can be fully reconstructed from calorimeter jets. The challenge is here to select the correct three out of at least four jets in the event which belong to the hadronic side of the $t\bar{t}$-decay. Wrong combinations can bias the top quark mass measurement and are thus referred to as **combinatorial background**.

Already in events with exactly four jets there are $\binom{4}{3} = 4$ possibilities to select the correct jet triplet. Since no upper cut is set on the number of jets per event, also cases with $\binom{5}{3} = 10$ and more possibilities exist. In addition, an explicit reconstruction of the hadronic W-boson would further increase the number of possible combinations.

In the following section, three different reconstruction methods are studied and compared to a random selection of the jet triplet. Several levels of abstraction are analysed from parton generator level with full event information to the level of reconstructed calorimeter jets. The goal is to find the reconstruction method which provides the largest fraction of correct combinations over combinatorial background.

5.4.1. Top Quark Reconstruction Methods

In general one distinguishes between two classes of top quark reconstruction methods in semi-leptonic $t\bar{t}$-events. The first class provides methods which only reconstruct the hadronic branch of the $t\bar{t}$-decay while the second class requires a full event reconstruction in order to exploit information provided by the leptonic branch.

The first three reconstruction methods are selecting three calorimeter jets. Each possible combination has only a hadronic top quark candidate:

a) **Random** – random selection of three calorimeter jets as a reference.

b) **Max $\mathbf{p_T}$** [40] – selection of the jet triplet whose combined four-vector has the largest transverse momentum compared to all other possible combinations.

c) **Min $\mathbf{\Delta R}$** – selection of the jet triplet where the sum of the three pair-wise jet axis distances in ΔR-space is minimal compared to all other possible combinations.

In case of a full event reconstruction, also lepton and neutrino candidates are considered. Each combination has a hadronic and a leptonic top quark candidate:

d) **Min $\mathbf{\Delta M}$** – selection of the $t\bar{t}$-candidate with the smallest mass difference between the leptonic and hadronic side.

In the following, all four top quark reconstruction methods are compared with the goal to minimise the combinatorial background.

5.4.2. Parton Level Studies

The parton level studies are performed on the generator output where the parton four-vectors of all $t\bar{t}$-decay products are well known. This allows for analysing the initial state of the $t\bar{t}$-decay, excluding the limitations of the hadronisation process, the smearing of the detector signal and the inefficiencies of the jet reconstruction and energy calibration. Above all, the correct assignment of the $t\bar{t}$-decay products is well known and can be taken as a reference. In order to find the correct combinations of partons, the four-vectors of the four quarks $(b_{lep}, b_{had}, q_0, q_1)$ are taken as an input to the different reconstruction methods. In case of the Min-ΔM method, also the four-vectors of the lepton and the neutrino are taken into account. Since the p_z^ν-component of the neutrino four-vector is not even indirectly reconstructible with the ATLAS detector, it is set to $p_z^\nu = 0$ for this study. Out of the four possible quark combinations only the triplet (b_{had}, q_0, q_1) reconstructs the hadronically decaying top quark correctly. The result of the parton level analysis is presented on the left side of Figure 5.3. The first bin of the histogram shows the fraction of correct combinations with respect to all lepton plus jets events. It is shown, that the Min-ΔM method selects with $\sim 60\,\%$ the largest fraction of correct combinations, followed by the equally successful Max-p_T and Min-ΔR methods with $\sim 36\,\%$. The reference method using a random selection shows no preferences and selects each of the four possible combinations with $\sim 25\,\%$.

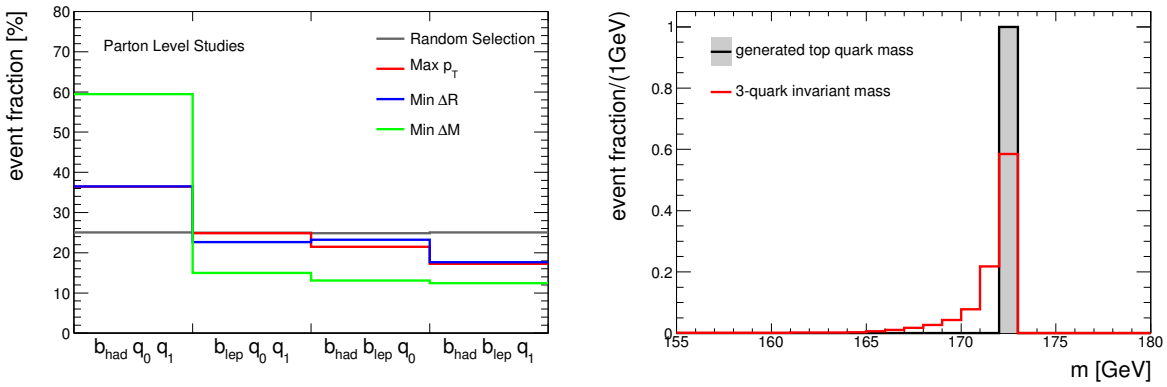

Figure 5.3.: Left: Event fraction of the four possible quark combinations at parton level. The correct combination (b_{had}, q_0, q_1) in the first bin is selected with $\sim 60\,\%$ by the Min-ΔM method, with $\sim 36\,\%$ by the Max-p_T and Min-ΔR methods and with $\sim 25\,\%$ by the random selection. Right: Invariant mass of the top quark decay products neglecting the gluons from the ISR.

Even if the Min-ΔM method selects more correct combinations than all others, it suffers from the imperfect mass reconstruction of the leptonic decay branch. The main reason is the ignorance of the p_z^ν-component of the neutrino four-vector. A second effect arises from initial state radiation where gluons carry some energy fraction of the top quark. This leads to a lower top mass if those gluons are neglected in the top quark reconstruction. Figure 5.3 shows the invariant mass of the top quark decay products neglecting the gluons from the ISR. Only $\sim 60\,\%$ of the events reconstruct the generated top quark mass of $m_t = 172.5\,\text{GeV}$ perfectly.

The other two methods, Max-p_T and Min-ΔR, are based on kinematic properties and thus a 100 % efficiency is not expected. Nevertheless their discriminative power is shown which underlines the assumption, that the system of hadronic top quark decay products has often the largest transverse momentum or is closest to each other compared to the rest of the event.

5.4.3. Jet Level Studies including Parton-to-Jet Matching

The next studies are performed at jet level, first using truth particle jets and afterwards taking calorimeter jets. In contrast to previous studies at parton level, both cases include effects from hadronisation processes as well as from inefficiencies of the jet reconstruction and energy determination. In the second case of calorimeter jets also detector effects like acceptance and signal smearing are included.

The specific characteristic of the following jet level studies is the parton-to-jet matching. Here, only a sub-sample of events is considered where a complete set of jets could be matched to their partonic $t\bar{t}$-decay products within a distance of $\Delta R < 0.1$. The matching criteria leads to a preferred selection of "well reconstructed" events which results into a bias for the efficiency calculation. On the other hand, one keeps the knowledge of the correct assignment of the decay products and thus the reference for this study.

In analogue to the parton level studies, the three previously defined top quark reconstruction methods are compared to each other plus a random selection of jets as a reference. In case of the Min-ΔM-method, the electron and neutrino are chosen according to the considered jet collection. For truth particle jets, a truth lepton is taken into account while the neutrino is reconstructed from the truth missing transverse energy four-vector, neglecting the p_z^ν-component. In case of calorimeter jets, the lepton and neutrino are consistently taken from the reconstructed collections as described in Section 5.2.

The results of both jet level studies are summarised in Figure 5.4 where the method efficiencies for truth particle jets are presented on the left and the ones for calorimeter jets on the right side. In general, the differences between the three reconstruction methods are small compared to the parton level studies. For truth particle jets the Min-ΔM method selects the correct combination in 50 %, the Min-ΔR in 48 % and the Max-p_T in 45 % of all cases. Similar results are found for calorimeter jets which shows that a good jet reconstruction and energy calibration minimises biases from detector effects.

Compared to the parton level studies, the Min-ΔR and the Max-p_T methods show an improved efficiency. This can be explained by the kinematic cuts for jets (cf. Section 5.2) and the bias from the "well reconstructed" sub-sample. In contrast to this has the Min-ΔM method a lower efficiency. This shows that the uncertainties on the jet four-vector reconstruction, in particular on the direction and energy, have a significant effect on the top quark mass reconstruction.

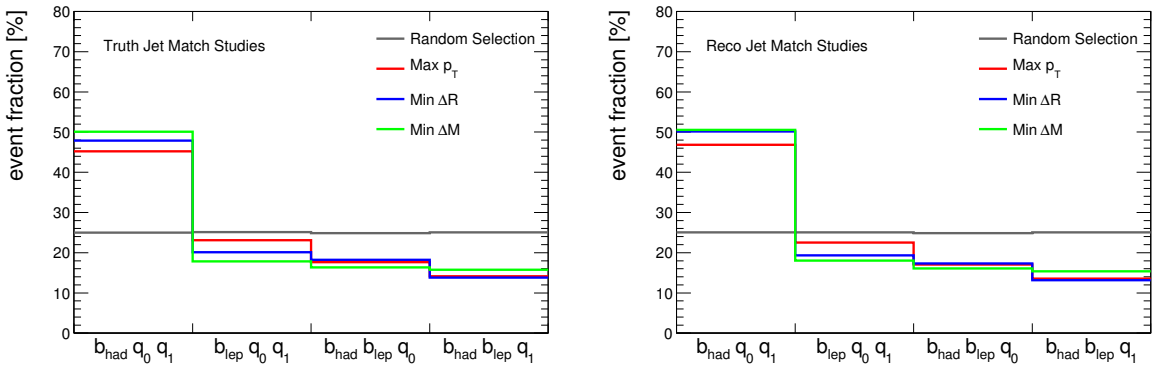

Figure 5.4.: Event fraction of the four possible quark combinations at jet level including parton-to-jet matching. For truth particle jets (left) the correct combination (b_{had}, q_0, q_1) in the first bin is selected with 50 % by the Min-ΔM method, followed by the Min-ΔR method (48 %) and the Max-p_T method (45 %). Similar results are found for reconstructed calorimeter jets (right).

5.4.4. Jet Level Studies without Parton-to-Jet Matching

In the last step of the combinatorial background studies, the three top quark reconstruction methods are tested on a realistic sample of lepton plus jets $t\bar{t}$-events after applying the event selection described in Section 5.3. This scenario is similar to the calorimeter jets case in the previous section without the bias of the parton-to-jet matching. As a consequence, the correct combination of jets remains unknown and a new definition for combinatorial background needs to be chosen.

In the following, a correct combination is found if the combined jet four-vector overlaps with the four-vector of the generated top quark within a distance of $\Delta R = 0.1$ at maximum. This is a very strict in order to ensure the quality of the sub-sample of correct combinations. Nevertheless, one cannot distinguish any longer between the selection of a wrong jet combination and the general mis-reconstruction of the entire event. Thus the number of correct combinations found is expected to be generally lower compared to the previous studies.

In addition to the question if a certain combination is correct or not also the shape of the 3-jet invariant mass distribution of the combinatorial background is important for the quality of a mass measurement. A good separation of correct combinations and combinatorial background is expected to improve the uncertainty of a measurement.

The result of this analysis is presented in Figure 5.5. For each reconstruction method, the 3-jet invariant mass distribution of correct combinations (light grey) and combinatorial background (dark grey) are shown and compared to a random selection of jets. Furthermore, the sample purity, defined as the event fraction of correct combinations, is quoted.

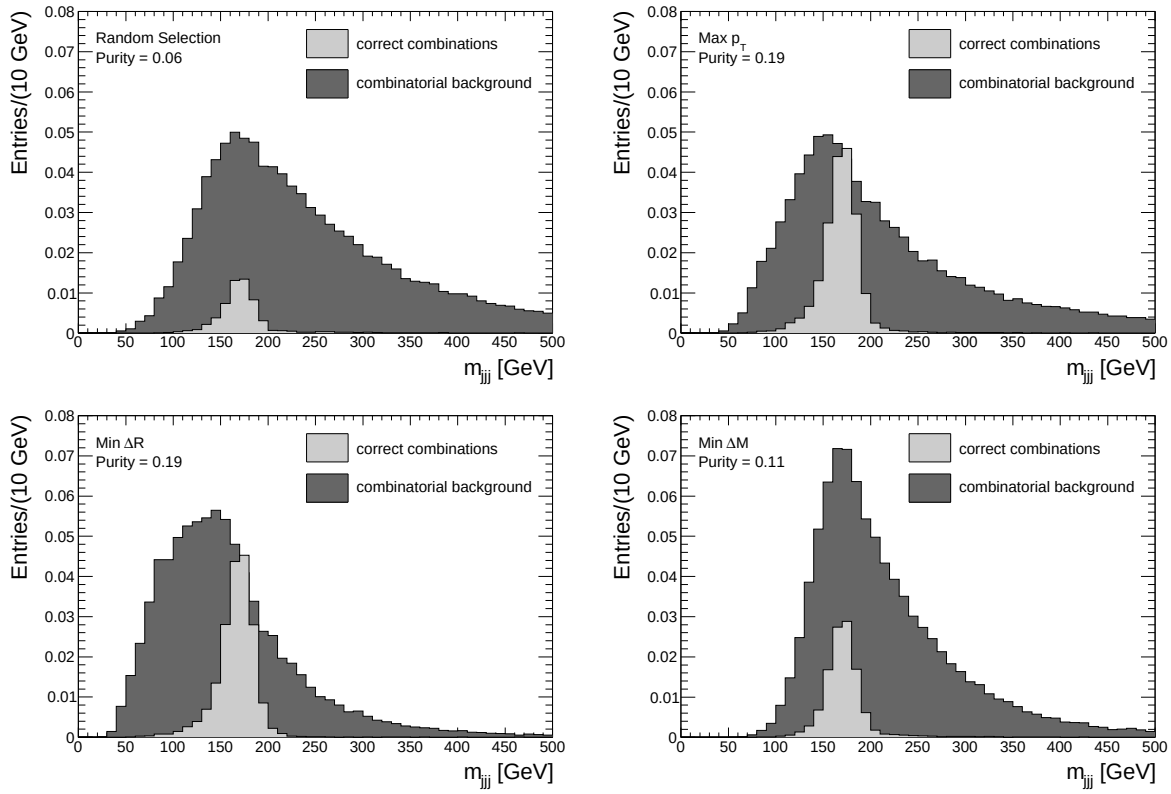

Figure 5.5.: Distribution of the 3-jet invariant mass for correct combinations (light grey) and combinatorial background (dark grey) on a realistic sample of $t\bar{t}$-candidate events. While the Max-p_T and Min-ΔR methods have a sample purity of 19 %, the Min-ΔM method has only 11 % which is not far from the Random Selection with 6 %. In case of the Max-p_T method, the combinatorial background shows a symmetric peak close to the position of the correct combinations while in case of the Min-ΔR method, the combinatorial background distribution is clearly asymmetric and shifted towards lower mass values.

Both methods, Max-p_T and Min-ΔR, show a reasonable sample purity of 19 % compared to 6 % for the random selection. This proves again that their kinematic assumptions have discriminative power but also that on about 80 % the methods don't succeed due to different event topologies or general mis-reconstruction. Even if both methods result into a similar sample purity, their 3-jet invariant mass distributions differ from each other. In case of the Max-p_T method, the combinatorial background shows a symmetric peak close to the position of the correct combinations while in case of the Min-ΔR method, the combinatorial background distribution is clearly asymmetric and shifted towards lower mass values.

Compared to the previous studies, the Min-ΔM method has a much lower efficiency with a sample purity of only 11 %. This shows, that different event topologies have a significant effect on this method in particular through the indirect reconstruction of the neutrino four-vector from missing transverse energy. Furthermore, the 3-jet invariant mass distribution of the combinatorial background peaks exactly at the position of the correct combinations and shows a tendency towards larger mass values, in particular compared to the Min-ΔR method.

5.4.5. Conclusion

In the previous section, the three reconstruction methods, Max-p_T, Min-ΔR and Min-ΔM have been studied on lepton plus jets $t\bar{t}$-events for different levels of Monte Carlo simulation. While at parton level the Min-ΔM shows the best performance, it looses its discriminative power at jet level. This is due to the indirect reconstruction of the neutrino four-vector from missing transverse energy and the wide range of event topologies including ISR and FSR. The Max-p_T and Min-ΔR methods show the best performance at jet level since they are based on kinematic properties only. Both methods are further investigated in the final top quark mass measurement in the next section.

5.5. Top Quark Mass Measurement with the Combined Fit Method

In this section, a complete top quark mass measurement is presented including an evaluation of the main systematic uncertainties. The measurement is performed using a χ^2-fit of the combined 3-jet invariant mass distribution for signal and background events. Except for a bias correction, the mean parameter of the signal distribution corresponds to the pole mass of the top quark (cf. Chapter 1). In order to evaluate systematic differences between the electron and muon channel as well as between the two reconstruction methods Max-p_T and Min-ΔR, the measurement is repeated for each combination of channel type and reconstruction method individually.

The basis for the following analysis is the output sample of Section 5.3 which is equivalent to an ATLAS dataset of $\mathscr{L} = 200\,\mathrm{pb}^{-1}$ at a centre-of-mass energy of $\sqrt{s} = 10\,\mathrm{TeV}$. The mass measurement presented here assumes neither b-tagging nor in-situ jet energy calibrations. In the following, all figures and results are exemplarily shown for the electron channel and both reconstruction methods. The results for the muon channel are summarised below in Section 5.5.4.

5.5.1. Invariant Mass Distribution

The key figure of the combined fit method is the 3-jet invariant mass which is reconstructed from the assumed decay products of the hadronic top quark decay. In other words, the four-vectors of the three jets selected by a chosen reconstruction method are combined and the mass of the resulting four-vector is taken. The distributions of the 3-jet invariant mass for both reconstruction methods are presented in Figure 5.6. Both plots include the signal process as well as all relevant physics background processes where the number of events per process is normalised to an integrated luminosity of $\mathscr{L} = 200\,\mathrm{pb}^{-1}$. The signal process is divided according to the matching criteria of Section 5.4.4 into correct combinations (light grey) and combinatorial background (dark grey).

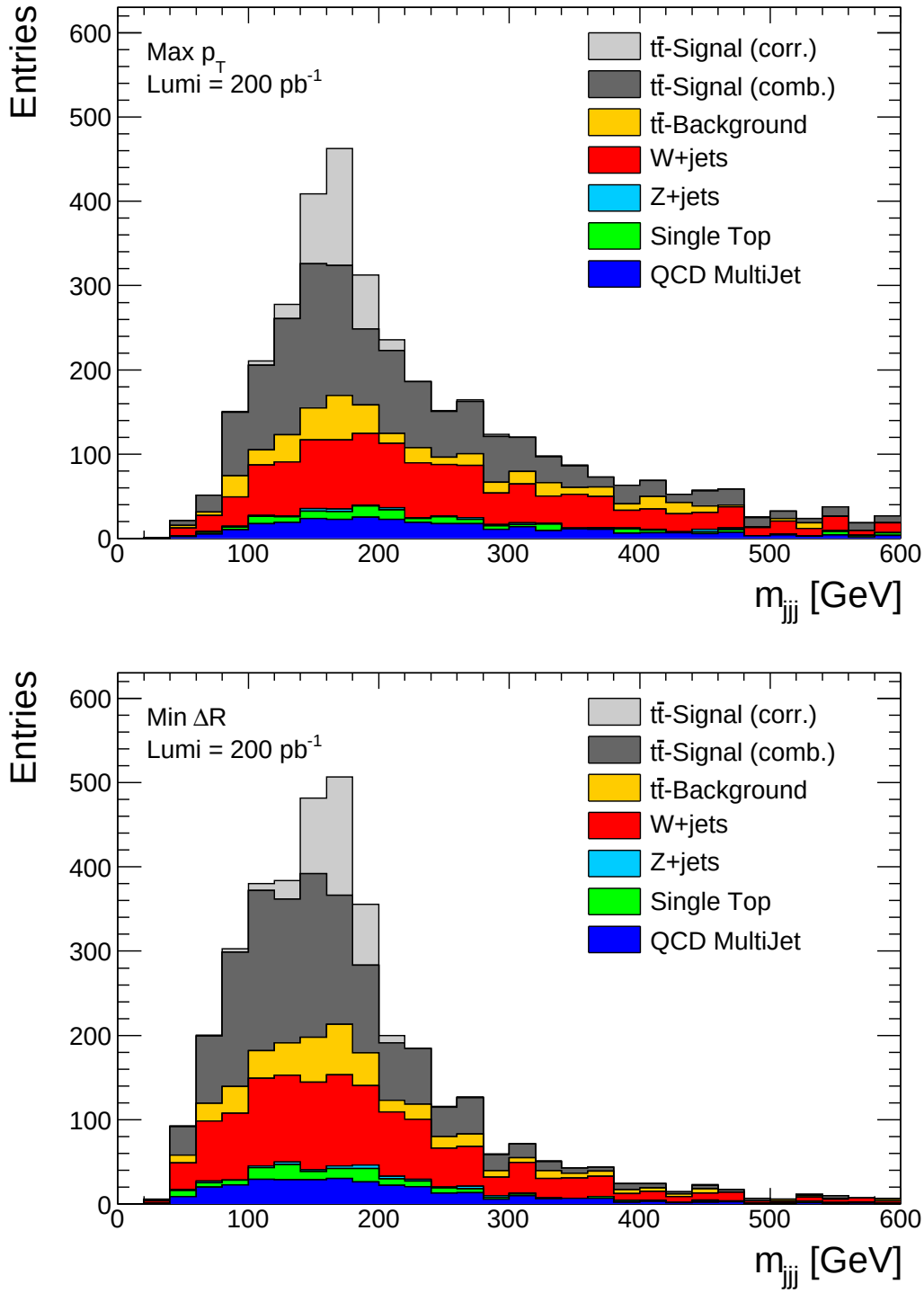

Figure 5.6.: Invariant mass distribution of the 3-jet combination selected by the Max-p_T (top) and Min-ΔR (bottom) reconstruction method for the electron channel. The signal events are indicated in grey and the background events in their respective colour code. The major source of physics background are events from W + jets processes and other $t\bar{t}$-decay channels. Both plots represent a typical pseudo-experiment with an integrated luminosity of $\mathscr{L} = 200\,\mathrm{pb}^{-1}$.

Due to the good statistics of the ATLAS Monte Carlo production, the events could be selected for each process randomly from a larger statistical sample. Only in case of the QCD processes a limited sample corresponding to an integrated luminosity of about $\mathscr{L} = 10\,\mathrm{pb}^{-1}$ was available due to the large cross section of these processes.

In order to avoid large shape fluctuations which come along with large scaling factors, the shape of the W + jets background is taken here and scaled according to the correct sample fraction for events from QCD processes. In order to account for the possible bias introduced by this choice, a large variation of the shape and normalisation is performed during the evaluation of systematic uncertainties.

For both reconstruction methods, all physics background processes show a similar behaviour. The background classes of Z + jets events and single top production are rather flat while the distributions of W + jets events and other $\mathrm{t\bar{t}}$-decay channels show a peak close to the peak position of the signal distribution.

5.5.2. Combined Fit of Signal and Background

In the following, the top quark mass is measured from the 3-jet invariant mass distribution using a χ^2-fit procedure and a combined parametrisation of the signal and background distributions. The resulting fit function $f^{\mathrm{fit}}_{\mathrm{comb}}(m_{jjj})$ is a convolution of the signal and background parametrisations

$$f^{\mathrm{fit}}_{\mathrm{comb}}(m_{jjj}) = f_{\mathrm{si}}(m_{jjj}) \otimes f_{\mathrm{bg}}(m_{jjj}) \tag{5.6}$$

which depends on the 3-jet invariant mass variable m_{jjj}. It must be constructed in a way that one of the fit parameters describes the most probable value of the m_{jjj} signal distribution.

Signal Shape Parametrisation

Assuming that any underlying distribution of the top quark decay (Breit-Wigner, gluon radiation) is covered by the detector resolution, the distribution of correctly combined signal events should follow a Gaussian. For this reason, the parametrisation is chosen to be

$$f_{\mathrm{si}}(m_{jjj}) = C_0 \cdot e^{-\frac{1}{2}\cdot\left(\frac{m_{jjj}-C_1}{C_2}\right)^2}, \tag{5.7}$$

where m_{jjj} is the 3-jet invariant mass variable and C_0 to C_2 are the free fit parameters. The mean of the Gaussian C_1 is equal to the most probable value of the signal event distribution and thus the parameter of interest in this analysis.

Background Shape Parametrisation

The shape of the background distribution can be parametrised by a linear combination of polynomials. In this analysis, Legendre polynomials are chosen which form a basis of orthogonal functions in the range $x \in [-1, 1]$ with respect to the condition

$$\int_{-1}^{+1} L_n(x) \cdot L_m(x) dx = \frac{2}{2n+1} \delta_{mn}. \tag{5.8}$$

Here, $L_n(x)$ represents a Legendre polynomial of the order n and δ_{mn} represents the Kronecker symbol. In particular, a linear combination of Legendre polynomials up to the 7th order is chosen to fit the combined background distribution including physics and combinatorial background

$$f_{bg}(x) = \sum_{n=0}^{6} C_{n+3} \cdot L_n(x). \tag{5.9}$$

In more detail, the first five orders of the Legendre polynomials are defined as

$$\begin{aligned}
L_0(x) &= 1\,, \\
L_1(x) &= x\,, \\
L_2(x) &= \tfrac{1}{2} \cdot \left(3x^2 - 1\right)\,, \\
L_3(x) &= \tfrac{1}{2} \cdot \left(5x^3 - 3x\right)\,, \\
L_4(x) &= \tfrac{1}{8} \cdot \left(35x^4 - 30x^2 + 3\right)\,, \\
L_5(x) &= \tfrac{1}{8} \cdot \left(63x^5 - 70x^3 + 15x\right)\,, \\
L_6(x) &= \tfrac{1}{16} \cdot \left(231x^6 - 315x^4 + 105x^2 - 5\right)\,.
\end{aligned} \tag{5.10}$$

The Legendre polynomials are defined with respect to the standard basis of monomials x^i with x $\in [-1, 1]$. This is important in order to minimise the correlations among each other and thus to achieve a good control on the fit convergence and the errors of the fit parameters C_3 to C_7.

In order to use the background fit function $f_{bg}(x)$ on the fit range $[m_{jjj}^{min}, m_{jjj}^{max}]$, the linear transformation $m_{jjj} \to x$ has to be applied. It is defined via

$$\begin{aligned}
x &= x_0 \cdot m_{jjj} + x_1, \\
x_0 &= 2/(m_{jjj}^{max} - m_{jjj}^{min}), \\
x_1 &= 1 - x_0 \cdot m_{jjj}^{max}.
\end{aligned} \tag{5.11}$$

The fit range for this measurement is chosen to be $[m_{jjj}^{min}, m_{jjj}^{max}] = [50\,\text{GeV}, 400\,\text{GeV}]$ which ensures the minimisation of the impact of the distribution tails from both sides.

Fit Results

The parameters of the combined fit function are estimated using a χ^2-minimisation procedure [73]. The fit returns a complete set of parameters which correspond to the minimal χ^2-value. All fits in this analysis are performed individually on the invariant mass spectrum of the pseudo-experiments using the data analysis framework `ROOT` running the minimisation package `Minuit` [74].

The results of the combined fit for the electron channel are shown on the left side of the Figures 5.7 (Max-p_T) and 5.8 (Min-ΔR). The combined fit function is shown in black and fits the overall distribution. The individual sub-functions for signal and background are shown in blue and red, respectively.

For both reconstruction methods, the distributions for signal and combined background are well described by the fit functions. The parameter of interest, the mean value of the signal distribution, is estimated to be $m_{jjj} = 165.2 \pm 2.2\,\text{GeV}$ for the Max-p_T method and $m_{jjj} = 166.5 \pm 2.4\,\text{GeV}$ for the Min-ΔR method. Since the fit precision is limited by the size of the event sample, the fit uncertainty is quoted as the statistical uncertainty of this parameter value.

In order to evaluate the goodness of the signal description by the combined fit, a comparison to a separate Gaussian fit of the 3-jet invariant mass distribution for only correct combinations (light grey) is done. The result is shown on the right side of the Figures 5.7 (Max-p_T) and 5.8 (Min-ΔR), where the signal sub-function from the combined fit is the same as on the left side (blue line) and the result from a separate fit is displayed as a green line.

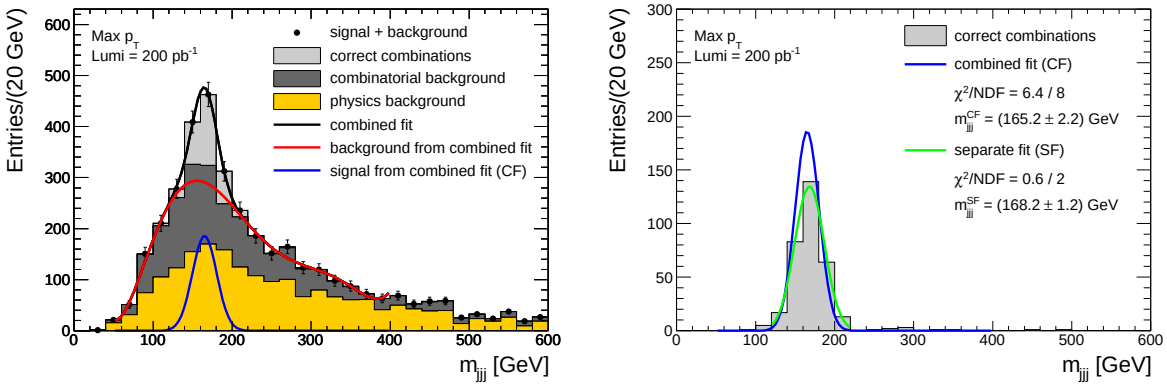

Figure 5.7.: Left: Distribution of the 3-jet invariant mass from one pseudo-experiment for $\mathscr{L} = 200\,\text{pb}^{-1}$ using the Max-p_T reconstruction method. Correct combinations are indicated in light grey, combinatorial background in dark grey and physics background in yellow. The combined fit function is shown as a black line, the individual sub-functions for signal and combined background as blue and red line respectively. Right: Comparison of the signal sub-function from the combined fit (blue line) and the result from a separate fit (green line) of the 3-jet invariant mass distribution for correct combinations only (light grey).

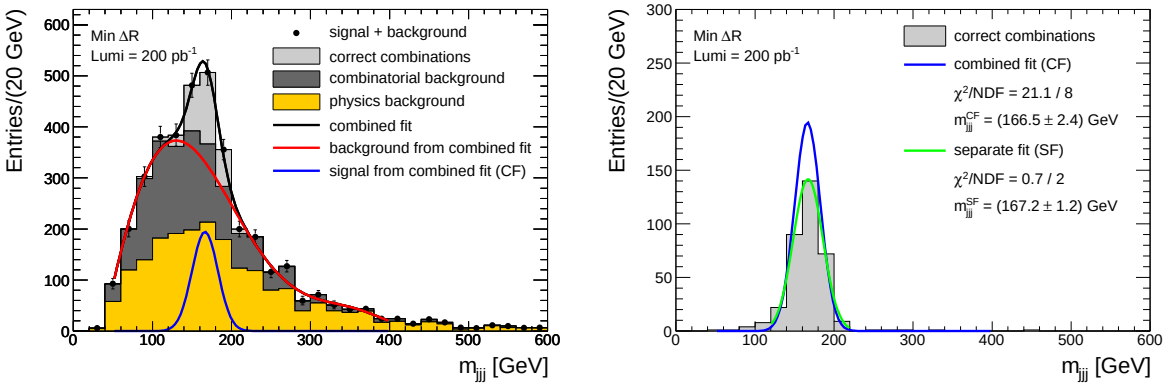

Figure 5.8.: Left: Distribution of the 3-jet invariant mass from one pseudo-experiment for $\mathscr{L} = 200\,\mathrm{pb}^{-1}$ using the Min-ΔR reconstruction method. Correct combinations are indicated in light grey, combinatorial background in dark grey and physics background in yellow. The combined fit function is shown as a black line, the individual sub-functions for signal and combined background as blue and red line respectively. Right: Comparison of the signal sub-function from the combined fit (blue line) and the result from a separate fit (green line) of the 3-jet invariant mass distribution for correct combinations only (light grey).

Both reconstruction methods show a very good agreement of the results from the combined and the separate fit which gives confidence into the reliability of the combined fit. While the Max-p_T-method has a difference of $\Delta m_{jjj} = |m_{jjj}^{CF} - m_{jjj}^{SF}| = 3.0\,\mathrm{GeV}$ between the two mean values, the difference is even smaller for the Min-ΔR-method with $\Delta m_{jjj} = 0.7\,\mathrm{GeV}$ respectively.

In general, the height of the signal peak from the combined fit is slightly larger compared to the histogram of correct combinations. This implies an underestimation of correct combinations in the signal sample and thus an overestimation of the combinatorial background. It improves by increasing the somewhat arbitrary cut parameter of the combinatorial background definition ($\Delta R = 0.1$). Nevertheless, any change of it has no effect on the combined fit result.

Also the agreement among the two different reconstruction methods is very good. The sets of selected combinations are to more than 50 % identical and the resulting mean values from both methods are very close to each other. This gives confidence into the assumption that possible biases from the reconstruction method itself are relatively small (cf. Section 5.6). One should keep in mind that the central values are derived from one possible pseudo-experiment without any bias correction and thus differ from the generated top quark mass value of $m_t^{gen} = 172.5\,\mathrm{GeV}$.

	Combined Fit (CF)		Separate Fit (SF)	
Recon. Method	$m_{jjj}^{CF} \pm \Delta m_{jjj}^{CF}$ [GeV]	χ^2/NDF	$m_{jjj}^{SF} \pm \Delta m_{jjj}^{SF}$ [GeV]	χ^2/NDF
Max-p_T	165.2 ± 2.2	6.4/8	168.2 ± 1.2	0.6/2
Min-ΔR	166.5 ± 2.4	21.1/8	167.2 ± 1.2	0.7/2

Table 5.4.: Numerical results of the combined and separate fit for the Max-p_T and Min-ΔR method in the electron channel including statistical uncertainties.

5.5.3. Systematic Uncertainties

Beyond statistical uncertainties due to the limited number of events, systematic uncertainties occur from the limited precision of the underlying simulation model or from the measurement resolution of the data reconstruction methods. In order to evaluate these systematic uncertainties, all relevant parameters of the simulation and reconstruction process are varied. The magnitude of the shift compared to the original result is a measure of the impact from the respective parameter. In the following, all key parameters are varied individually within $\pm 1\sigma$ with respect to the default measurement. Depending on the complexity of the case, the dataset was re-simulated and re-reconstructed before the 3-jet invariant mass was estimated using the combined fit procedure. The shift of the mean value of the Gaussian part is considered as the systematic uncertainty for this specific variation. In order to give a conservative estimation, the final systematic uncertainty quoted for each parameter is calculated as the maximum of the absolute shift of all variations of the respective parameter.

Jet Energy Scale

The largest effect on a mass measurement from hadronic final states with calorimeter jets is expected from jet energy determination. First of all, any variation of the jet energy scale effects directly the result of the 3-jet invariant mass calculation of the top quark candidate from individual jets. Furthermore, the event selection depends significantly on variables based on the transverse jet energy. This effects the number as well as the kind of selected events. In addition, the number of low energetic jets per event varies due to jet energy dependent selection cuts. This can result into significant differences for the outcome of all top quark reconstruction methods since a different jet triplet might be selected.

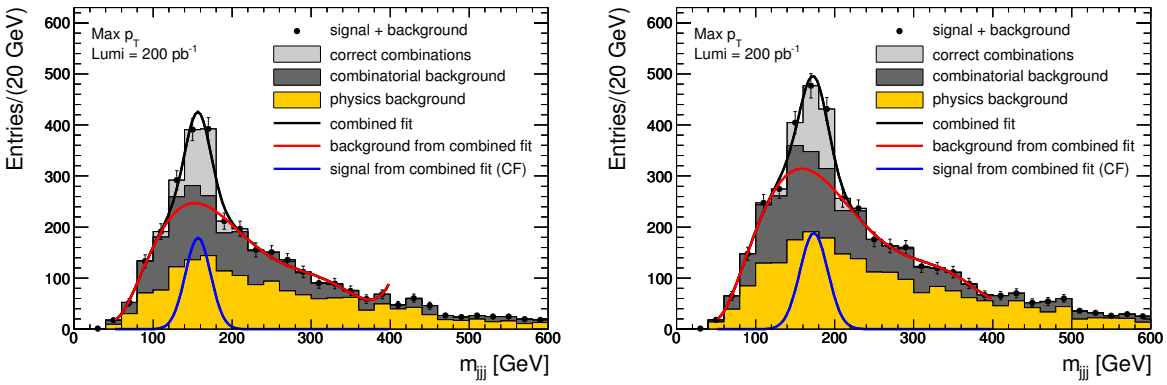

Figure 5.9.: Distribution of the 3-jet invariant mass in the electron channel reconstructed using the Max-p_T method. The effect of a reduced jet energy scale by 5% is shown on the left and of an increased one by 5% on the right side.

For this study, the jet energy scale is varied by $\pm 5\%$ with respect to the default value. For both reconstruction methods, the mean value is shifted to lower values for reduced and shifted to larger values for increased jet energy scale. In Figure 5.9, the result is exemplarily shown for the Max-p_T method. The combined effect is with $\Delta m_{jjj}^{\text{syst}} = \pm 8.6\,\text{GeV}$ a bit smaller for the Max-p_T method compared to the Min-ΔR method with $\Delta m_{jjj}^{\text{syst}} = \pm 10.1\,\text{GeV}$.

b-Jet Energy Scale

In general, the b-jet energy scale is different from the light jet energy scale due to a different composition of the particle shower. They include semi-leptonic b- and c-quark decays where the hadronic shower is initiated in conjunction with a lepton/neutrino pair. This leads to a different fragmentation behaviour and thus to an additional source of systematic uncertainties.

The energy of b-jets is varied independently from the overall jet energy scale by $\pm 2.5\%$. Since no b-quark tagging is applied to the reconstructed calorimeter jets, a Monte Carlo truth reference is taken for this study. In particular, a calorimeter jet is defined to be a b-jet if its four-vector matches the generated b-quark within a cone of $\Delta R < 0.3$.

In consistency with the result above, the mean value of the Gaussian part is shifted towards the direction of the variation for both reconstruction methods. In case of the Max-p_T method, the shift is $\Delta m_{jjj}^{\text{syst}} = \pm 1.4\,\text{GeV}$ while in case of the Min-ΔR method the shift is slightly smaller with $\Delta m_{jjj}^{\text{syst}} = \pm 1.2\,\text{GeV}$. Nevertheless, the magnitude of the impact from the b-jet energy scale is much smaller with respect to the overall jet energy scale since in general only one out of three combined jets is effected.

One should keep in mind that muons and neutrinos are not included into the reference truth particle jets of the energy calibration. Nevertheless, any mass measurement from jets is very sensitive to these undetected particle. The resulting bias needs to be corrected for in order to obtain the correct pole mass value.

Background Normalisation

No particle collider experiment in the past reached the high centre-of-mass energies of the Large Hadron Collider. Unfortunately, the resulting multi-parton interactions are rarely calculated with next-to-leading order precision. Most of the processes are only known at leading order and their Monte Carlo simulation suffers from model dependencies and large theoretical uncertainties.

In particular the production cross section of processes with multiple jets involved are dominated by large uncertainties. Since the physics background of this analysis consists mainly of W/Z+jets and QCD multi jet events, a significant effect on the number of background events is expected.

In order to give a conservative estimation of the systematic uncertainty, a variation of the overall physics background normalisation by $\pm 50\%$ is performed. This results into a maximal shift of $\Delta m_{jjj}^{\text{syst}} = \pm 0.7\,\text{GeV}$ in case of the Max-p_T method and $\Delta m_{jjj}^{\text{syst}} = \pm 0.8\,\text{GeV}$ in case of the Min-ΔR method. Both are relatively small compared to the uncertainties from jet energy scale variations.

Once the production cross sections of these processes are measured from LHC data, model dependencies can be reduced and thus such a large variation of the physics background normalisation is no longer needed for this analysis.

Background Shape

In addition to the uncertainties of the production cross section also the shape of the 3-jet invariant mass spectrum is not very well known. Due to the large cross section in particular for low energetic QCD multi jet production, only limited statistics could be simulated which requires large scaling factors to model an integrated luminosity of $\mathscr{L} = 200\,\text{pb}^{-1}$. For this reason, the spectrum shape of W+jets events is taken in this analysis to describe the QCD multi jet background.

In order to estimate the systematic uncertainty of the distribution shape, a shape variation is performed covering four extreme models. The original physics background shape of the pseudo experiment is multiplied by a factor between 0 and 2, depending on the 3-jet invariant mass value m_{jjj}:

$$n'_{1,2} = n \pm n \cdot \frac{m_{jjj}}{m_{jjj}^{\max}} \qquad \text{and} \qquad n'_{3,4} = n \pm n \cdot \left(1 - \frac{m_{jjj}}{m_{jjj}^{\max}}\right). \tag{5.12}$$

Here, n is the number of original events, n'_x the number of calculated events and $m_{jjj}^{\max}$ was set to 600 GeV. All four transformation types are illustrated on the left side of Figure 5.10.

Even if the shape variations are quite large, the resulting shifts are relatively small. The overall systematic uncertainty in case of the Max-p_T method is $\Delta m_{jjj}^{\text{syst}} = \pm 0.9\,\text{GeV}$ and $\Delta m_{jjj}^{\text{syst}} = \pm 0.8\,\text{GeV}$ in case of the Min-ΔR method. This gives confidence also into the decision to estimate the shape for QCD multi jet event from W+jets processes.

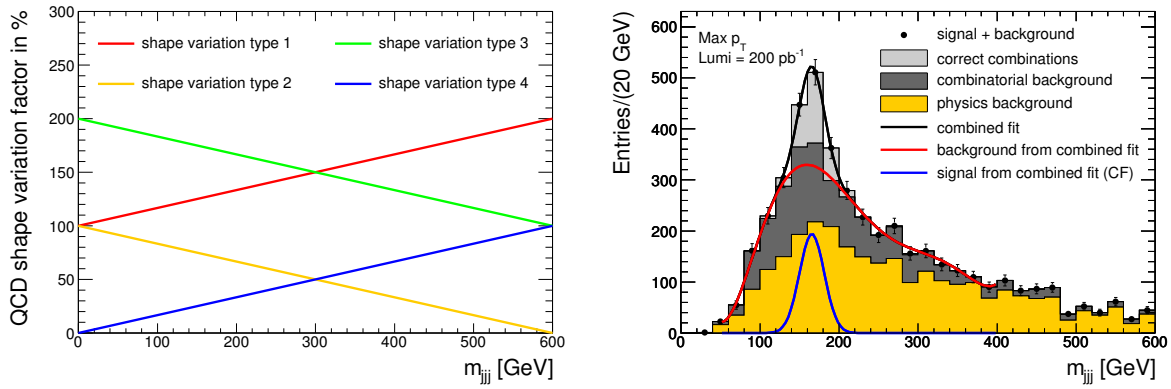

Figure 5.10.: Left: Shape variation factor corresponding to the four background shape variation types. Right: Distribution of the 3-jet invariant mass in the electron channel reconstructed using the Max-p_T method. The background shape is varied with the type 1 transformation.

Total Systematic Uncertainty

The individual contributions to the systematic uncertainty are summarised in table 5.5. The total systematic uncertainty per reconstruction method is derived by summing up all combined contributions per parameter in quadrature, considering statistical independence. This results into a total systematic uncertainty of $\Delta m_{jjj}^{\text{syst}} = \pm 8.8\,\text{GeV}$ for the Max-p_T method and $\Delta m_{jjj}^{\text{syst}} = \pm 10.2\,\text{GeV}$ for the Min-ΔR method.

	Max-p_T [GeV]		Min-ΔR [GeV]	
Parameter Variation	$m_{jjj}^{\text{fit}} \pm \Delta m_{jjj}^{\text{fit}}$	$\Delta m_{jjj}^{\text{syst}}$	$m_{jjj}^{\text{fit}} \pm \Delta m_{jjj}^{\text{fit}}$	$\Delta m_{jjj}^{\text{syst}}$
jet energy scale ($-5\,\%$)	156.9 ± 2.9	-8.3	159.4 ± 2.6	-7.1
jet energy scale ($+5\,\%$)	173.8 ± 2.6	$+8.6$	176.6 ± 3.0	$+10.1$
jet energy scale (maximum)		± 8.6		± 10.1
b-jet energy scale ($-2.5\,\%$)	164.8 ± 2.2	-0.4	165.6 ± 2.3	-0.9
b-Jet energy scale ($+2.5\,\%$)	166.6 ± 2.5	$+1.4$	167.7 ± 2.5	$+1.2$
b-Jet energy scale (maximum)		± 1.4		± 1.2
background normalisation ($-50\,\%$)	164.5 ± 2.0	-0.7	165.7 ± 2.2	-0.8
background normalisation ($+50\,\%$)	165.8 ± 2.6	$+0.6$	167.1 ± 2.7	$+0.6$
background normalisation (maximum)		± 0.7		± 0.8
background shape (type 1)	165.6 ± 2.3	$+0.4$	167.0 ± 2.4	$+0.5$
background shape (type 2)	164.7 ± 2.2	-0.5	166.0 ± 2.4	-0.5
background shape (type 3)	165.9 ± 2.3	$+0.7$	167.2 ± 2.4	$+0.7$
background shape (type 4)	164.3 ± 2.0	-0.9	165.7 ± 2.4	-0.8
background shape (maximum)		± 0.9		± 0.8
total (combined)		$\pm$ **8.8**		$\pm$ **10.2**

Table 5.5.: Summary of systematic uncertainties on m_{jjj} in the electron channel.

5.5.4. Numerical Results of the Muon Channel

In this section, a brief summary of the muon channel (cf. Chapter 1) results is provided. In contrast to electrons, muons do not leave a relevant signal within the calorimeters but are measured instead using the dedicated muon chamber system (cf. Chapter 2). Due to this, it is much more unlikely to fake a high-p_T muon in a multi jet environment compared to an electron. This leads to a significant reduction of the physics background, in particular of QCD multi jet events, and thus to an improvement of the signal to background ratio (cf. Section 5.3). Nevertheless, in order to ensure the comparability within these studies, no channel specific analysis constraints apart from the event selection cuts are applied. In particular, the $t\bar{t}$-candidate reconstruction methods and the fit functions are the same. As summarised in the Tables 5.6 and 5.7, the results of the muon channel are consistent with the results of the electron channel. A more detailed discussion on the results of both $t\bar{t}$-decay channels is provided in the final section of this chapter.

	Combined Fit (CF)		Separate Fit (SF)	
Recon. Method	$m_{jjj}^{CF} \pm \Delta m_{jjj}^{CF}$ [GeV]	χ^2/NDF	$m_{jjj}^{SF} \pm \Delta m_{jjj}^{SF}$ [GeV]	χ^2/NDF
Max-p_T	166.9 ± 3.6	1.7/8	168.2 ± 1.2	3.3/2
Min-ΔR	163.9 ± 2.3	11.6/8	167.8 ± 1.2	5.4/2

Table 5.6.: Numerical results of the combined and separate fit for the Max-p_T and Min-ΔR method in the muon channel including statistical uncertainties.

	Max-p_T [GeV]		Min-ΔR [GeV]	
Parameter Variation	$m_{jjj}^{\text{fit}} \pm \Delta m_{jjj}^{\text{fit}}$	$\Delta m_{jjj}^{\text{syst}}$	$m_{jjj}^{\text{fit}} \pm \Delta m_{jjj}^{\text{fit}}$	$\Delta m_{jjj}^{\text{syst}}$
jet energy scale ($-5\,\%$)	156.4 ± 3.4	-10.5	154.2 ± 2.9	-9.7
jet energy scale ($+5\,\%$)	168.2 ± 4.7	$+1.3$	170.9 ± 4.3	$+7.0$
jet energy scale (maximum)		± 10.5		± 9.7
b-jet energy scale ($-2.5\,\%$)	164.5 ± 3.3	-2.4	162.0 ± 2.0	-1.9
b-jet energy scale ($+2.5\,\%$)	167.2 ± 4.2	$+0.3$	166.3 ± 2.5	$+2.4$
b-jet energy scale (maximum)		± 2.4		± 2.4
background normalisation ($-50\,\%$)	167.5 ± 3.3	$+0.6$	164.1 ± 2.1	$+0.2$
background normalisation ($+50\,\%$)	165.8 ± 5.1	-1.1	163.7 ± 2.5	-0.2
background normalisation (maximum)		± 1.1		± 0.2
background shape (type 1)	166.6 ± 4.0	-0.3	163.7 ± 2.2	-0.2
background shape (type 2)	167.1 ± 3.1	$+0.2$	164.1 ± 2.2	$+0.2$
background shape (type 3)	164.6 ± 4.9	-2.3	163.6 ± 2.2	-0.3
background shape (type 4)	167.7 ± 2.5	$+0.8$	164.3 ± 2.2	$+0.4$
background shape (maximum)		± 2.3		± 0.4
total (combined)		$\pm$ **11.1**		$\pm$ **10.0**

Table 5.7.: Summary of systematic uncertainties on m_{jjj} in the muon channel.

5.6. Final Results and Discussion

In the following, the final results of this chapter are summarised and discussed. All studies are performed on Monte Carlo simulated pp-collision events in order to investigate the prospects of a top quark mass measurement in the lepton plus jets $t\bar{t}$-decay channel with the ATLAS detector. The analysis corresponds to a centre-of-mass energy of $\sqrt{s} = 10\,\text{TeV}$ and an integrated luminosity of $\mathscr{L} = 200\,\text{pb}^{-1}$. It is performed using a cut based event selection and compares several top quark reconstruction methods of the hadronic decay branch. It turns out that the Max-p_T and Min-ΔR reconstruction methods show the most promising results.

A χ^2-fit procedure of the combined distribution of signal and background events is chosen in order to estimate the mean value of the signal events which are found to be Gaussian distributed. According to Chapter 1, the mean value of this 3-jet invariant mass signal spectrum can be finally translated into the top quark pole mass through a correction of the residual bias. The analysis is completed by a study of all relevant systematic uncertainties. It turns out, that the most important systematic uncertainty arises from the variation of the jet energy scale.

The results of the 3-jet invariant mass measurement from one typical pseudo-experiment are summarised below, divided by $t\bar{t}$-decay channel type and top quark reconstruction method:

$$m^{\text{Max-p}_T}_{jjj,\text{el-channel}} = 165.2 \pm 2.2|_{stat.} \pm 8.8|_{syst.}\,\text{GeV} \quad (5.13)$$

$$m^{\text{Min-}\Delta\text{R}}_{jjj,\text{el-channel}} = 166.5 \pm 2.4|_{stat.} \pm 10.2|_{syst.}\,\text{GeV} \quad (5.14)$$

$$m^{\text{Max-p}_T}_{jjj,\text{mu-channel}} = 166.9 \pm 3.6|_{stat.} \pm 11.1|_{syst.}\,\text{GeV} \quad (5.15)$$

$$m^{\text{Min-}\Delta\text{R}}_{jjj,\text{mu-channel}} = 163.9 \pm 2.3|_{stat.} \pm 10.0|_{syst.}\,\text{GeV}. \quad (5.16)$$

First of all, the results are consistent within their statistical uncertainties, independent of the $t\bar{t}$-decay channel type and the top quark reconstruction method. Compared to the generated top quark mass value of $m_t^{gen} = 172.5\,\text{GeV}$, all central values are shifted towards lower mass values by about 5 to 9 GeV. This can be explained by the expected differences of the 3-jet invariant mass and the top quark pole mass, which needs to be corrected for in the next step.

In order to study the overall bias for the entire measurement, a larger sample of statistical independent pseudo-experiments is investigated. The pseudo-experiments are generated using Poissonian smearing of the initial 3-jet invariant mass distribution, considering all Monte Carlo simulated events per $t\bar{t}$-decay channel. For each of the 400 generated pseudo-experiments, the χ^2-fit procedure is performed applying the fit function described in Section 5.5.2.

The first statistical test performed is the calculation of the sample's pull distribution from the results of the individual χ^2-fits. The pull variable is defined as

$$\text{pull} = \frac{m_t^{gen} - m_{jjj}^{\text{meas}}}{\sigma_{m_{jjj}^{\text{meas}}}^{\text{stat}}}, \tag{5.17}$$

where m_t^{gen} is the generate top quark mass, m_{jjj}^{meas} the measured 3-jet invariant mass of each pseudo-experiment and $\sigma_{m_t^{\text{meas}}}^{\text{stat}}$ the corresponding statistical uncertainty. The distribution of the pull variable is exemplarily shown on the left side of Figure 5.11 for the Max-p_T method in the electron channel. Here, the width of the pull variable distribution is a measure of the reliability of the statistical uncertainty estimation. Since for each decay channel and reconstruction method (cf. Table 5.8, the width of the Gaussian shaped pull distribution is compatible with unity, the statistical uncertainty is well estimated by the χ^2-fit procedure. The actual

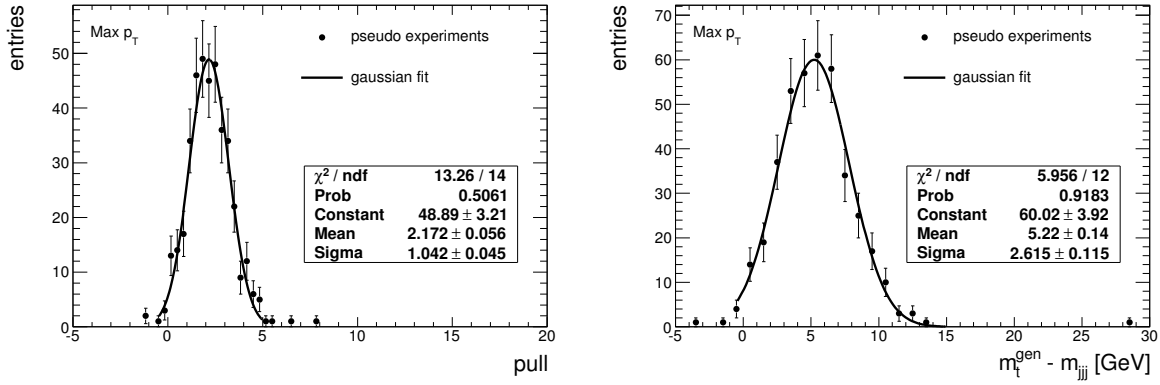

Figure 5.11.: Distribution of the pull variable (left) and the bias (right) for a sample of 400 pseudo-experiments in the electron channel using the Max-p_T reconstruction method.

bias is investigated calculating the difference between the generated and the measured masses, $m_t^{gen} - m_{jjj}^{\text{meas}}$. The result is shown on the right side of Figure 5.11 for the Max-p_T method in the electron channel again. The mean of the Gaussian shaped distribution gives the average bias per pseudo-experiment with respect to the generated top quark mass. The numerical results are given in Table 5.8 and it turns out that the average shift is about 5 GeV in the electron channel and about $6 - 7$ GeV in the muon channel. Thus the chosen measurement methods in this analysis underestimate the generated top mass value by about $3 - 4\,\%$.

	Electron Channel		Muon Channel	
Test parameter	Max-p_T	Min-ΔR	Max-p_T	Min-ΔR
σ_{pull}	1.042 ± 0.045	1.030 ± 0.040	1.066 ± 0.042	1.024 ± 0.047
$m_t^{gen} - m_{jjj}^{\text{meas}}$	5.22 ± 0.14	5.43 ± 0.12	6.05 ± 0.11	7.30 ± 0.12

Table 5.8.: Numerical results of statistical tests on a sample of 400 statistical independent pseudo-experiments.

The observed bias of this top quark mass measurement can have several origins. The main reasons are expected from the following four effects:

1. the choice of the top quark reconstruction method,

2. the choice of the combined fit function and the entire fit procedure,

3. the fact that exactly four jets are considered for the top quark reconstruction which neglects effects from jet splitting and merging as well as additional gluon radiation

4. and the missing parton level corrections of the jet energy, in particular for jets with semi-leptonic b-quark decays in the cascade.

In general, it is difficult to disentangle these effects. In the following, the magnitude and the direction of the shift from each individual effect is estimated from the studies performed in this chapter. Due to the absence of a real reference method, both top quark reconstruction methods are only compared to each other. Since the top mass values derived from the Max-p_T and Min-ΔR method are close to each other, no large bias is expected from this choice. Nevertheless, the studies in Section 5.4 indicate that using a worse performing reconstruction method might lead to a different result.

In order to study the impact of the fit procedure, the results of the combined and the separate fit are compared for the sample of 400 pseudo-experiments. The distribution of the difference between both is shown in Figure 5.12 for the electron channel and the Max-p_T method. It turns out that the combined fit results lead to on average smaller mass values by about $1 - 1.5\,\text{GeV}$ in the electron channel and $2\,\text{GeV}$ in the muon channel.

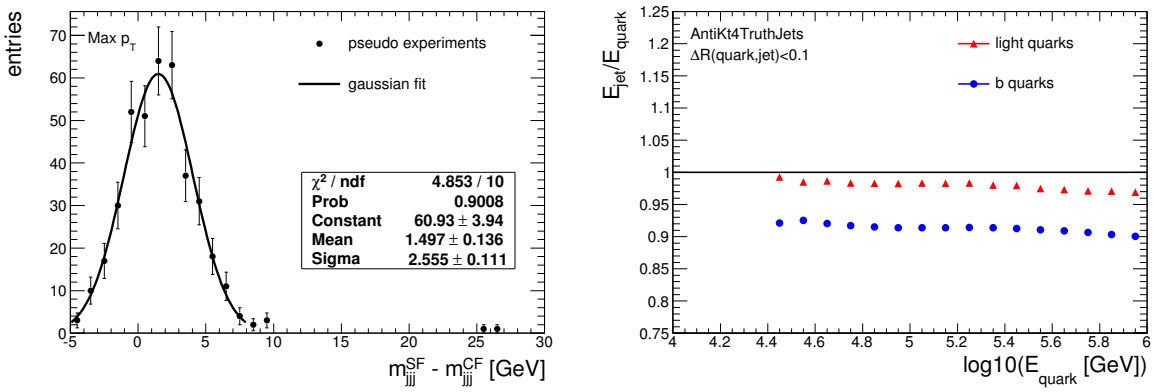

Figure 5.12.: Left: Distribution of the difference between combined and separate fit results for a sample 400 pseudo-experiments. On average, the combined fit returns a smaller value of about $1.5\,\text{GeV}$. Right: Ratio of the truth particle jet energy over the energy of a matched quark, for light and b-quark jets. While the energy response is close to one for light quark jets, the energy of b-quark jets is underestimated on average by about $7 - 10\,\%$.

The third effect concerns the number of jets belonging to the hadronic top quark decay branch. In order to give a reasonable magnitude, further studies comparing different hadronisation models and jet algorithms would be needed. Nevertheless, this analysis aimed to keep this effect small while using the infra-red safe anti-kt jet reconstruction algorithm.

The largest bias is expected from the fourth effect, since no dedicated parton level corrections are applied to the jet energy in this analysis. The jets considered for the top quark mass measurement are calibrated with respect to Monte Carlo truth jets using the jet level corrections described in Chapter 4. The differences between truth jet and parton level are expected to be small for light quark jets but much larger for b-quark jets due to the presence of semi-leptonic b-quark decays. These decays include high energetic neutrinos which cannot be detected with the ATLAS detector and thus are not included into the definition of the truth jet object.

The differences between truth jet and parton level for light quark and b-quark jets are shown on the right side of Figure 5.12. Here, the ratio of the quark energy and the energy of its corresponding jet (matching criteria: $\Delta R < 0.1$) is calculated for a wide range of quark energies including all η-regions. While the energy response is close to one for light quark jets, the energy of b-quark jets is underestimated on average by about $7 - 10\,\%$. This leads finally to a shift of about $4 - 6\,\mathrm{GeV}$ towards smaller values for the average top quark mass [75]. The bias can be reduced applying a dedicated in-situ calibration of the jet energy using hadronic W- and Z-boson decays (cf. Chapter 3). In addition, semi-leptonic b-quark jets need to be identified in order to apply specific corrections for the undetected neutrino energy.

For the moment, the bias must be taken into account in order to obtain a correct result of the top quark measurement. The bias correction is performed by simply adding the average shift to the central value of the result for the pseudo-experiment described above. As a consequence, the generated top quark mass value of $m_t^{gen} = 172.5\,\mathrm{GeV}$ is now covered by the statistical uncertainty in both top quark decay channels and for each reconstruction method:

$$m_{t,\text{el-channel}}^{\text{Max-p}_\text{T}} = 170.4 \pm 2.2|_{stat.} \pm 8.8|_{syst.}\,\mathrm{GeV} \quad (5.18)$$

$$m_{t,\text{el-channel}}^{\text{Min-}\Delta\text{R}} = 171.9 \pm 2.4|_{stat.} \pm 10.2|_{syst.}\,\mathrm{GeV} \quad (5.19)$$

$$m_{t,\text{mu-channel}}^{\text{Max-p}_\text{T}} = 171.9 \pm 3.6|_{stat.} \pm 11.1|_{syst.}\,\mathrm{GeV} \quad (5.20)$$

$$m_{t,\text{mu-channel}}^{\text{Min-}\Delta\text{R}} = 171.2 \pm 2.3|_{stat.} \pm 10.0|_{syst.}\,\mathrm{GeV}. \quad (5.21)$$

One should keep in mind that the magnitude of the shift varies depending on the analysis conditions, in particular on the generated top quark mass of the Monte Carlo simulation. A consequent enhancement of the described analysis would be the replication of the entire measurement on Monte Carlo samples, simulated with different top quark mass points than $m_t^{gen} = 172.5\,\mathrm{GeV}$.

Monte Carlo samples for different top quark mass points would further allow to retrieve a direct correlation between the generated and the measured top quark mass. In this case, a correction of the bias from the jet energy calibration level is automatically included in the top quark mass measurement and the dependency on the generated top quark mass is resolved.

In order to reduce the bias due to the model dependency of the fit function, a Template Method can be taken into account. Here, the 3-jet invariant mass distribution (or any other top quark mass dependent variable) is obtained for all available Monte Carlo samples with different generated top quark mass values (Monte Carlo templates). The shape of the distribution obtained from a pseudo-experiment (or real LHC data) is then directly compared to the shape of these Monte Carlo templates. The overall agreement is expressed by a χ^2-distribution depending on the generated top quark mass. The top quark mass value corresponding to the minimum of χ^2-distribution is finally interpreted as the measured top quark mass.

Promising studies of the template method have been performed already during this analysis. Unfortunately, Monte Carlo samples for different top quark mass points than $m_t^{gen} = 172.5\,\text{GeV}$ were only available for fast simulation at that time. This led to an incompatible calibration of the jet energy between signal and background processes since dedicated jet energy corrections for jets with local hadron calibration did not exist. Nevertheless, there are promising studies of the template method on first ATLAS data considering a different jet energy calibration [76].

As a conclusion, the Monte Carlo studies presented in this chapter show that a top quark mass measurement is feasible with a good accuracy considering $\mathscr{L} = 200\,\text{pb}^{-1}$ of ATLAS data. The results obtained for one typical pseudo-experiment are stable and consistent, independent of the top quark decay channel and the reconstruction method. The observed shift of the central value could be explained considering biases from the χ^2-fit procedure and the jet energy calibration level. An improvement of the accuracy could be achieved, considering b-tagging information during the top quark reconstruction as well as data driven background estimation.

6. Summary and Conclusion

> "Wir können das Universum nicht erklären, sondern nur beschreiben; und wir wissen nicht, ob unsere Theorien wahr sind, wir wissen nur, dass sie nicht falsch sind."
>
> HARALD LESCH [77]

In this thesis, two major research projects were presented. One is the development of a new energy calibration method for calorimeter jets in ATLAS, the other is a Monte Carlo based study of the prospects for a top quark mass measurement with the ATLAS detector. The top quark study is further one of the first analyses where the new jet energy calibration is applied.

In order to motivate the development of a new jet energy calibration method, an overview of the jet reconstruction and energy calibration chain in ATLAS was provided in Chapter 3. It started with the description of the topological clustering of calorimeter cells, continued with local hadron calibration on cluster level and closed with the description of the major jet reconstruction algorithms. It was further shown that the energy of calorimeter jets, reconstructed from pre-calibrated topological cell clusters, suffers from lost particles in the non-instrumented up-stream detector material. For this reason, additional calibration is needed in order to bring the jet energy to the Monte Carlo truth particle level.

The new calibration approach, introduced in Chapter 4, was based on information about the jet shapes and the energy distribution inside a jet. For this reason, an extended study of jet shape variables on Monte Carlo multi-jet samples was presented. The focus was set on studying non-linearities of the average jet energy response with respect to the energy of truth particle jets. It was shown that among various jet shape variables only the transverse energy fraction of low energetic clusters E_T^{frac} has a significant sensitivity to the non-linearities. It was thus chosen as a third variable together with E and η to calculate the jet energy calibration coefficients. Finally, a dedicated set of calibration constants was derived from Monte Carlo multi-jet samples using the method of numerical inversion.

In order to test the new calibration strategy, it was applied on jets in various Monte Carlo samples. As result, the average jet energy response was close to $\langle R_{jet} \rangle = 1.0$ and linear within $1-2\,\%$ over a wide range of jet energies and η-regions for all Monte Carlo samples. Furthermore, the dependency on the underlying physics process was reduced by adopting the jet shape variable E_T^{frac}. In addition, a small improvement of the jet energy response resolution $\Delta_{R_{jet}}$ was observed compared to the constituent level.

For a second test, the new calibration constants were applied on first ATLAS minimum bias events from $\sqrt{s} = 900\,\text{GeV}$ proton-proton collisions. Promising results were presented for the major jet properties including the input variables of the jet energy calibration. A comparison of the final jet energy scale with the previous calibration steps showed a consistent behaviour in data and Monte Carlo and an overall agreement within 2 %. These first results on ATLAS data are very promising and give confidence into the newly developed jet energy calibration method.

Nevertheless, the development of this jet energy calibration is an ongoing process. Even if the consideration of E_T^{frac} showed promising results, the analysis of additional jet shape variables is still ongoing. One way to further improve the impact of the jet properties is to consider also track based jet shape variables which are reconstructed from hits in the inner detector system. In addition, binning effects could be reduced by a multidimensional interpolation method. Finally, an extrapolation method could be developed in order to cover empty phase space points which arise from low Monte Carlo statistics in particular for lower jet energies.

One strength of the jet calibration project is the fact that the software packages for the calculation and application of the calibration coefficients are fully integrated within the ATLAS software framework. This ensures that this jet energy calibration method can be applied to all future data analyses in ATLAS.

The second project of the thesis was a study of the prospects for a top quark mass measurement in the lepton plus jets decay channel of top quark pair events. The analysis was performed on a set of Monte Carlo simulated samples corresponding to an ATLAS dataset with an integrated luminosity of $\mathscr{L} = 200\,\text{pb}^{-1}$ at a centre-of-mass collision energy of $\sqrt{s} = 10\,\text{TeV}$. The entire measurement was performed separately for the electron channel and for the muon channel.

The data analysis for a typical pseudo-experiment started with a cut based event selection using a loose trigger on the high energetic electron or muon, respectively. Further cuts were applied on the transverse momentum of the lepton and of the jets as well as on the missing transverse energy. The energy of the jets was calibrated using the newly developed calibration method described in this thesis. The resulting dataset had a signal to background ratio of about 0.85 in the electron channel and of about 0.96 in the muon channel, respectively.

The top quark mass was extracted from a fit of the 3-jet invariant mass spectrum which was reconstructed from the jets of the hadronic top quark decay branch. In order to minimise combinatorial background from wrong jet combinations, an extended study of top quark reconstruction methods was performed. The efficiency of three different reconstruction methods plus a random selection was compared on different simulation levels, from pure generator four-vectors up to full detector simulation. It was shown that two methods, Max-p_T and Min-ΔR perform the best and thus are further taken into account for the top quark mass measurement.

For both top quark decay channels and both reconstruction methods, the 3-jet invariant mass spectrum was reconstructed from signal and background events. A combined fit of the 3-jet invariant mass spectrum was performed, using a Gaussian distribution for the signal part and a set of Legendre polynomials for the background distribution. The most probable value of the 3-jet invariant mass of this particular pseudo-experiment was extracted from the mean of the Gaussian part and the most promising result of $m_{jjj} = 165.2 \pm 2.2\,\text{GeV}$ was shown by the Max-p_T method in the electron channel. The other three combinations of decay channel and reconstruction method showed similar results.

In order to estimate the systematic uncertainty of this top quark mass measurement, the analysis was repeated varying the parameters corresponding to the major sources, like the jet energy scale and the background distributions. It turned out that varying the jet energy resulted into the largest shift of the extracted mass value. While the shifts from a variation of the background normalisation and shape are smaller than 1 GeV, the effect of a 5 % variation of the jet energy causes a shift of about $5 - 7\,\%$, i.e. about $8 - 11\,\text{GeV}$. Nevertheless, the assumption of a 5 % variation is very conservative and is going to be reduced with the progress of the ATLAS data taking.

Finally, the top quark pole mass was extracted from the measured 3-jet invariant mass. The difference among the two values was a bias mainly caused by the determination of the b-jet energy, the top quark reconstruction method and the fit process. The overall bias was determined by analysing the difference between the generated mass value and the measured 3-jet invariant mass value in about 400 individual pseudo-experiments. It turned out that the average bias is between 5 and 8 GeV, depending on the decay channel and the reconstruction method. After correcting for this bias, the generated top quark mass value of $m_t^{gen} = 172.5\,\text{GeV}$ is included into the ranges of the statistical uncertainties of all four previously described pseudo-experiments.

The results of this Monte Carlo study for a top quark mass measurement with the ATLAS detector are very promising. It was shown that even with very robust analysis the top quark mass can be measured with good accuracy on $\mathscr{L} = 200\,\text{pb}^{-1}$ of ATLAS data. The analysis could be refined by using b-tagging information or applying a refined event selection, e.g. using a Likelihood fit. The final extraction of the top quark mass from a combined fit plus a bias correction is very stable against systematics. It could be improved by the usage of Monte Carlo samples generated for a set of different top quark mass points around the expected mass value. On top of the combined fit of the 3-jet invariant mass distribution also the comparison to template distribution can be taken into account.

One can conclude that the top quark mass measurement studied in this thesis, including the application of the newly developed jet energy calibration, can be successfully applied to ATLAS collision data.

A. Appendix

A.1. Technical Information on Monte Carlo Samples

Sample	p_T^{min} [GeV]	p_T^{max} [GeV]
J0	8	17
J1	17	35
J2	35	70
J3	70	140
J4	140	280
J5	280	560
J6	560	1120
J7	1120	2240
J8	2240	–

Table A.1.: Definition of p_T-slices for the leading parton (`Pythia`) or leading jet (`AlpGen`) in simulated QCD jet events.

A.2. Additional Figures on Jet Shape Variables

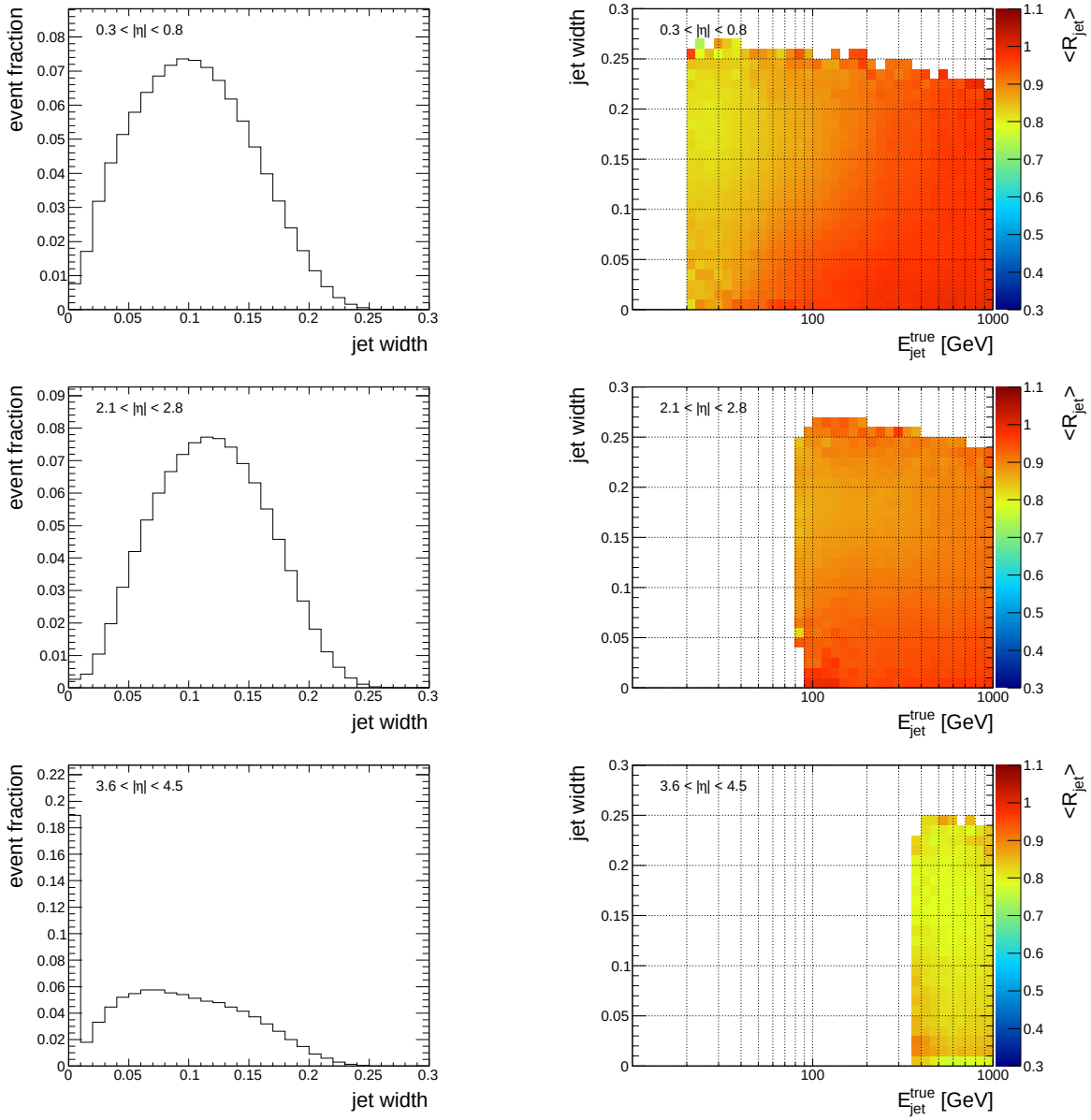

Figure A.1.: Distribution of the jet width and the average jet energy response for `AntiKt4LCTopoJets` in additional η-regions.

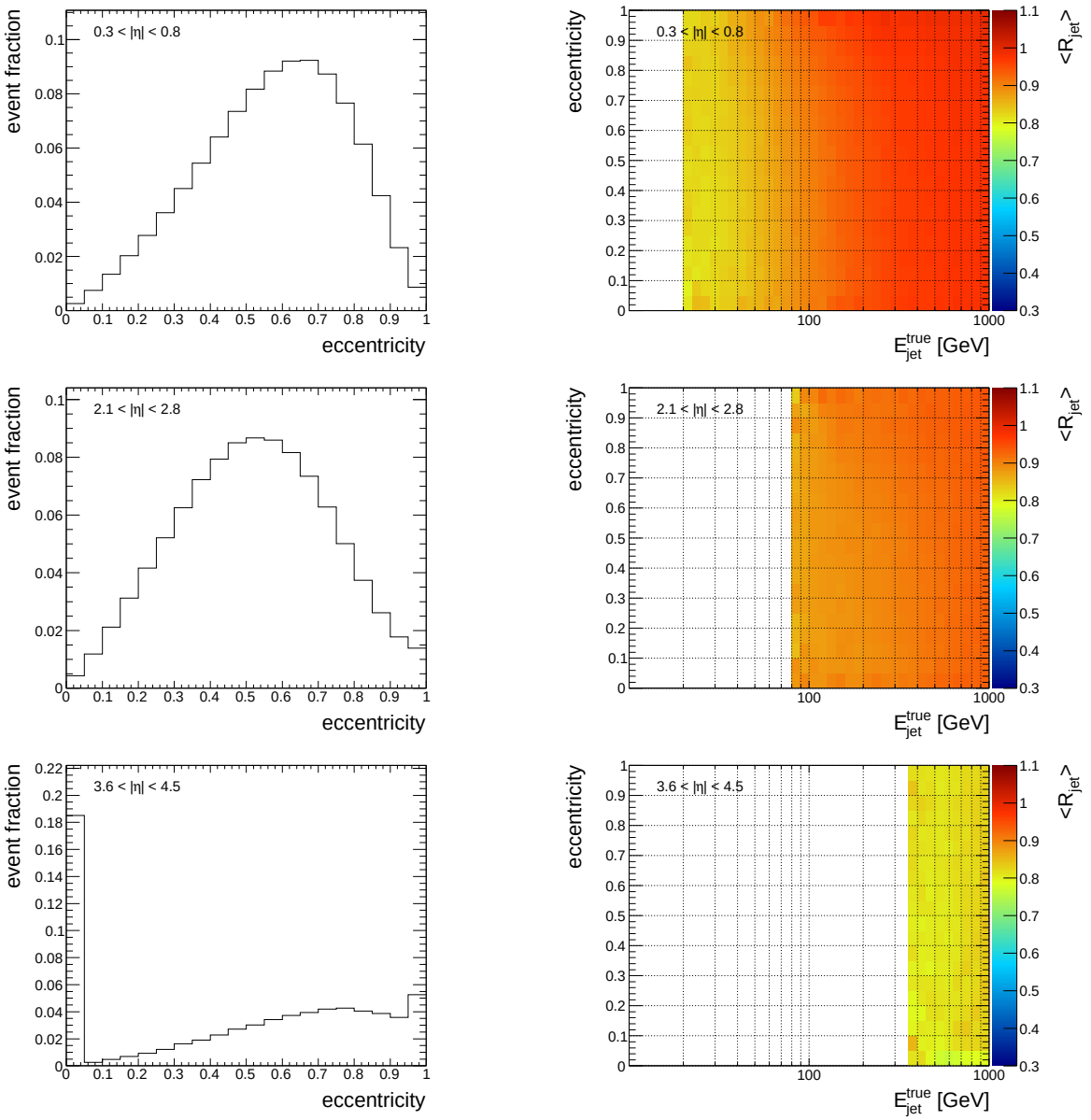

Figure A.2.: Distribution of the jet eccentricity and the average jet energy response for `AntiKt4LCTopoJets` in additional η-regions.

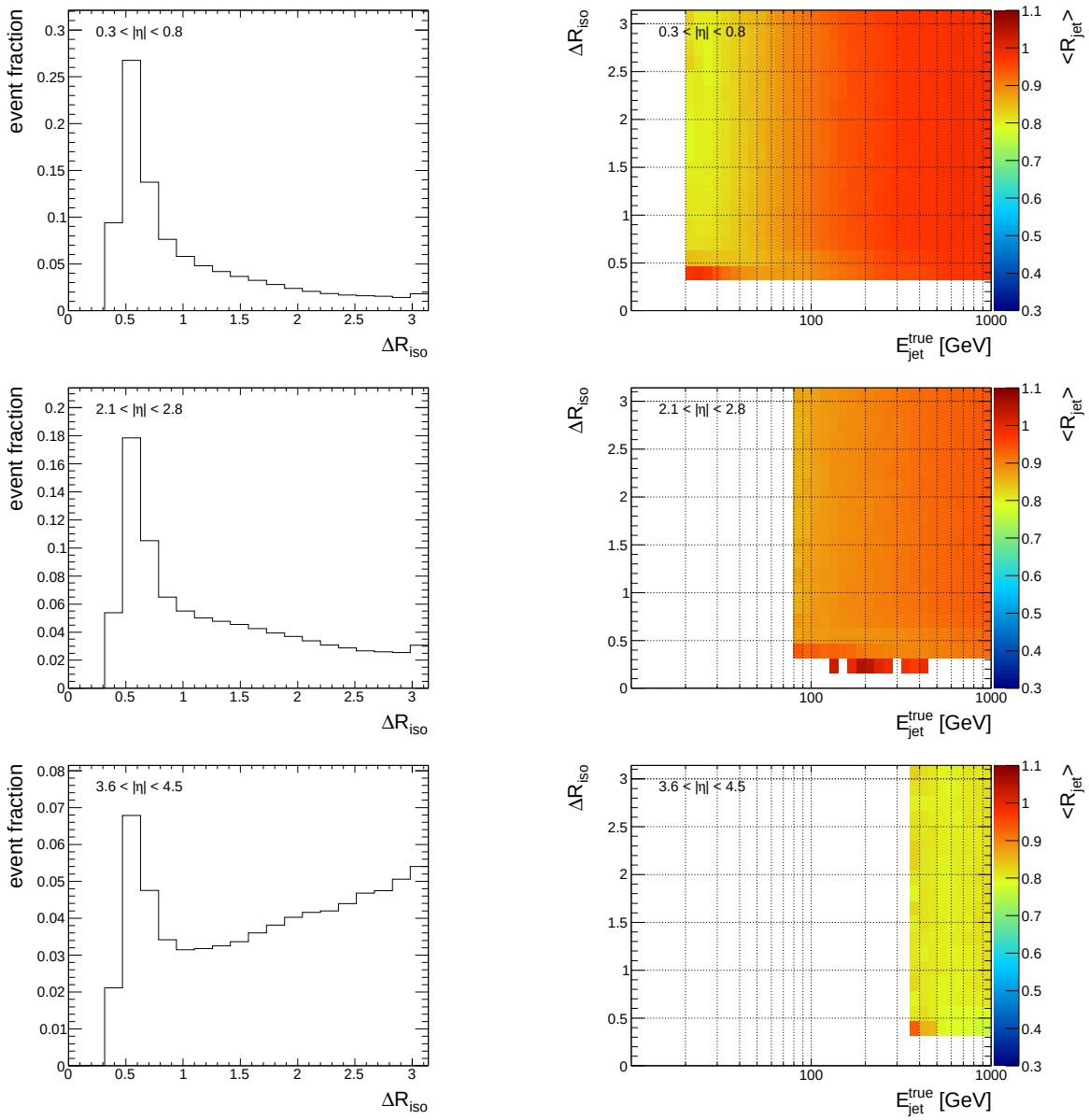

Figure A.3.: Distribution of the isolation distance and the average jet energy response for `AntiKt4LCTopoJets` in additional η-regions.

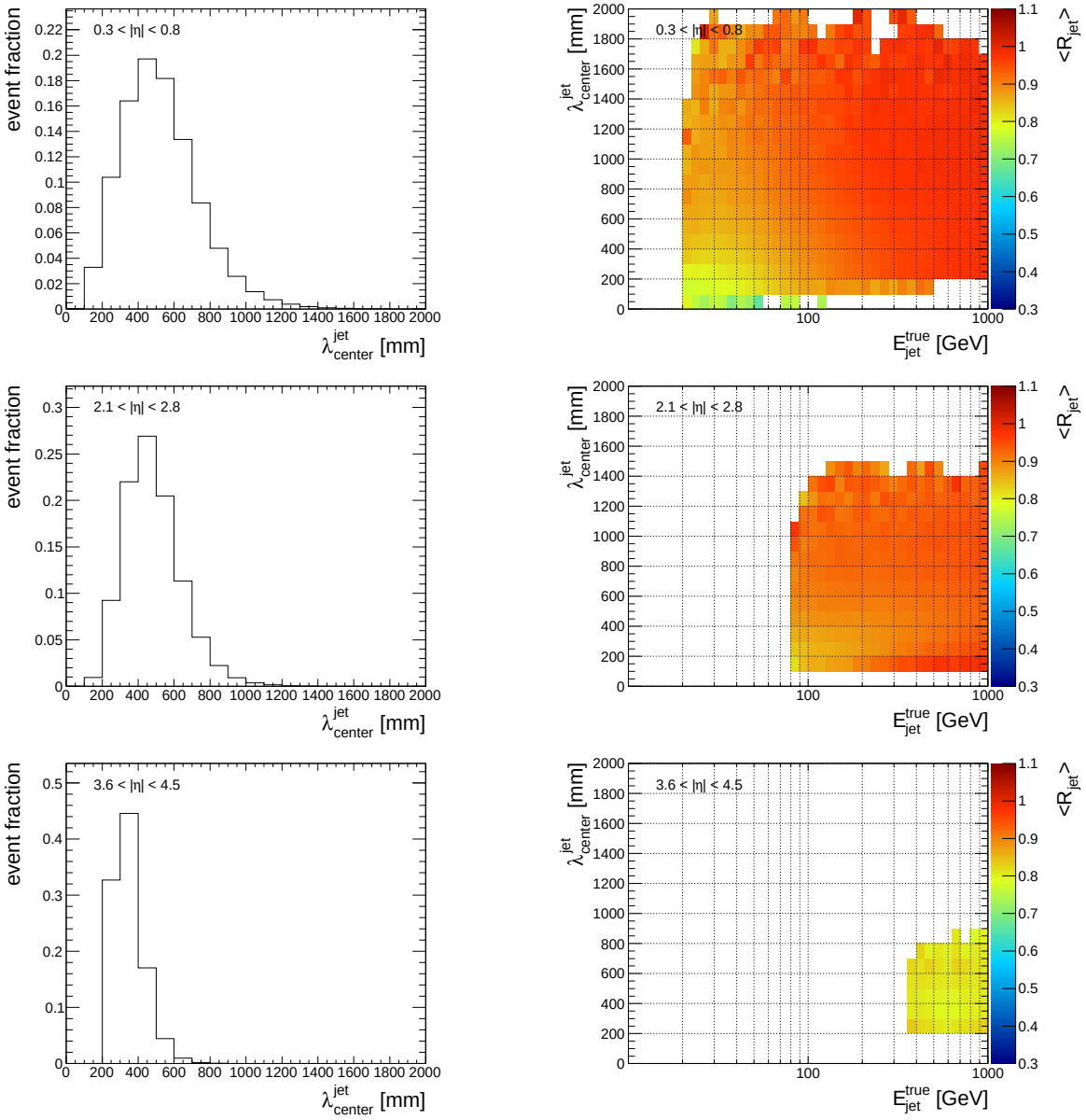

Figure A.4.: Distribution of the λ^{jet}_{centre} and the average jet energy response for `AntiKt4LCTopoJets` in additional η-regions.

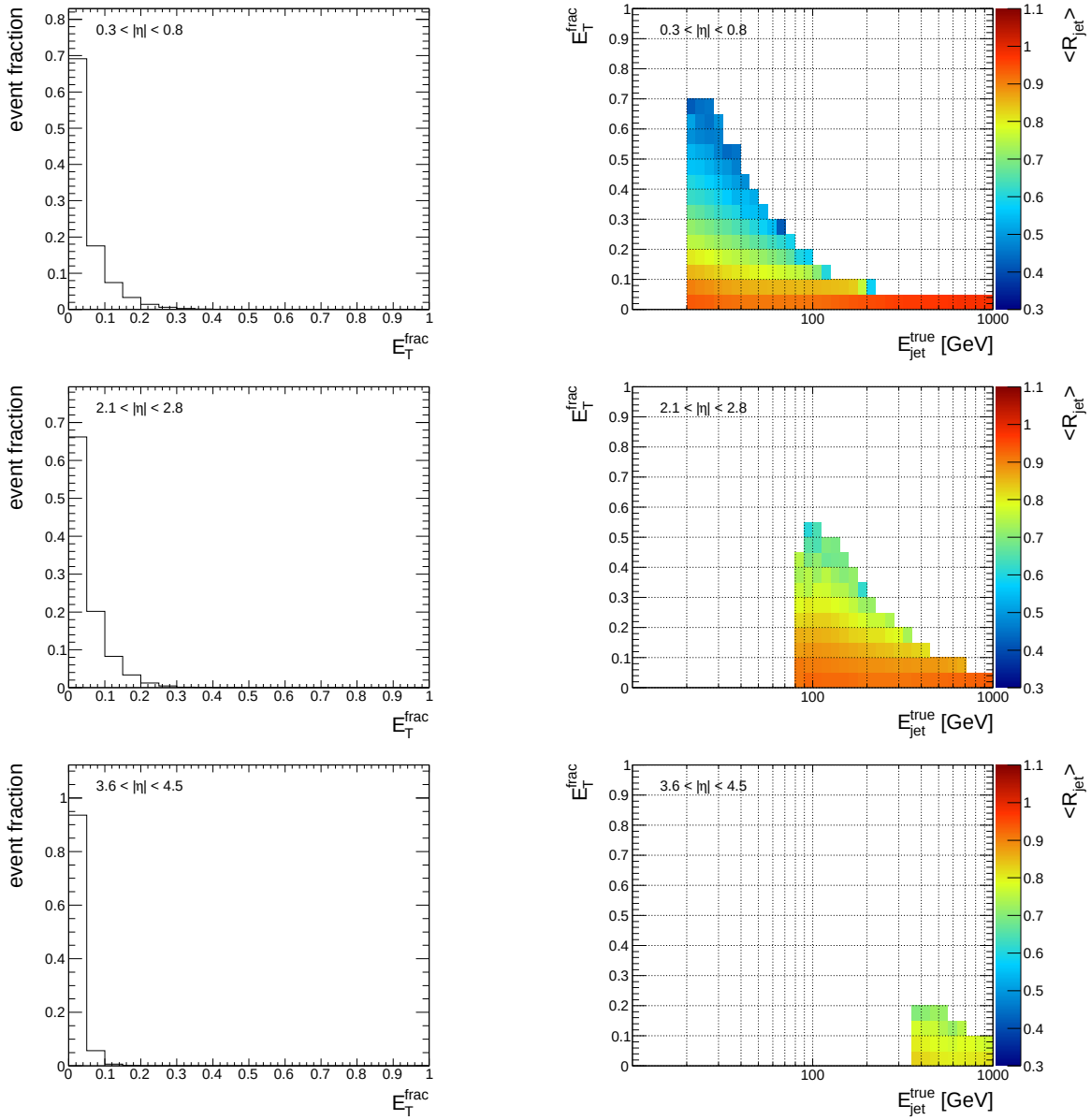

Figure A.5.: Distribution of E_T^{frac} and the average jet energy response for `AntiKt4LCTopoJets` in additional η-regions.

List of Figures

1.1. Phenomenological model of a hard proton-proton interaction. 8
1.2. Experimental limits on the Higgs boson mass and Standard Global CKM Fit. . . 10
1.3. Comparison of the indirect constraints on m_W and m_t. 11
1.4. Feynman diagrams for top quark pair production via the strong interaction. . . . 12
1.5. Feynman diagrams for electroweak single top quark production. 13
1.6. Leading order Feynman diagram of the lepton plus jets channel in $t\bar{t}$-events. . . . 14
1.7. QCD prediction of the $t\bar{t}$ cross section and world average of the top quark mass. 16

2.1. Schematic view of the Large Hadron Collider at CERN. 18
2.2. Schematic view of the ATLAS detector. 19
2.3. Cut-away view of the ATLAS inner detector system. 21
2.4. Schematic view of the ATLAS Calorimeter System. 23
2.5. Sketch of an EMB module and artist's view of one HEC module. 24
2.6. Schematic view of the HEC LAr gap and the hadronic endcap calorimeter. 25
2.7. Electrode structure of the first FCal module and sketch of a Tile segment. 26
2.8. Linearity (left) and fractional resolution (right) of the pion energy response. . . . 27
2.9. Schematic view of the ATLAS Muon Spectrometer System. 28
2.10. Sketch of the ATLAS trigger system 30

3.1. Sketch of the different reference levels of jets, depending on their constituents. . . 33
3.2. Exemplary illustration of the topological cell clustering algorithm. 39
3.3. Illustration of the hadronic shower profile. 41
3.4. Sketch of the various contributions to Local Hadron Calibration. 44
3.5. Linearity (left) and resolution (right) of the pion energy response. 45
3.6. Schematic view on the reconstruction sequences for calorimeter jets. 48

4.1. Average jet energy response $\langle R_{jet} \rangle$ of `AntiKt4LCTopoJets`. 52
4.2. Distribution of the jet width and average jet energy response. 54
4.3. Distribution of the jet eccentricity and average jet energy response. 54
4.4. Distribution of the isolation distance and the average jet energy response. 55
4.5. Distribution of λ_{centre}^{jet} and the average jet energy response. 56
4.6. Distribution of E_T^{frac} and the average jet energy response. 57
4.7. Value of the jet energy calibration weight factors. 59
4.8. Average jet energy response $\langle R_{jet} \rangle$ after the final calibration step. 61
4.9. Development of the average jet energy response for different calibration steps. . . 62

4.10. Average jet energy response in QCD dijet events. 63
4.11. Average jet energy response in QCD multijet events. 64
4.12. Average jet energy response in all hadronic top quark pair events. 65
4.13. Comparison of jets in early data events and from Monte Carlo simulation. 67
4.14. Distribution of the average energy ratios with respect to the E_{jet}^{em}. 69
4.15. Distribution of the average energy ratios with respect to the η-position. 69
4.16. Distribution of the average energy ratios with respect to E_T^{frac}. 70

5.1. Distribution of the $E_{\mathrm{T}}^{\mathrm{miss}}$ significance and transverse momentum of the fourth jet. 83
5.2. Cut-flow diagram for the online and offline event selection. 84
5.3. Event fraction of the four possible quark combinations at parton level. 87
5.4. Event fraction of the four possible quark combinations at jet level. 89
5.5. Distribution of the 3-jet invariant mass for correct and false combinations. 90
5.6. Invariant mass distribution of the selected 3-jet combination. 92
5.7. Combined fit of one pseudo-experiment using the Max-$\mathrm{p_T}$ method. 95
5.8. Combined fit of one pseudo-experiment using the Min-ΔR method. 96
5.9. Distribution of the 3-jet invariant mass with varied jet energy scale. 97
5.10. Variation factor for background shape and 3-jet invariant mass distribution. . . . 100
5.11. Distribution of the pull variable and the bias. 103
5.12. Difference between combined and separate fit, jet energy response w.r.t. partons. 104

A.1. Distribution of the jet width in additional η-regions. 112
A.2. Distribution of the jet eccentricity in additional η-regions. 113
A.3. Distribution of the isolation distance in additional η-regions. 114
A.4. Distribution of λ_{centre}^{jet} in additional η-regions. 115
A.5. Distribution of E_T^{frac} in additional η-regions. 116

List of Tables

1.1. The three generations of fundamental fermions. 6
1.2. The fundamental interactions in the Standard Model of Particle Physics. 6
1.3. Calculated cross sections for top quark pair and single top production. 13
1.4. Integrated branching ratio of the top quark pair decay channels. 14

5.1. Monte Carlo generated signal and background samples including k-factors [38]. . 78
5.2. Expected number of events after each selection cut for the electron channel. . . . 85
5.3. Expected number of events after each selection cut for the muon channel. 85
5.4. Numerical results of the combined and separate fit in the electron channel. 96
5.5. Summary of systematic uncertainties on m_{jjj} in the electron channel. 100
5.6. Numerical results of the combined and separate fit in the muon channel. 101
5.7. Summary of systematic uncertainties on m_{jjj} in the muon channel. 101
5.8. Numerical results of statistical tests. 103

A.1. Definition of p_T-slices in simulated QCD jet events. 111

Bibliography

[1] R. P. Feynman, *QED. The Strange Theory of Light and Matter.* Princeton University Press, 1985.

[2] **Particle Data Group**, K. Nakamura et al., *Review of Particle Physics*, J. Phys. **G37** (2010) 075021.

[3] B. Povh et al., *Teilchen und Kerne: Eine Einführung in die physikalischen Konzepte.* Springer, Berlin, Germany, 1993.

[4] M. Böhm et al., *Gauge theories of the strong and electroweak interaction.* Vieweg & Teubner, 2001.

[5] A. Quadt, *Top quark physics at hadron colliders*, Eur. Phys. J. **C48** (2006) 835–1000.

[6] J. R. Incandela et al., *Status and Prospects of Top-Quark Physics*, Prog. Part. Nucl. Phys. **63** (2009) 239–292.

[7] S. L. Glashow, *Partial Symmetries of Weak Interactions*, Nucl. Phys. **22** (1961) 579–588.

[8] S. Weinberg, *A Model of Leptons*, Phys. Rev. Lett. **19** (1967) 1264–1266.

[9] A. Salam, *Weak and Electromagnetic Interactions*, originally printed in "Svartholm: Elementary Particle Theory, Proceedings of the Nobel Symposium held 1968 at Lerum, Sweden", Stockholm 1968, 367-377.

[10] P. W. Higgs, *Broken Symmetries and the Masses of Gauge Bosons*, Phys. Rev. Lett. **13** (1964) 508–509.

[11] N. Cabibbo, *Unitary Symmetry and Leptonic Decays*, Phys. Rev. Lett. **10** (1963) 531–532.

[12] M. Kobayashi and T. Maskawa, *CP violation in the renormalizable theory of weak interaction*, Prog. Theor. Phys. **49** (1973) 652–657.

[13] D. J. Gross and F. Wilczek, *Asymptotically Free Gauge Theories. 1*, Phys. Rev. **D8** (1973) 3633–3652.

[14] D. J. Gross and F. Wilczek, *Ultraviolet behavior of non-Abelian gauge theories*, Phys. Rev. Lett. **30** (1973) 1343–1346.

[15] D. J. Gross and F. Wilczek, *Asymptotically free gauge theories. 2*, Phys. Rev. **D9** (1974) 980–993.

[16] R. K. Ellis, W. J. Stirling, and B. R. Webber, *QCD and Collider Physics*, Camb. Monogr. Part. Phys. Nucl. Phys. Cosmol. **8** (1996) 1–435.

[17] M. Dobbs et al., *Les Houches guidebook to Monte Carlo generators for hadron collider physics*, pp. 411–459. 2004. Compiled by the Working Group on Quantum Chromodynamics and the Standard Model.

[18] Y. L. Dokshitzer, *Calculation of the Structure Functions for Deep Inelastic Scattering and e+ e- Annihilation by Perturbation Theory in Quantum Chromodynamics*, Sov. Phys. JETP **46** (1977) 641–653.

[19] V. N. Gribov and L. N. Lipatov, *Deep inelastic e p scattering in perturbation theory*, Sov. J. Nucl. Phys. **15** (1972) 438–450.

[20] G. Altarelli and G. Parisi, *Asymptotic Freedom in Parton Language*, Nucl. Phys. **B126** (1977) 298.

[21] B. Andersson et al., *Parton Fragmentation and String Dynamics*, Phys. Rept. **97** (1983) 31–145.

[22] J. Alcaraz, *Precision Electroweak Measurements and Constraints on the Standard Model*, `arXiv:0911.2604 [hep-ex]`.

[23] **CKMfitter Group**, J. Charles et al., *CP violation and the CKM matrix: Assessing the impact of the asymmetric B factories*, Eur. Phys. J. **C41** (2005) 1–131.

[24] J. R. Ellis, *Beyond the standard model with the LHC*, Nature **448** (2007) 297–301.

[25] H. P. Nilles, *Supersymmetry, Supergravity and Particle Physics*, Phys. Rept. **110** (1984) 1–162.

[26] H. E. Haber and G. L. Kane, *The Search for Supersymmetry: Probing Physics Beyond the Standard Model*, Phys. Rept. **117** (1985) 75–263.

[27] L. Randall and R. Sundrum, *A large mass hierarchy from a small extra dimension*, Phys. Rev. Lett. **83** (1999) 3370–3373.

[28] N. Arkani-Hamed et al., *The hierarchy problem and new dimensions at a millimeter*, Phys. Lett. **B429** (1998) 263–272.

[29] I. Antoniadis et al., *New dimensions at a millimeter to a Fermi and superstrings at a TeV*, Phys. Lett. **B436** (1998) 257–263.

[30] **Tevatron Electroweak Working Group**, M. Lancaster et al., *Combination of CDF and DO results on the mass of the top quark using up to 5.8 fb-1 of data*, `arXiv:1107.5255 [hep-ex]`.

[31] **CDF Collaboration**, F. Abe et al., *Observation of top quark production in $\bar{p}p$ collisions*, Phys. Rev. Lett. **74** (1995) 2626–2631.

[32] **D0 Collaboration**, S. Abachi et al., *Observation of the top quark*, Phys. Rev. Lett. **74** (1995) 2632–2637.

[33] W. Bernreuther, *Top quark physics at the LHC*, J. Phys. **G35** (2008) 083001.

[34] J. C. Collins, D. E. Soper, and G. Sterman, *Heavy Particle Production in High-Energy Hadron Collisions*, Nucl. Phys. **B263** (1986) 37.

[35] **D0 Collaboration**, V. M. Abazov et al., *Observation of Single Top-Quark Production*, Phys. Rev. Lett. **103** (2009) 092001.

[36] **CDF Collaboration**, T. Aaltonen et al., *First Observation of Electroweak Single Top Quark Production*, Phys. Rev. Lett. **103** (2009) 092002.

[37] **CDF Collaboration**, T. Aaltonen et al., *Observation of Single Top Quark Production and Measurement of $|V_{tb}|$ with CDF*, Phys. Rev. **D82** (2010) 112005.

[38] **The ATLAS Top Working Group**, R. Hawkings et al., *private communication 2009*, Internal overview of Monte Carlo samples, cross sections and scaling factors for top quark analysis with MC08 production. The numbers are calculated with the use of [70, 78, 79, 80].

[39] **D0 Collaboration**, V. M. Abazov et al., *Combination of ttbar cross section measurements and constraints on the mass of the top quark and its decays into charged Higgs bosons*, Phys. Rev. **D80** (2009) 071102.

[40] **The ATLAS Collaboration**, G. Aad et al., *Expected Performance of the ATLAS Experiment - Detector, Trigger and Physics*, `arXiv:0901.0512 [hep-ex]`.

[41] S. Catani, *Aspects of QCD, from the Tevatron to the LHC*, `arXiv:hep-ph/0005233`.

[42] L. Evans et al., *LHC Machine*, JINST **3** (2008) S08001.

[43] **CMS Collaboration**, R. Adolphi et al., *The CMS experiment at the CERN LHC*, JINST **3** (2008) S08004.

[44] **LHCb Collaboration**, A. A. Alves et al., *The LHCb Detector at the LHC*, JINST **3** (2008) S08005.

[45] **ALICE Collaboration**, K. Aamodt et al., *The ALICE experiment at the CERN LHC*, JINST **3** (2008) S08002.

[46] **The ATLAS Collaboration**, G. Aad et al., *The ATLAS Experiment at the CERN Large Hadron Collider*, JINST **3** (2008) S08003.

[47] D. Gingrich et al., *Construction, assembly and testing of the ATLAS hadronic end-cap calorimeter*, Tech. Rep. CERN-ATL-COM-LARG-2007-006, CERN, Geneva, Apr 2007.

[48] **ATLAS Liquid Argon EMEC/HEC/FCAL**, J. Pinfold et al., *Performance of the ATLAS liquid argon endcap calorimeter in the pseudorapidity region* $2.5 < |\eta| < 4.0$ *in beam tests*, Nucl. Instrum. Meth. **A593** (2008) 324–342.

[49] **ATLAS Liquid Argon EMEC/HEC**, C. Cojocaru et al., *Hadronic calibration of the ATLAS liquid argon end-cap calorimeter in the pseudorapidity region* $1.6 < |\eta| < 1.8$ *in beam tests*, Nucl. Instrum. Meth. **A531** (2004) 481–514.

[50] G. P. Salam, *Towards Jetography*, Eur.Phys.J. **C67** (2010) 637–686.

[51] **The ATLAS Collaboration**, *Atlas Computing: technical design report*, tech. rep., Geneva, 2005.

[52] G. P. Salam and G. Soyez, *A practical Seedless Infrared-Safe Cone jet algorithm*, JHEP **05** (2007) 086.

[53] S. Catani et al., *Longitudinally invariant K_t clustering algorithms for hadron hadron collisions*, Nucl. Phys. **B406** (1993) 187–224.

[54] S. D. Ellis and D. E. Soper, *Successive combination jet algorithm for hadron collisions*, Phys.Rev. **D48** (1993) 3160–3166.

[55] M. Cacciari, G. P. Salam, and G. Soyez, *The anti-kt jet clustering algorithm*, JHEP **04** (2008) 063.

[56] W. Lampl et al., *Calorimeter clustering algorithms: Description and performance*, Tech. Rep. ATL-LARG-PUB-2008-002, CERN, Geneva, 2008.

[57] T. Sjostrand, *High-energy physics event generation with PYTHIA 5.7 and JETSET 7.4*, Comput. Phys. Commun. **82** (1994) 74–90.

[58] S. Agostinelli et al., *GEANT4 a simulation toolkit*, Nucl. Instr. and Meth. A **506** (2003) no. 3, 250–303.

[59] *CERN Program Library*, 1999. `http://cernlib.web.cern.ch/cernlib/`.

[60] **The ATLAS Collaboration**, T. Barillari et al., *Local Hadronic Calibration*, Tech. Rep. ATL-LARG-PUB-2009-001, 2009.

[61] **The ATLAS Collaboration**, B. Smith et al., *Identifying Merged Jets using Principal Component Analysis*, Tech. Rep. ATL-COM-PHYS-2009-338, 2009.

[62] M. L. Mangano et al., *ALPGEN, a generator for hard multi parton processes in hadronic collisions*, JHEP **07** (2003) 001.

[63] G. Marchesini et al., *HERWIG: A Monte Carlo event generator for simulating hadron emission reactions with interfering gluons. Version 5.1 - April 1991*, Comput.Phys.Commun. **67** (1992) 465–508.

[64] S. Frixione and B. R. Webber, *Matching NLO QCD computations and parton shower simulations*, JHEP **0206** (2002) 029.

[65] J. M. Butterworth et al., *Multiparton interactions in photoproduction at HERA*, Z. Phys. **C72** (1996) 637–646.

[66] **The ATLAS Collaboration**, *Inputs to Jet Reconstruction and Calibration with the ATLAS Detector Using Proton-Proton Collisions at* $\sqrt{s} = 900\ GeV$, Tech. Rep. ATLAS-CONF-2010-016, CERN, Geneva, Jul 2010.

[67] **The ATLAS Collaboration**, *ATLAS Monte Carlo tunes for MC09*, Tech. Rep. ATL-PHYS-PUB-2010-002, CERN, Geneva, Mar 2010.

[68] **The ATLAS Collaboration**, G. Aad et al., *The ATLAS Simulation Infrastructure*, Eur. Phys. J. **C70** (2010) 823–874.

[69] P. M. Nadolsky et al., *Implications of CTEQ global analysis for collider observables*, Phys. Rev. D **78** (2008) no. 1, 013004.

[70] S. Moch and P. Uwer, *Theoretical status and prospects for top-quark pair production at hadron colliders*, Phys. Rev. **D78** (2008) 034003.

[71] B. P. Kersevan and E. Richter-Was, *The Monte Carlo event generator AcerMC version 2.0 with interfaces to PYTHIA 6.2 and HERWIG 6.5*, `arXiv:hep-ph/0405247`.

[72] E. Rauter, *Top Quark Mass Measurement: Prospects of Commissioning Studies for Early LHC Data in the ATLAS Detector*. PhD thesis, TU Munich, 2009.

[73] R. J. Barlow, *Statistics: A Guide to the Use of Statistical Methods in the Physical Sciences*. Jon Wiley and Sons, 1989.

[74] R. Brun and F. Rademakers, *ROOT: An object oriented data analysis framework*, Nucl. Instrum. Meth. **A389** (1997) 81–86. `http://root.cern.ch`.

[75] P. Giovannini, *Studies on the top quark mass measurement in the all-hadronic top-antitop decay channel with ATLAS*. PhD thesis, TU Munich, 2011.

[76] *Measurement of the Top-Quark Mass using the Template Method in pp Collisions at root(s)=7 TeV with the ATLAS detector*, Tech. Rep. ATLAS-CONF-2011-033, CERN, Geneva, Mar 2011.

[77] H. Lesch, *Planeten, Sterne, Galaxien: Der Astrophysiker Harald Lesch beantwortet den GEO-Fragebogen*, GEO **11** (2006) 28.

[78] U. Langenfeld et al., *Measuring the running top-quark mass*, Phys. Rev. **D80** (2009) 054009.

[79] N. Kidonakis and R. Vogt, *Next-to-next-to-leading order soft gluon corrections in top quark hadroproduction*, Phys. Rev. **D68** (2003) 114014.

[80] R. Bonciani et al., *NLL resummation of the heavy quark hadroproduction cross-section*, Nucl. Phys. **B529** (1998) 424–450.

[81] E. Kästner, *Als ich ein kleiner Junge war*. Atrium Verlag, 1957.

Acknowledgement

> "Wenn es zutreffen sollte, dass ich nicht nur weiß, was schlimm und hässlich, sondern auch was schön ist, so verdanke ich diese Gabe dem Glück, in Dresden aufgewachsen zu sein."
>
> Erich Kästner [81]

First of all, I would like to express my gratitude to Prof. Dr. Siegfried Bethke and Dr. Sven Menke. You gave me the opportunity to work on one of the greatest projects in science, the ATLAS experiment. I appreciated very much your supervision of my research work and your valuable comments on this thesis.

Further, I would like to thank my colleagues from the Max-Planck-Institute for Physics. I really enjoyed the international atmosphere full of discussions about physics, politics and football. In particular, I would like to thank the members of the HEC group, by name Horst, Peter, Sven, Teresa, Gennady, Paola, Andrej, Denis and Martin. Thanks a lot for your help and support during my time in the group. For the great time I spend at CERN, I would also like to mention Gabi, Emanuel and Pavol. I learned so much from you about the experiment and thanks to you, I always felt welcome in Geneva.

For thanking my office mates Paola and Gena, words are not enough. You became real friends to me and it was my honour to spend the last years with you in this little room. You know better than me how much I already miss our time together, our open discussions and cultural misunderstandings. I hope we will always find an occasion for a little coffee in the future.

Not forgotten should be my parents, my whole family and all my friends. Your support, your understanding and your patience were more important to me than you might think. Thank you for this and I owe all of you a big apology since nobody of you got the deserved attention in the last months. I promise to do better in the near future!

Finally, I am very grateful to all my colleagues at CALEO, especially to Hanno Hetzer and Dr. Jan Gräter. You did not only give me a great job opportunity, but also I could always count on your support to complete this thesis.

The last, but most important ingredient is you, Caro. Without your support, I could not have written this thesis. But even more important, without your love, I would not be the same person. Please forgive me the delay of our plans, I am looking forward to our future.